COMPARTMENTALIZED GRANULAR GASES

CLUSTERING AND DIRECTED TRANSPORT

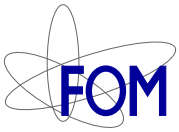

The research described in this thesis is part of the research program of the ”Stichting voor Fundamenteel Onderzoek der Materie” (FOM), which is financially supported by the ”Nederlandse Organisatie voor Wetenschappelijk Onderzoek” (NWO). It was carried out at the Physics of Fluids research group of the faculty of Science and Technology of the University of Twente.

Nederlandse titel:
Granulair gas in compartimenten:
over clusterende kogels en gericht deeltjestransport.

Publisher:
Devaraj van der Meer, Physics of Fluids, University of Twente,
P.O Box 217, 7500 AE Enschede, The Netherlands
www.tn.utwente.nl/PoF

Cover design: Devaraj van der Meer
Print: PrintPartners Ipskamp B.V., Enschede

ISBN 90-365-2031-2

COMPARTMENTALIZED GRANULAR GASES

CLUSTERING AND DIRECTED TRANSPORT

PROEFSCHRIFT

ter verkrijging van
de graad van doctor aan de Universiteit Twente,
op gezag van de rector magnificus,
prof. dr. F.A. van Vught,
volgens besluit van het College voor Promoties
in het openbaar te verdedigen
op donderdag 29 april 2004 om 15.00 uur

door

Roger Maurice van der Meer
(Devaraj)

geboren op 1 augustus 1963

te Amsterdam

Dit proefschrift is goedgekeurd door de promotor:

prof. dr. rer. nat. D. Lohse

To my wife Nileen
my children Steven and Mara
and my parents Ben and Ruth
With love

Contents

Chapter 1

Introduction

1.1 Clustering in granular gases

Granular matter is often referred to as the fourth state of matter [1]: Depending on the situation, it can behave as a solid, a liquid, or a gas. When sand flows through an hourglass, it behaves as a liquid, while the pile on which it pours down is solid-like. And when dry sand is fluidized by blowing air through it or by strong shaking, it behaves like a gas.

Granular matter belongs to the class of many body systems far from equilibrium which display a wide range of fascinating collective behavior. Out of the various types of complex matter, granular materials are particularly attractive because of their easy accessibility to experiments, while at the same time they exemplify many concepts in modern physics.

To quote Isaac Goldhirsch in a recent review on rapid granular flows [2]: *"The newcomers to this field have rapidly realized its great practical importance as well as the fact that it poses highly nontrivial scientific challenges, some of which pertain to the core of understanding of the nature of matter in general* [1, 3, 4]."

Granular gases consist of macroscopic particles which have kinetic energies many orders of magnitude larger than the thermal energy [5]. This difference in size is however not the main reason that they behave so differently from molecular gases, but the fact that grain collisions are typically inelastic: Whenever two grains collide they lose some their kinetic energy to internal degrees of freedom: heat, sound, or irreversible deformation. In consequence, to perpetuate the motion of the granular gas a continuous supply of energy is needed. Therefore granular gases are systems far from thermodynamic equilibrium, and have many remarkable properties unseen in ordinary gases.

One of the most characteristic features of granular gases is their tendency to spontaneously separate in dense and dilute regions [1, 2, 4]. The clustering effect was first demonstrated in numerical studies of rapid granular shear flows [6] and freely cooling granular gases [7]. In the latter paper, the particles start out from a spatially homogeneous state, with a Maxwellian velocity distribution, and are left to evolve without further energy input, which means that the mean kinetic energy (or equivalently, the granular temperature) decays with time due to the inelastic collisions.

The clustering process can be directly traced back to the inelasticity of the collisions between the grains [7]: In a region where, due to some fluctuation, the density exceeds the average density of the gas, the collision rate is higher and the granular temperature will therefore drop faster than in the neighboring, less dense regions. In hydrodynamical terms this means that a pressure gradient is built up between high and low temperature (and thus pressure) regions, resulting in a migration of particles into denser regions from diluter ones. Hence the dense regions become denser, and the dilute regions diluter, and this self-enhancing process spontaneously leads to the formation of clusters (consisting of many slow particles) coexisting with almost empty regions (where the particles move much faster).

The above clustering mechanism also holds for granular gases that are kept at a constant granular temperature by an external energy input [2, 8, 9]. The phenomenon becomes particularly clear-cut in a container divided into two compartments by a separating wall (Fig. 1.1) extending from the bottom to a certain height h. The container is mounted on a shaker, and filled with a few hundred beads which are brought into a gaseous state by shaking the system vertically, such that they are able to jump from one compartment to the other.

This system, nicknamed the 'Maxwell demon' experiment after the inspiring title of [10], was described first in the literature by two German physicists, Schlichting and Nordmeier, in an educational paper about structures found in granular matter. They observed that, when the system was shaken vigorously, the particles distributed themselves over the compartments, much like any ordinary gas would do. But when they reduced the driving they found a surprise. To quote the authors [11]:

"... Interessant wird es erst, wenn man die Amplitude der Grundplatte langsam drosselt. Dann nimmt die mittlere Sprunghöhe der Teilchen ab. Wird sie schließlich vergleichbar mit der Wandhöhe, so kann man etwas Erstaunliches beobachten: Entgegen der Erwartung, daß die Teilchen mit verschwindender Amplitude gleichverteilt in beiden Zellen zur Ruhe kommen, sammeln sie sich stets in nur einer der beiden Zellen."[*]

[*] ... Things becomes really interesting when the amplitude of the bottom is reduced. Then the average height of the jumps of the particles will go down. If it becomes comparable to the height

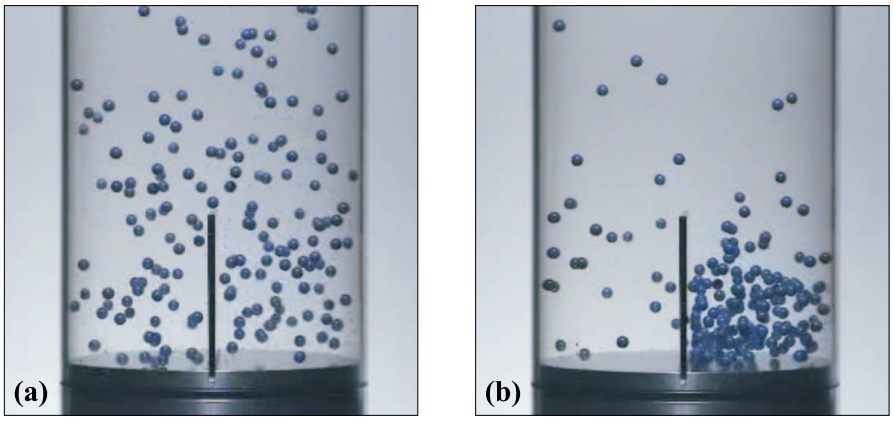

Figure 1.1: Two snapshots from the 'Maxwell demon' experiment, in which glass beads are shaken in a container divided into two compartments by a wall. (a) At vigorous shaking the particles distribute themselves evenly over the compartments, much like any ordinary gas would do. (b) At mild shaking the particles cluster together into one of the compartments: A steady state is reached in which a cluster of many slow particles is balanced by few, but very lively particles in the other compartment.

In order to describe the dynamics of this remarkable system, Eggers [10] proposed an analytical flux model. For simplicity he restricted himself to the 2D case, and assumed a slightly different setup: The wall is taken to extend over the whole height of the system, with only a small opening positioned at a certain height h above the bottom.

In this thesis, the two-compartment system of Schlichting and Nordmeier is extended to a multibox system, which turned out to be an extremely fruitful extension, giving rise to an abundance of phenomena, like hysteresis, coarsening, the sudden collapse phenomenon, competitive clustering, and directed transport. In describing these phenomena the flux model proved a valuable analytical tool; in the next section we present a derivation which roughly follows the one by Eggers [10].

1.2 Derivation of the Eggers flux function

The setup that will be studied in this section consists of a (rectangular) container, which is mounted on a shaker and filled with small grains. The grains are fluidized

of the separating wall, the observer will be witness to an astonishing phenomenon: against the expectation that at decreasing amplitude the particles will slowly come to rest, neatly spread over both compartments, they are seen to accumulate in just one of the compartments.

by vertically vibrating the setup with a sawtooth-shaped signal with frequency f and amplitude a. The container has a small, rectangular aperture of size $S = w\,\Delta h$ at a certain height h. For the derivation of the model the grains are assumed to be frictionless spheres, such that only normal restitution contributes to the dissipation. Furthermore, any collisions with the walls (extending all the way up to infinity) and bottom are assumed to be perfectly elastic.

The objective is to obtain an expression for the flux through the aperture as a function of the particle fraction (or number of particles) in the compartment. To this end, we first need to find expressions for the temperature and density near the aperture.

To describe the gas in the container, we start out from the general (three-dimensional) hydrodynamics equations for a dissipative, low density granular gas, as they can be derived from Boltzmann's equation [12–16] by taking its first three moments with respect to the velocity distribution

$$\begin{aligned} \frac{Dn}{Dt} + n\nabla\cdot\boldsymbol{u} &= 0 \\ mn\frac{D\boldsymbol{u}}{Dt} + \nabla\cdot\mathbf{P} &= n\mathbf{f}, \\ n\frac{Dk_BT}{Dt} + \mathbf{P}:\nabla\boldsymbol{u} + \nabla\cdot\mathbf{J} &= I. \end{aligned} \tag{1.1}$$

where $D/Dt \equiv \partial/\partial t + \boldsymbol{u}\cdot\nabla$ is the Lagrangian or material derivative. The first equation, in which n is the local particle density, reflects mass conservation. The second one, featuring the velocity field $\boldsymbol{u}$, the stress (or pressure) tensor $\mathbf{P}$, and the external force (due to gravity) per particle $\mathbf{f} = -mg\mathbf{e}_z$[†], expresses the conservation of momentum. The third, with T the granular temperature, $\mathbf{J}$ the heat flux vector and I the energy dissipation rate per unit volume, conveys conservation of energy. The combination $(3/2)k_BT$ is equal to the local mean kinetic energy of the particles in the Lagrangian sense, i.e., in a reference frame which is moving with the flow. The stress tensor $\mathbf{P}$ and k_BT are subject to the identity: $\mathrm{tr}(\mathbf{P}) = 3nk_BT$, where $\mathrm{tr}(\mathbf{P})$ is defined as the sum of the diagonal elements of the tensor. This identity follows directly from their definition in terms of the one-particle distribution function (see e.g. [12]). The Boltzmann constant k_B can be chosen at will, to define a granular temperature scale suitable for the system under consideration.

In a stationary situation, and in the absence of net flow, the above set of three equations reduces to

$$\nabla\cdot\mathbf{P} = n\mathbf{f}, \tag{1.2}$$

$$\nabla\cdot\mathbf{J} = I. \tag{1.3}$$

[†] m and g are the particle mass and the acceleration of gravity respectively

The next step is to assume that the stress tensor is of diagonal form (normal stress only), and that all three elements are equal (isotropy). In terms of the diagonal elements p the identity $\mathrm{tr}(\mathbf{P}) = 3nk_BT$ reduces to $p = nk_BT$, which is recognized as the ideal gas law when p is identified as the pressure. Herewith Eq. (1.2) becomes

$$\nabla p = n\mathbf{f} \qquad \Rightarrow \qquad \frac{d(nk_BT)}{dz} = -nmg. \tag{1.4}$$

To arrive at the right hand side equation, we have chosen gravity along the z-axis and took the temperature and density to be dependent on the vertical coordinate only. This expression yields, upon integration

$$n(z) = \frac{mgP}{\Omega k_BT(z)} \exp\left\{-\int_0^z \frac{mg}{k_BT(\zeta)} d\zeta\right\}. \tag{1.5}$$

Here P is the total number of particles in the compartment and Ω is the ground area of the compartment[‡].

The second equation [Eq. (1.3)] can be integrated over the container volume V, which with use of Gauss' theorem gives

$$\int_{\partial V} \mathbf{J} \cdot \mathbf{dA} = \int_V I \, dV \qquad \text{or} \qquad Q_{in} = Q_{diss}, \tag{1.6}$$

where ∂V stands for the boundaries of the container, i.e., the walls and the bottom. Since the walls (and bottom) are assumed to be non-dissipative, the only contribution to the left integral stems from the energy input rate (Q_{in}) at the bottom. This should be balanced by the right integral, which can be interpreted as the total dissipation rate in the container.

The assumptions made up to this point are common to all hydrodynamic analyses of containers filled with smooth spheres (see e.g. [17–20]).

The key assumption of the Eggers model is that the temperature is constant within the gas [10]. This is in good agreement with molecular dynamics simulations (Fig. 1.2a), apart from a small region just above the bottom, where the energy input leads to an increase of the temperature. With this assumption, the evaluation of the integral in Eq. (1.5) results in the barometric height distribution

$$n(z) = \frac{mgP}{\Omega k_BT} \exp\left\{-\frac{mgz}{k_BT}\right\}. \tag{1.7}$$

[‡]The prefactor follows by directly integrating Eq. (1.4) from zero to infi nity.

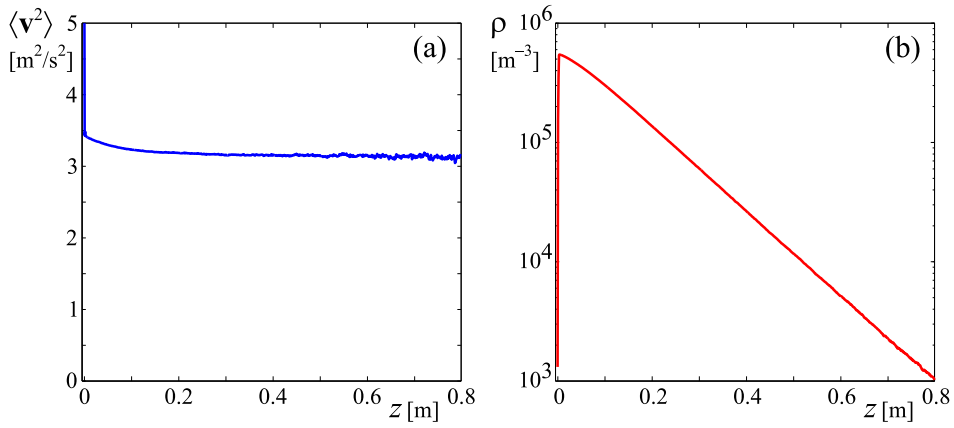

Figure 1.2: (a) The granular temperature in a molecular dynamics simulation of a granular gas is nearly constant throughout the gas, with the exception of a small region just above the fbor. (b) The particle density n quickly approaches the barometric height distribution, which is a straight line in this semi-logarithmic plot. The granular gas in the simulation consists of 50 smooth particles of diameter 2.36 mm and normal restitution coeffi cient $e = 0.90$, in a container with a fbor area of 6.25 cm ^{2}, driven by a sinusoidal driving signal ($a = 1$ mm, and $f = 72.6$ Hz).

The temperature can now be written as a function of P by making use of Eq. (1.6). To this end, we first need to express Q_{in} and Q_{diss} in terms of P and T. For Q_{diss} this can be done in various ways, with different levels of sophistication, leading to results with increasing complexity (see e.g. [12, 21]). The standard way is to assume a local Maxwell-Boltzmann distribution for the velocity, calculate the probability for a collision between two particles at positions $\boldsymbol{r}_1$ and $\boldsymbol{r}_2$, with velocities $\boldsymbol{v}_1$ and $\boldsymbol{v}_2$ respectively, and average over the ensemble. This gives

$$Q_{diss} = 4\frac{\sqrt{\pi m}}{\Omega} g r^2 P^2 (1 - e^2)\sqrt{k_B T_z}. \tag{1.8}$$

More intricate approaches, using the Chapman-Enskog method up to Burnett order, give results which only differ from Eq. (1.8) by a multiplicative function depending on the coefficient of restitution e only [14, 16]. They approach Eq. (1.8) in the limit of small e. A similar procedure for the energy input at the bottom gives

$$Q_{in} = \frac{mgPu}{k_B T}\psi(\gamma). \tag{1.9}$$

This is true for any type of driving, with u the rms velocity of the driving, $\gamma \equiv [2k_B T/(mu^2)]^{1/2}$ a dimensionless number equal to the ratio of a typical particle

velocity and the average velocity of the floor, and $\psi(\gamma)$ a function which depends on the driving shape only. For the sawtooth driving considered here we have $u = 2af$ and $\psi(\gamma) = \gamma/\sqrt{\pi} + \gamma^2/2$. The quantity γ is typically large in the gaseous state, where particle velocities are on average much larger than the velocity of the bottom, and thus $\psi(\gamma) \approx \gamma^2/2$. If we insert this in Eq. (1.9) we obtain

$$Q_{in} \approx 2mgPaf. \tag{1.10}$$

By equating the expressions Eqs. (1.8) and (1.10), we can finally express the temperature in the number of particles in the container:

$$k_B T = \frac{m\Omega^2 a^2 f^2}{4\pi(1-e^2)^2 r^4 P^2}. \tag{1.11}$$

The flux (in particles per second) from the compartment is now found by multiplying the density of particles moving towards the wall ($n(z)/2$) at height h with the average velocity normal to the aperture and the area of the aperture (S):

$$\begin{aligned} \widehat{F}(P) &= \frac{1}{2} n(h) \sqrt{\frac{2k_B T}{\pi m}} S \\ &= \widehat{A} P^2 \exp\left\{-\widehat{B} P^2\right\}, \end{aligned} \tag{1.12}$$

with:

$$\begin{aligned} \widehat{A} &= \sqrt{2}\,(1-e^2)\,\left(\frac{g\,r^2\,S}{a\,f\,\Omega^2}\right), \\ \widehat{B} &= 4\pi(1-e^2)^2 \left(\frac{gh}{a^2 f^2}\right)\left(\frac{r^4}{\Omega^2}\right). \end{aligned} \tag{1.13}$$

This concludes the derivation of the flux function[§]. It has the property that it is non-monotonous: the flux first increases from zero (for $P = 0$) until it reaches a maximum and then, due to the inelasticity of the collisions, decreases again (Fig. 1.3). It is this property that allows for the flux from a dense compartment to be balanced by an equal but opposite flux from a diluted compartment, and thus for the clustering in a compartmentalized granular gas.

One of the frequently encountered objections to the constant temperature assumption is that the largest deviations from constant temperature are found exactly there where the energy is put into the system, i.e., at the bottom of the container. When solving the problem in the context of differential equations it would seem

[§]The notation $\widehat{F}$, $\widehat{A}$, and $\widehat{B}$ distinguishes these quantities from F, A, and B which are used in the coming chapters and are defi ned with respect to particle fractions, instead of particle numbers.

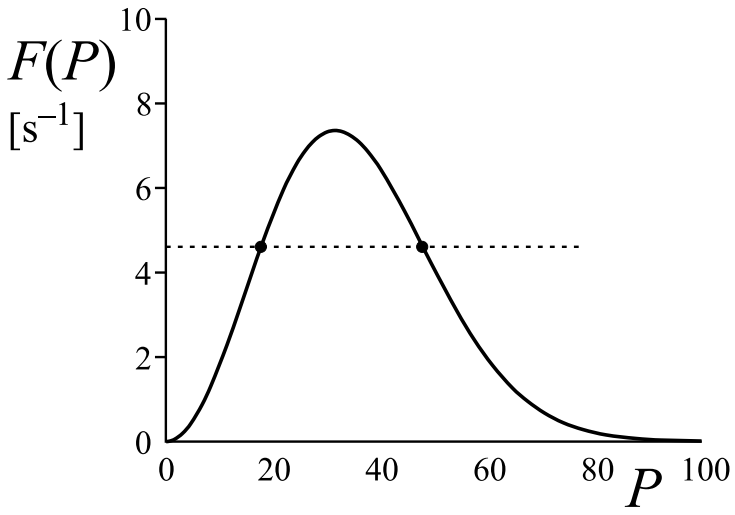

Figure 1.3: The Eggers flux function, giving the flux (in particles per second) through an aperture in the wall as a function of the number of particles in a compartment. The horizontal dashed line indicates how the flux from a diluted compartment can balance the flux from a densely populated compartment. (The plot is calculated from Eq. (1.12) using $\widehat{A} = 0.02\ \mathrm{s}^{-1}$, $\widehat{B} = 0.001$.)

that applying the boundary condition at the bottom would cause large discrepancies between the assumed constant temperature and the actual temperature.

The integral approach presented above however shows that, because the total energy input rate at the bottom is balanced with the total dissipation rate within the gas, solving the equations in the constant temperature assumption is more like using an *averaged temperature* assumption, in which the actual temperature profile is replaced by a constant temperature giving the same dissipation rate in the system.

The great advantage of the constant (or average) temperature approach is that we obtain an *analytical* approximation for the flux function, instead of the numerical expression which is found when performing the full integration of Eqs. (1.2) and (1.3). Qualitatively, it is true that many of the phenomena that will be discussed in this thesis are rather determined by the fact that the flux function is non-monotonic (i.e. attaining a maximum for a certain particle density and then decreasing again), than by its precise form. But in order to analyze these phenomena, the benefit of having an analytical expression for the flux is enormous.

1.3 A guide through the chapters

The 'Maxwell demon' experiment, where the granular gas in a partitioned vertically driven container spontaneously clusters in one of the two compartments, is a surprising and counter-intuitive phenomenon (see Section 1.1). The main objective of this thesis is to study the implications of the generalization of the geometry of the system into arrays of many connected compartments.

In Chapter 2 experiments of the original two-compartment are found to be in good agreement with the flux model from [10], showing a continuous phase transition towards the clustered state. When the system is extended to three compartments there is a surprise: We now find a second order phase transition which goes hand in hand with the observed *hysteresis* [22].

From an analysis within the context of the flux model we find that hysteresis is generic to all systems with more than two compartments. This is the key result of Chapter 3, in which the bifurcation diagram for a container divided into an arbitrary number of compartments is constructed. By means of a stability analysis it is found that there are only two stable situations possible: the uniform distribution, for very high driving strengths, and the state in which just one cluster is present, for milder shaking. The hysteresis between these states becomes more and more pronounced as the number of compartments increases [23].

One of the remarkable observations is the abruptness of the collapse of the clusters for systems containing a single, unstable cluster at sufficiently strong shaking. In Chapter 4 we analytically calculate the observed cluster lifetime as a function of the driving intensity. Here we make use of the self-similarity of the process [24].

Very close to the critical point, where the cluster becomes stable, the lifetime diverges with a critical exponent $-1/2$. This is explained in Chapter 5, using a mean field potential formulation [25].

The path to the one-cluster state is far from direct: Starting from a granular gas which is homogeneously distributed over the container the particles in a first stage cluster in a few of the compartments. In the second stage these clusters collapse one by one, at ever increasing timescales. This *coarsening process*, which is the subject of Chapter 6, is found to be anomalously slow [26]. This chapter concludes our discussion of the phenomena observed in the vertically vibrated granular gas in N simply connected compartments.

In Chapter 7, we modify the system by adding a small hole at the bottom of each wall. In this way we create a *"granular fountain"*, in which the spontaneous clustering of a vibrofluidized granular gas is used to generate convection rolls, which, in experiment, are reminiscent of the common fluid fountain. A sec-

ond modification leads to a *"granular ratchet"* with a spontaneous particle current perpendicular to the direction of energy input. In both instances, transport arises spontaneously, as a collective symmetry breaking effect of many interacting granular particles [27].

Searching for ways to refine the flux model, we came across the observation that, in molecular dynamics simulations, the average squared velocity (temperature) in the horizontal directions was consistently smaller than the temperature in the vertical direction, in which the energy is put into the container. In Chapter 8 we present a simplified analytical model, which quantitatively explains these observations. The main conclusion is that anisotropic driving of a granular gas in a steady state *necessarily* causes anisotropy of the granular temperature [28].

The work presented in this thesis is a close combination of laboratory experiments, molecular dynamics simulations, and theoretical analysis, both within the flux model and beyond. As seen again and again, all three are found to agree very well, shedding light onto the clustering effect in granular gases.

References

[1] H.M. Jaeger, S.R. Nagel, and R.P. Behringer, *Granular solids, liquids, and gases*, Rev. Mod. Phys. **68**, 1259 (1996).

[2] I. Goldhirsch, *Rapid granular flows*, Annu. Rev. Fluid Mech. **35**, 267 (2003).

[3] M-L. Tan and I. Goldhirsch, *Rapid granular flows as mesoscopic systems*, Phys. Rev. Lett. **81**, 3022 (1998).

[4] L.P. Kadanoff, *Built upon sand: Theoretical ideas inspired by granular flows*, Rev. Mod. Phys. **71**, 435 (1999).

[5] J. Duran, *Sands, powders, and grains: An introduction to the physics of granular materials* (Springer Verlag, Berlin, Germany, 2000), 1st ed.

[6] M.A. Hopkins and M.Y. Louge, *Inelastic microstructure in rapid granular flows of smooth disks*, Phys. Fluids A **3**, 47 (1991).

[7] I. Goldhirsch and G. Zanetti, *Clustering instability in dissipative gases*, Phys. Rev. Lett. **70**, 1619 (1993).

[8] Y. Du, H. Li, and L.P. Kadanoff, *Breakdown of hydrodynamics in a one-dimensional system of inelastic particles*, Phys. Rev. Lett. **74**, 1268 (1995).

[9] A. Kudrolli, M. Wolpert, and J.P. Gollub, *Cluster formation due to collisions in granular material*, Phys. Rev. Lett. **78**, 1383 (1997).

[10] J. Eggers, *Sand as Maxwell's demon*, Phys. Rev. Lett. **83**, 5322 (1999).

[11] H.J. Schlichting and V. Nordmeier, *Strukturen im Sand*, Math. Naturwiss. Unterr. **49**, 323 (1996).

[12] J.J. Brey, M.J. Ruiz-Montero, and F. Moreno, *Steady uniform shear flow in a low density granular gas*, Phys. Rev. E **55**, 2846 (1997).

[13] J.J. Brey, J.W. Dufty, and A. Santos, *Dissipative dynamics for hard spheres*, J. Stat. Phys. **87**, 1051 (1997).

[14] J.J. Brey, J.W. Dufty, C.S. Kim, and A. Santos, *Hydrodynamics for granular flow at low density*, Phys. Rev. E **58**, 4638 (1998).

[15] T.C.P. van Noije, M.H. Ernst, and R. Brito, *Ring kinetic theory for an idealized granular gas*, Physica A **251**, 266 (1998).

[16] N. Sela and I. Goldhirsch, *Hydrodynamic equations for rapid flows of smooth inelastic spheres, to Burnett order*, J. Fluid Mech. **361**, 41 (1998).

[17] A. Baldassarri, U. Marini Bettolo Marconi, A. Puglisi, and A. Vulpiani, *Driven granular gases with gravity*, Phys. Rev. E **64**, 011301 (2001).

[18] J.J. Brey, J. Ruiz-Montero, and F. Moreno, *Hydrodynamics of an open vibrated granular system*, Phys. Rev. E **63**, 061305 (2001).

[19] J. J. Brey, F. Moreno, R. García-Rojo, and M. J. Ruiz-Montero, *Hydrodynamic Maxwell demon in granular systems*, Phys. Rev. E **65**, 011305 (2002).

[20] A. Barrat and E. Trizac, *A molecular dynamics 'Maxwell demon' experiment for granular mixtures*, Molecular Physics **101**, 1713 (2003).

[21] V. Kumaran, *Temperature of a granular material 'fluidized' by external vibrations*, Phys. Rev. E **57**, 5660 (1998).

[22] K. van der Weele, D. van der Meer, M. Versluis, and D. Lohse, *Hysteretic clustering in a granular gas*, Europhys. Lett. **53**, 328 (2001).

[23] D. van der Meer, K. van der Weele, and D. Lohse, *Bifurcation diagrams of compartmentalized granular gases*, Phys. Rev. E **63**, 061304 (2001).

[24] D. van der Meer, K. van der Weele, and D. Lohse, *Sudden collapse of a granular cluster*, Phys. Rev. Lett. **88**, 174302 (2002).

[25] D. van der Meer and K. van der Weele, *Breakdown of a near-stable granular cluster*, Prog. Theor. Phys. Suppl. **150**, 297 (2003).

[26] D. van der Meer, K. van der Weele, and D. Lohse, *Coarsening dynamics of compartmentalized granular gases*, JSTAT **1** (in press, 2004).

[27] D. van der Meer, P. Reimann, K. van der Weele, and D. Lohse, *Spontaneous ratchet effect in a granular gas*, Phys. Rev. Lett. **92** (in press, 2004).

[28] D. van der Meer and P. Reimann, *Temperature anisotropy in a driven granular gas*, preprint (submitted to PRL, 2004).

Chapter 2

Hysteretic Clustering in a Granular Gas [‡]

Granular material is vibro-fluidized in $N = 2$ and $N = 3$ connected compartments, respectively. For sufficiently strong shaking the granular gas is equipartitioned, but if the shaking intensity is lowered, the gas clusters in one compartment. The phase transition towards the clustered state is of 2nd order for $N = 2$ and of 1st order for $N = 3$. In particular, the latter is hysteretic. The experimental findings are accounted for within a dynamical model that exactly has the above properties.

2.1 The "Maxwell Demon" experiment

One of the characteristic features of a granular gas is its tendency to spontaneously separate in dense and dilute regions [1–7]. This makes granular gases fundamentally different from ordinary molecular gases. The dynamics of granular material is of importance for many industrial applications where it is brought into motion in order to sort, transport, or process it. Here clustering usually is an unwanted effect and any further understanding may yield a substantial economic benefit.

The tendency to form clusters can be traced back to the fact that the collisions between the granules are inelastic. Some energy is dissipated in every collision, which means that a relatively dense region (where the particles collide more often than elsewhere) will dissipate more energy, and thus become even denser, resulting

[‡]Published as: Ko van der Weele, Devaraj van der Meer, Michel Versluis, and Detlef Lohse, *Hysteretic Clustering in a Granular Gas*, Europhys. Lett. **53**, pp. 328-334 (2001)

in a cluster of slow particles. Vice versa, because the particle number is conserved, relatively dilute regions will become more dilute. The few particles in these regions are very rapid ones. In terms of the granular temperature, which goes as the mean squared velocity of the particles, the clustering phenomenon can also be interpreted as a separation in cold and hot regions, as if Maxwell's demon were at work [8].

A striking illustration of the clustering phenomenon is provided by the Maxwell-demon experiment [9], consisting of a box divided into two compartments by a wall of a certain height, with a few hundred small beads in each compartment. The beads are brought in a gaseous state by shaking the system vertically. If the shaking is vigorous enough, the inelasticity of the gas is overpowered by the energy input into the system, and the beads divide themselves uniformly over the two compartments as in any ordinary molecular gas. But if the driving is lowered below a certain level, the beads cluster in one of the two compartments. We end up with a "cold" compartment containing a lot of beads (moving rather sluggishly, hardly able to jump over the wall anymore) and a "hot" compartment containing only a few (much more lively) beads. In equilibrium, the average particle flux from left to right equals that from right to left.

Such an asymmetric equilibrium can only be explained if the flux of particles from one compartment to the other is not a monotonously increasing function of the number of particles. Rather it must be a function that attains a maximum (at a certain number of particles) and thereafter decreases again. In agreement with this, and based on the kinetic theory for dilute granular gases [10–12], Eggers proposed the following analytic approximation for the flux [8] (rewritten here in a form suited for an arbitrary number of N connected compartments),

$$F(n_k) = A n_k^2 e^{-N^2 B n_k^2}, \tag{2.1}$$

which is indeed a one-humped function of n_k, with a maximum at $n_k = 1/(N\sqrt{B})$. Here n_k is the fraction of the particles in the k-th box, normalized to $\sum n_k = 1$.

The factors A and B depend on the particle properties (such as their radius r, and the restitution coefficient e of the interparticle collisions) and on experimental parameters such as the height h of the wall and the frequency f and amplitude a of the driving. The factor A determines the absolute rate of the flux, and can simply be incorporated in the time scale. The phase transition towards the clustering state is only determined by the factor B, which for a 2D gas of spherical disks takes the form [8]

$$B = 4\pi g r^2 (1-e)^2 \frac{h}{(af)^2} \left(\frac{P}{lN}\right)^2, \tag{2.2}$$

where P is the total number of particles, and l is the width of each box. Again,

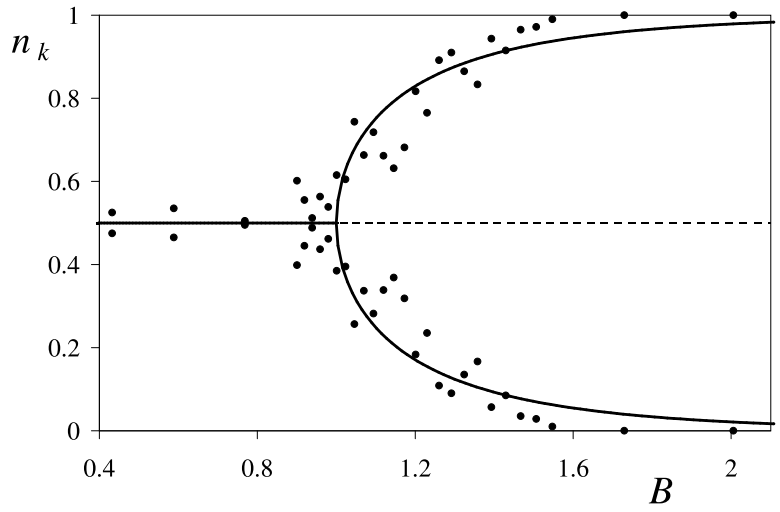

Figure 2.1: Bifurcation diagram for the 2-box system (k = 1, 2). The solid line represents stable and the dashed line unstable equilibria of the flux model. The dots are experimental measurements. In both cases, the transition to the clustering state is seen to take place via a pitchfork bifurcation.

we have chosen a notation that anticipates the generalization to a row of N equal boxes. For a given granular material (r and e fixed), B can be raised either by increasing the value of h or by decreasing the value of af, i.e., by reducing the driving.

In order to check how well this flux equation works in practice we compared theory and experiment for the 2-box system. Theory says that the dynamics is given by the balance equation

$$\frac{dn_1}{dt} = -F(n_1) + F(n_2) = -F(n_1) + F(1 - n_1), \tag{2.3}$$

and in equilibrium one has $dn_1/dt = 0$. One finds that for $B < 1$ there is only one (stable) equilibrium, namely the uniform $\{1/2, 1/2\}$ distribution. For $B > 1$ it becomes unstable and gives way to an asymmetric equilibrium. In other words, there is a symmetry breaking bifurcation at $B_{bif} = 1$. In Fig. 2.1 we have drawn the corresponding bifurcation diagram (cf. [8]).

For the experimental verification of this diagram we put 600 glass beads (r = 1.25 mm, e = 0.97) in a cylindrical perspex tube of inner radius 27.5 mm, di-

vided into two equal compartments by a wall of height h = 23.0 mm. The tube was mounted on a shaker with an adjustable frequency and amplitude, so that B could be varied. In the present experiments (for a 3D gas, with $B \propto 1/f^2$ still holding) this was done by varying of the frequency f, at a fixed value of a = 6.5 mm. The measurements are included as solid dots in Fig. 2.1. Clearly, theory and experiment agree on the fact that the clustering transition takes place via a pitchfork bifurcation. It may be noted that the experimental curves bend towards the $\{1, 0\}$ distribution earlier than predicted by the theory. This is due to the fact that the beads were counted not in the dynamical situation, but *after* the shaker had been turned off and the particles had come to rest. During the final bounces, the fast particles still jump over the wall (from the empty compartment into the full one), whereas jumps in the opposite direction hardly occur at all. The result is that a dynamical equilibrium of say $\{0.97, 0.03\}$ is turned into a static state $\{1, 0\}$, and that is what we count.

2.2 Generalization to three connected compartments

Now we generalize the experiment by taking not two, but three cyclic compartments ($N = 3$). Again, we find a uniform distribution $\{1/3, 1/3, 1/3\}$ at high driving levels, and a single-peak distribution at milder driving, but in contrast to the $N = 2$ case the transition between them is hysteretic, see Fig. 2.2. That is, the value of B at which the transition occurs when one goes from vigorous to mild driving is different from the B-value when one goes in the opposite direction. The experimental measurements were again done with 600 glass beads (r = 1.25 mm, e = 0.97) in a 3-compartment tube mounted on a shaker.

To account for this experimental finding, we assume that the approximate expression for the flux [Eq. (2.1)] remains valid also for 3 compartments. In this model, the dynamics of the system is governed by the following set of equations:

$$\frac{dn_1}{dt} = -2F(n_1) + F(n_2) + F(n_3), \qquad \text{and cyclic permutations.} \qquad (2.4)$$

The uniform distribution $\{1/3, 1/3, 1/3\}$ always is a solution, but it is stable only for $B < 1$. At this value it turns unstable and gives way to a single-peaked solution. This can be seen as follows.

From a linear stability analysis of the set of Eqs. (2.4) around the uniform solution $\{1/3, 1/3, 1/3\}$ we obtain the eigenvalues 0 and twice $-3F'(1/3)$. The zero eigenvalue, with eigenvector $(1, 1, 1)$, reflects the fact that synchronously raising (or lowering) the occupation numbers in the three compartments is forbidden

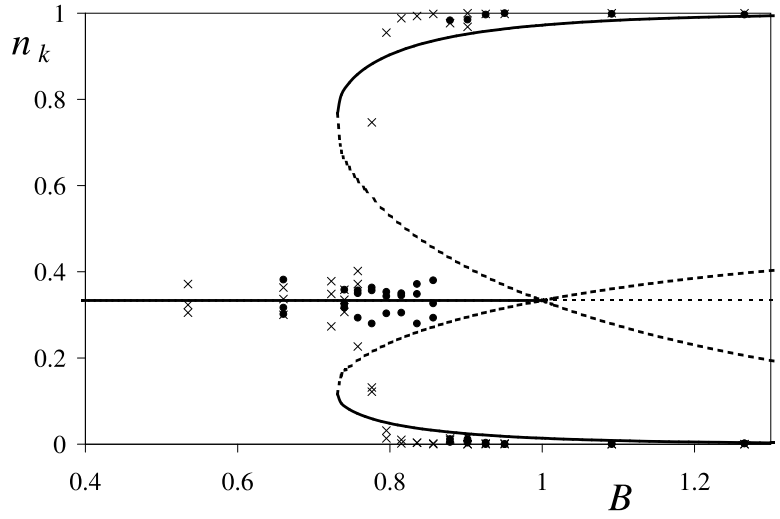

Figure 2.2: Hysteretic bifurcation diagram for the cyclic 3-box system ($k = 1, 2, 3$). The solid lines represent stable and the dashed lines unstable equilibria of the flux model. The bifurcations in this model take place at $B_{bif} = 1$ for increasing B and at $B_{sn} = 0.73$ for decreasing B. The dots and crosses are experimental measurements: The dots for measurements that were started from the uniform distribution $\{1/3, 1/3, 1/3\}$ and the crosses for those that were started from a single peaked distribution.

by particle conservation. The doubly degenerate eigenvalue becomes positive for $B > 1$, i.e., $\{1/3, 1/3, 1/3\}$ becomes unstable. Any small perturbations from the symmetric solution will grow, subject of course to the conservation condition $\sum n_k = 1$, which defines a plane in the 3D space $\{n_1, n_2, n_3\}$. Indeed, it is exactly this plane $\sum n_k = 1$ that is spanned by the two eigenvectors belonging to the degenerate eigenvalue. It is depicted in Fig. 2.3 in the form of a triangle. For instance, the lower left corner corresponds to the distribution $\{1, 0, 0\}$, and the solid dot in the center is the uniform distribution $\{1/3, 1/3, 1/3\}$.

Further insight can be gained by direct inspection of Eq. (2.4). Since $n_1 = 1 - n_2 - n_3$, this equation can also be written as:

$$\frac{dn_1}{dt} = -\frac{dn_2}{dt} - \frac{dn_3}{dt} = -2F(1 - n_2 - n_3) + F(n_2) + F(n_3), \qquad (2.5)$$

The uniform distribution ($n_1 = n_2 = n_3$) is the most symmetric solution the system admits, and when it bifurcates it gives way to solutions that necessarily

have a lesser degree of symmetry. Numerical evaluation of Eq. (2.4) reveals that these new solutions lie on one of the three (equivalent) lines $n_1 = n_2$, $n_1 = n_3$ and $n_2 = n_3$ (see also Fig. 2.3). We therefore turn our attention to solutions of Eq. (2.5) with the reduced symmetry $n_2 = n_3$. In the triangular plane $\sum n_k = 1$ of Fig. 2.3 this defines the dashed line from the lower left corner $\{1, 0, 0\}$ to the middle of the right-hand side of the triangle, $\{0, 1/2, 1/2\}$. With $n_2 = n_3 \equiv n$, $n_1 = 1 - 2n$, equation (2.5) takes the form:

$$\frac{dn}{dt} = F(1-2n) - F(n) = A\{(1-2n)^2 e^{-9B(1-2n)^2} - n^2 e^{-9Bn^2}\}, \qquad (2.6)$$

and cyclic permutations along the other two symmetry lines. For increasing values of B the maxima of $F(n)$ and $F(1-2n)$ move in opposite directions, and they go simultaneously through $n = 1/3$ at the value $B = 1$. It is precisely at this point that the uniform solution becomes unstable. The situation is depicted in Fig. 2.3 for four successive values of B.

At $B = 0.72$ (curve *a*) we see that dn/dt has only one zero (steady state) on the relevant interval $0 \leq n \leq 1/2$, namely, at $n = 1/3$. This solution is stable, as one can easily check from the sign of dn/dt. So regardless of the initial condition one always ends up in $\{1/3, 1/3, 1/3\}$: its basin of attraction (the shaded area in Fig. 2.3) is the whole plane $\sum n_k = 1$. Next, for $B = B_{sn} = 0.73$ (not shown), the function dn/dt touches zero at $n = 0.1255$. The index sn denotes that this involves a saddle-node bifurcation.

In curve *b*, at $B = 0.78$, we see that dn/dt has meanwhile gone through zero, creating one stable and one unstable steady state along the line $n_2 = n_3$. And, because of the threefold symmetry of the system, the same has happened along the lines $n_1 = n_2$ and $n_2 = n_3$. The three newly created stable steady states are single-peaked distributions. Also the uniform distribution is still stable, so in the present situation there are four co-existing stable states, each one surrounded by its own basin of attraction. The three *unstable* states move towards the center of the triangle, closing in upon $\{1/3, 1/3, 1/3\}$ and making its basin of attraction (the shaded area) smaller and smaller for increasing B.

Curve *c* depicts the situation for $B = B_{bif} = 1.00$. The three unstable states have just reached the point $\{1/3, 1/3, 1/3\}$, reducing its basin of attraction to zero. At this instant the uniform distribution turns unstable. So from now on all initial configurations end up in one of the three single-peaked distributions.

Curve *d*, at $B = 1.56$, gives an impression of the final situation. The basins of attraction of the three single-peaked states divide the triangle into three equal, kite-shaped parts. All the other steady states are unstable. The three states that have gone through the point $\{1/3, 1/3, 1/3\}$ are saddle points. Their stable branches

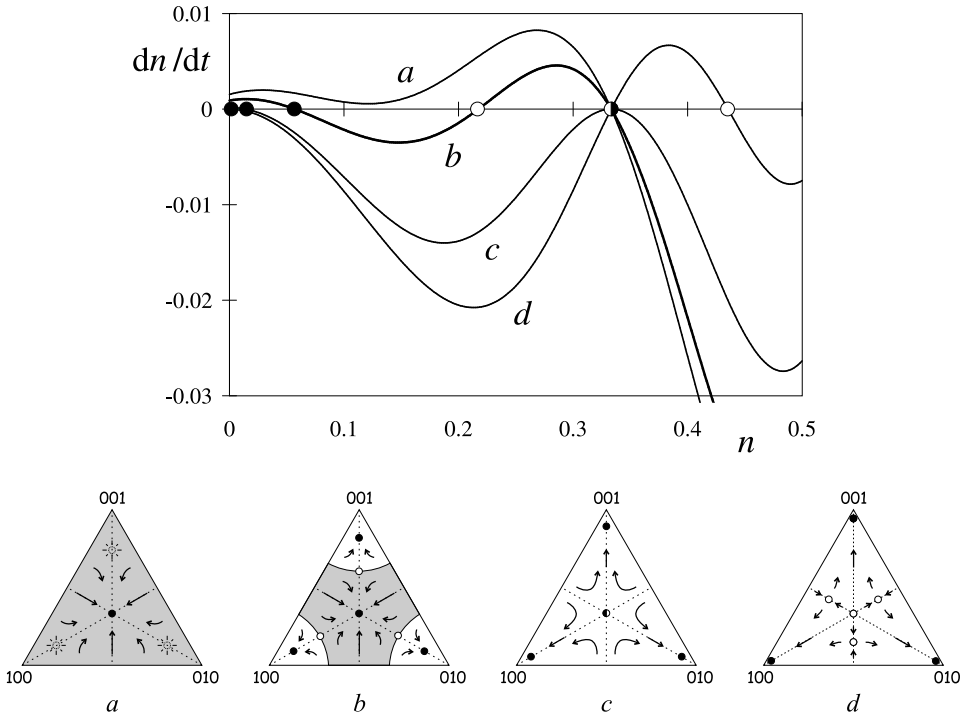

Figure 2.3: The rate of change dn/dt as function of n, along the symmetry axes of the 3-box system (cf. Eq. (6)), for four successive values of B, namely, a) $B = 0.72$, b) $B = 0.78$, c) $B = 1.0$, and d) $B = 1.56$. For each of these values a triangular fbw diagram is given, which shows the dynamics of the full system. The shaded area is the (diminishing) basin of attraction of the uniform solution $\{1/3, 1/3, 1/3\}$, in the center of the triangle; the white kites are the basins of attraction of the clustering solutions. Closed circles represent stable equilibria, open circles unstable equilibria.

lie along the symmetry lines (cf. the negative slope of dn/dt in Fig. 2.3) and their unstable branches in the perpendicular directions, as indicated in the triangular plot. So, starting out from the neighborhood of $\{1/3, 1/3, 1/3\}$, one first gets a situation where one box empties itself and two boxes are filled more or less equally, and only later one of these two boxes draws all the beads to itself.

The above sequence of events can be translated into the bifurcation diagram of Fig. 2.2. The uniform distribution is stable for $0 < B < 1$, and becomes unstable by means of an encounter with the unstable solutions. These have emerged from the saddle-node bifurcation at $B_{sn} = 0.73$, together with the stable single-peaked solutions. The latter solutions remain stable for all $B > 0.73$. In the interval $0.73 < B < 1$ both the uniform and the single-peaked distributions are stable and, depending on the initial conditions, the system can end up in either one of them. This bifurcation structure is very different from the $N = 2$ case, where the transition from uniform to single peaked distribution takes place (see Fig. 2.1) by means of a simple pitchfork bifurcation, meaning a 2nd order (continuous) phase transition. The most salient point of the 1st order (discontinuous) phase transition for $N = 3$ is indeed the hysteresis, just as found in the experiment. If one gradually increases the value of B from zero upwards (i.e, if one reduces the driving), the transition from uniform to single-peaked distribution takes place at $B_{bif} = 1$. If the value of B is then gradually turned down again, the reverse transition occurs at $B_{sn} = 0.73$.

Physically, this difference stems from the fact that the forward transition has more degrees of freedom at its disposal than the reverse one. The former can take place via any path through a 2D section of the flow diagram (see Fig. 3d) whereas the latter is confined to take place along one of the 1D symmetry lines (see Fig. 3a). For the 2-box system (where the flow diagram reduces to a line) there is no room for any difference of freedom between the forward and backward transition, and hence there is no hysteresis.

As for the quantitative agreement between theory and experiment, we note that the experimental result for the ratio B_{sn}/B_{bif} (≈ 0.88 for the results displayed in Fig. 2.2) is larger than the theoretical value 0.73. This can be explained from statistical fluctuations in the particle fractions (typically of order $1/\sqrt{P}$, and larger near a bifurcation), which in the neighborhood of $B = 1$ extend beyond the rapidly decreasing basin of attraction of the $\{1/3, 1/3, 1/3\}$ state, causing the system to switch prematurely to a single-peaked distribution. This means that in a series of experiments for increasing B, the measured bifurcation value B_{bif} will be smaller than the theoretical one. Analogously, in a series for decreasing B (with a single-peaked distribution as initial condition) the measured value for B_{sn} will be somewhat larger than in theory. Therefore, the experimentally determined ratio

B_{sn}/B_{bif} should actually be regarded as an upper bound. In addition, of course, it must be recalled that the flux function in Eq. (2.1) is approximate, and that the theoretical value of 0.73 is therefore an approximation, too. Any small changes in the function $F(n_k)$ will affect the ratio B_{sn}/B_{bif}, however not the qualitative properties of the model.

Not only the hysteresis, but also other features of the model show up in the experiment. In particular, the tendency to move from $\{1/3, 1/3, 1/3\}$ to a single-peaked distribution via a transient saddle-point state with two boxes filled almost equally (leaving the third one empty) is observed. For $B >> 1$ (i.e., at very mild driving) the system is even observed to be frozen in this transient state. Both half-filled compartments are so cold that the particles cannot cross the barrier anymore, which in the triangular diagrams corresponds to vanishingly small flux arrows around the saddle point.

In conclusion, we see that the clustering effect in the Maxwell-demon experiment with 3 cyclic compartments is hysteretic. This remains true if the system is made non-cyclic (e.g., by making one of the walls very high, or by putting the boxes in a linear row) and also if one takes more compartments ($N = 4, 5, 6, ..$). The uniform distribution still becomes unstable at the value $B_{bif} = 1$, but by then there is already a number of alternative solutions. Indeed, for growing N one gets increasingly complex patterns (multi-peak distributions) and the sensitive dependence on initial conditions becomes more prominent.

References

[1] I. Goldhirsch and G. Zanetti, *Clustering instability in dissipative gases*, Phys. Rev. Lett. **70**, 1619 (1993).

[2] S. McNamara and W.R. Young, *Inelastic collapse in 2 dimensions*, Phys. Rev. E **50**, R28 (1994).

[3] Y. Du, H. Li, and L.P. Kadanoff, *Breakdown of hydrodynamics in a one-dimensional system of inelastic particles*, Phys. Rev. Lett. **74**, 1268 (1995).

[4] H.M. Jaeger, S.R. Nagel, and R.P. Behringer, *The physics of granular materials*, Physics Today **49**, 32 (1996).

[5] H.M. Jaeger, S.R. Nagel, and R.P. Behringer, *Granular solids, liquids, and gases*, Rev. Mod. Phys. **68**, 1259 (1996).

[6] A. Kudrolli, M. Wolpert, and J.P. Gollub, *Cluster formation due to collisions in granular material*, Phys. Rev. Lett. **78**, 1383 (1997).

[7] L.P. Kadanoff, *Built upon sand: Theoretical ideas inspired by granular flows*, Rev. Mod. Phys. **71**, 435 (1999).

[8] J. Eggers, *Sand as Maxwell's demon*, Phys. Rev. Lett. **83**, 5322 (1999).

[9] H.J. Schlichting and V. Nordmeier, *Strukturen im Sand*, Math. Naturwiss. Unterr. **49**, 323 (1996).

[10] J.T. Jenkins and S.B. Savage, *A theory for the rapid flow of identical, smooth, nearly elastic, spherical particles*, J. Fluid Mech. **130**, 187 (1983).

[11] J.T. Jenkins and M.W. Richman, *Boundary conditions for plane flows of smooth nearly elastic circular discs*, J. Fluid Mech. **171**, 53 (1986).

[12] S. McNamara and S. Luding, *Energy flows in vibrated granular media*, Phys. Rev. E **58**, 813 (1998).

Chapter 3

Bifurcation Diagrams of Compartmentalized Granular Gases [‡]

The bifurcation diagram for a vibro-fluidized granular gas in N connected compartments is constructed and discussed. At vigorous driving, the uniform distribution (in which the gas is equi-partitioned over the compartments) is stable. But when the driving intensity is decreased this uniform distribution becomes unstable and gives way to a clustered state. For the simplest case, $N = 2$, this transition takes place via a pitchfork bifurcation but for all $N > 2$ the transition involves saddle-node bifurcations. The associated hysteresis becomes more and more pronounced for growing N. In the bifurcation diagram, apart from the uniform and the one-peaked distributions, also a number of multi-peaked solutions occur. These are transient states. Their physical relevance is discussed in the context of a stability analysis.

3.1 Introduction

One of the key features of a granular gas is the tendency to spontaneously separate into dense and dilute regions [1–6]. This clustering phenomenon manifests itself in a particularly clear manner in a box that is divided in a series of N connected compartments, with a hole (at a certain height) in the wall between each two adjacent

[‡]Published as: Devaraj van der Meer, Ko van der Weele, and Detlef Lohse, *Bifurcation Diagrams of Compartmentalized Granular Gases*, Phys. Rev. E **63**, 061304, pp. 1-9 (2001).

compartments. The system is vibro-fluidized by shaking the box vertically. With vigorous shaking the granular material is observed to be distributed uniformly over the compartments as in any ordinary molecular gas. Below a certain driving level however, the particles cluster in a small subset of the compartments, emptying all the others.

For $N = 2$ the transition from the uniform to the clustered state is of second order, taking place through a pitchfork bifurcation [7]. For $N = 3$ it was recently found that the transition is hysteretic. It is a first order phase transition, involving saddle-node bifurcations [8]. This difference has been explained by a flux model. In the present paper we will use the same flux model to construct the bifurcation diagrams for arbitrary N.

The main ingredient of this model is a flux function $F(n)$, which gives the outflow from a compartment to one of its neighbors as a function of the fraction of particles (n) contained in the compartment [7]. The function $F(n)$ starts out from zero at $n = 0$ and initially increases with n. At large values of n it decreases again because the particles lose energy in the non-elastic collisions, which become more and more frequent with increasing particle density. So $F(n)$ is non-monotonic, and that is why the flux from a well-filled compartment can balance that from a nearly empty compartment.

Assuming that the granular gas in each compartment is in thermal equilibrium at any time (in the sense of the granular temperature [9]) the following approximate form for $F(n)$ can be derived [7]:

$$F(n_k) = An_k^2 e^{-BN^2 n_k^2}, \tag{3.1}$$

which is a one-humped function, possessing the features discussed before (See Fig. 3.1). In the above equation n_k is the fraction of particles in the k-th compartment, normalized to $\sum n_k = 1$. The factors A and B depend on the number of particles and their properties (such as the radius, and the restitution coefficient of the interparticle collisions), on the geometry of the system (such as the placement and form of the aperture between the compartments), and on the driving parameters (frequency and amplitude). The factor A determines the absolute rate of the flux, and will be incorporated in the time scale, which thus becomes dimensionless. The clustering transition is governed only by B.

The time rate of change $\dot{n}_k$ of the particle fraction in the k-th compartment is given by the inflow from its two neighbours minus the outflow from the compartment itself,

$$\dot{n}_k = F(n_{k-1}) - 2F(n_k) + F(n_{k+1}), \tag{3.2}$$

with $k = 1, 2, .., N$. Here we have assumed that the interaction is restricted to neighboring compartments only.

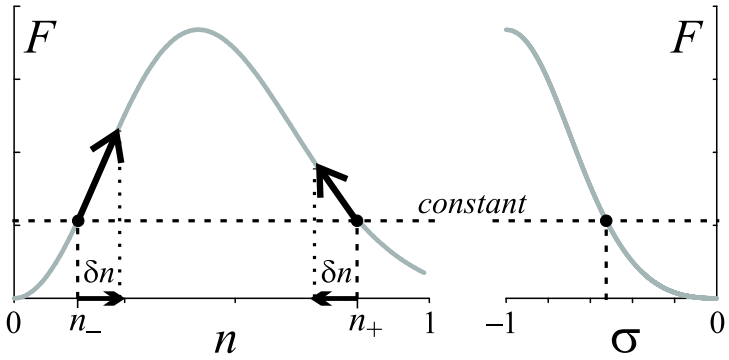

Figure 3.1: The solutions n_- and n_+ of $F(n_k) = constant$, cf. Eq. 3.5. Also shown is how the flux balance responds to an increase of n_- by an amount of δn (see also Eq. 3.11). The diagram on the right hand side depicts the relation between F and the quantity $\sigma = F'(n_+)/F'(n_-)$, which plays an important role in the stability analysis of Section 3.3.

For a cyclic arrangement the above equation is valid for all N compartments (with $k = N + 1$ equal to $k = 1$). If we take non-cyclic boundary conditions, by obstructing the flux between two of the compartments, the equation has to be modified accordingly for these compartments.

The total number of particles in the system is conserved ($\sum_k n_k = 1$), so

$$\sum_k \dot{n}_k = 0. \tag{3.3}$$

Statistical fluctuations in the system would add a noise term to Eq. (3.2), but we will not consider such a term here. So the present analysis has to be interpreted as a mean field theory for the system.

Equation (3.2) can also be written in matrix-form, as $\dot{\mathbf{n}} = \mathbf{M} \cdot \mathbf{F}$, or more explicitly:

$$\begin{aligned} \dot{n}_k &= \sum_l M_{kl} F(n_l) \\ &= \begin{pmatrix} -2 & 1 & 0 & 0 & \cdots & 0 & 1 \\ 1 & -2 & 1 & 0 & \cdots & 0 & 0 \\ 0 & 1 & -2 & 1 & \cdots & 0 & 0 \\ \vdots & \vdots & \vdots & \vdots & & \vdots & \vdots \\ 1 & 0 & 0 & 0 & \cdots & 1 & -2 \end{pmatrix} \cdot \begin{pmatrix} F(n_1) \\ F(n_2) \\ F(n_3) \\ \vdots \\ F(n_N) \end{pmatrix} \end{aligned} \tag{3.4}$$

The given matrix $\mathbf{M}$ corresponds to a cyclic arrangement of the N compartments. A similar matrix can be written down for the case of a non-cyclic arrange-

ment. We will come back to this later, when we will see that most of the results for the cyclic arrangement carry over to the non-cyclic case.

It is easily seen, from the fact that the elements of each row of $\mathbf{M}$ sum up to zero, that $\mathbf{1} = (1, 1, \ldots, 1)$ is an eigenvector. The corresponding eigenvalue $\lambda = 0$ physically reflects the fact that the compartments cannot all be filled (or emptied) simultaneously: $\sum_k \dot{n}_k = 0$ or $\sum_l M_{lk} = 0$. For future reference we note that all the other eigenvalues of $\mathbf{M}$ are negative (see Section 3.6).

The remainder of the paper is set up as follows. In Section 3.2 we show how to construct the bifurcation diagram, on the basis of Eq. (3.4), for an arbitrary number of compartments. In Section 3.3 we discuss the stability of the various branches in the diagram. Section 3.4 discusses the physical consequences resulting from the diagram, in particular in the limit for $N \to \infty$. Finally, Section 3.5 contains concluding remarks. The paper is accompanied by a mathematical appendix (Section 3.6), in which some essential results concerning the stability analysis are derived.

3.2 Constructing the bifurcation diagram

To calculate the bifurcation diagram, we have to find the fixed points of Eq. (3.4) as a function of the parameter B, i.e., those points for which $\dot{n}_k = \mathbf{M} \cdot \mathbf{F} = 0$. So $\mathbf{F}$ must be a multiple of the zero-eigenvalue vector $\mathbf{1} = (1, 1, \ldots, 1)$. This tells us that, in a stationary situation, all components of the flux vector $\mathbf{F}$ are equal: there is a detailed balance between all pairs of neighboring compartments. This rules out, for instance, the possibility of stable standing-wave-like patterns with equal but non-zero net fluxes throughout the system. The fixed point condition now becomes

$$\begin{cases} F(n_k) = \textit{constant} \\ \sum n_k = 1 \end{cases} \tag{3.5}$$

Since F is a one-humped function, $F(n_k) = constant$ has two solutions, which will be called n_- and n_+ (see Fig. 3.1). Every fixed point can be represented as a vector with elements n_- and n_+ (in any order, and summing up to 1) corresponding to a row of nearly empty and well-filled compartments. Let us call the number of well-filled compartments m. Apart from the ordering of the elements, every fixed point is then specified by only two numbers: n_+ and m.

Before actually calculating the bifurcation diagram, it is convenient to replace the fraction n by the (also dimensionless) variable $z = Nn\sqrt{B}$, as then the flux (3.1) simplifies to $F(z_k) \propto z_k^2 \exp(-z_k^2)$. The fixed point condition Eq. (3.5)

then reads:

$$\begin{cases} F(z_k) = \textit{constant} \\ \sum z_k = N\sqrt{B} \end{cases} \tag{3.6}$$

So the B-dependence has been transferred from **F** to the particle conservation, and this enables us to determine the entire bifurcation diagram from one single graph. This is illustrated in Fig. 3.2 for the case of N=5 compartments.

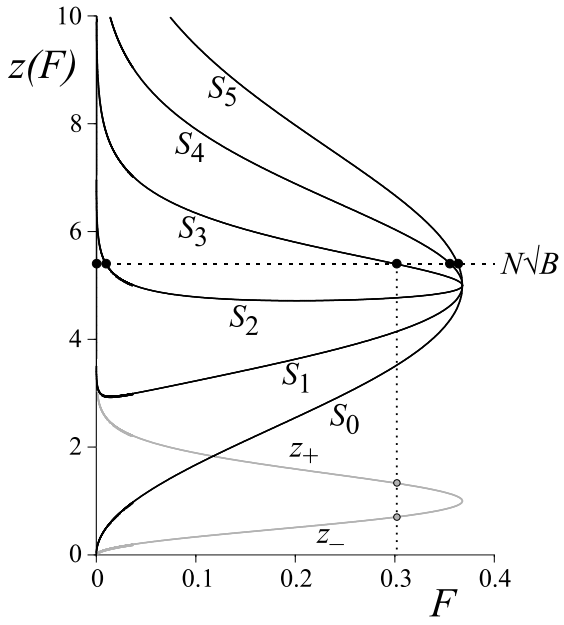

Figure 3.2: Inverted flux functions $z_-(F)$ and $z_+(F)$ and the $N+1$ sumfunctions $S_m(F) = mz_+(F) + (N-m)z_-(F), m = 0, 1, \ldots, N$. Here we picked $N = 5$. The points of intersection with the horizontal line $z = N\sqrt{B}$ represent the fixed points for the parameter value B. Curves S_0 and S_5 correspond to the uniform distribution (below and above the critical point $B = 1$, respectively) and the other curves belong to clustered states. Note that S_0 joins smoothly with S_5 at $B = 1$ (i.e. $z = N\sqrt{B} = 5$), and so does S_1 with S_4, and S_2 with S_3.

First, the one-humped function $F(z)$ is inverted separately on both sides of the maximum, yielding the functions $z_-(F)$ and $z_+(F)$. Then, we construct the sumfunctions:

$$S_m(F) = m\, z_+(F) + (N-m)\, z_-(F) \tag{3.7}$$

Now, from Eq. (3.6), the fixed points are found by intersecting the horizontal line $z = N\sqrt{B}$ with the sumfunctions $S_m(F)$. In Fig. 3.2 this is done for

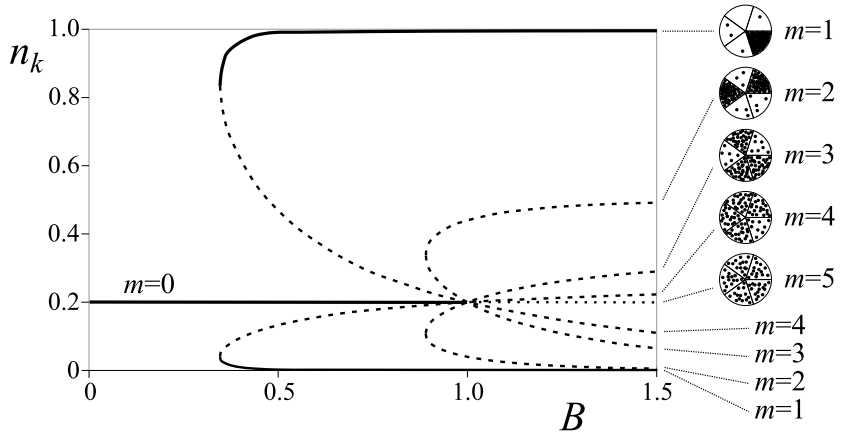

Figure 3.3: Bifurcation diagram for $N = 5$. It has been obtained from Fig. 3.2 by converting, for all B, each $\{z_-, z_+\}$-pair belonging to a point of intersection to a $\{n_-, n_+\}$-pair. Note that all branches come together at the critical point $B = 1$. The (stable) $m = 0$ branch becomes the (unstable) $m = 5$ branch, the $m = 1$ branch turns into the $m = 4$ branch, and $m = 2$ switches to $m = 3$.

B=1.08. Each intersection point yields a pair $\{z_-, z_+\}$, or equivalently $\{n_-, n_+\}$. Repeating the procedure for all B, we obtain the bifurcation diagram depicted in Fig. 3.3.

It contains several branches. First, a horizontal line (from the sumfunctions S_0 and S_5) corresponding to the equal distribution $n_+ = n_- = 0.2 = 1/N$. Second, the branches corresponding to the $m = 1$ clustered state (from S_1), which at $B = 1$ goes over into the $m = 4$ state (from S_4). And third, the branch of the $m = 2$ clustered state (from S_2), which at $B = 1$ becomes the $m = 3$ state. The physical appearance of these solutions is sketched in the small diagrams. Note that only the $m = 0$ branch (i.e., the uniform solution up to $B = 1$) and the outer $m = 1$ branch are stable. All the other branches are unstable, as will be discussed in the next section.

At $B = 1$, where the branches intersect with the uniform distribution $n_+ = n_- = 1/N$, we have a critical point. In the flux function one passes the maximum here. This means that n_+ and n_- are switched (relatively empty compartments become relatively filled, and vice versa), so m-branches change into $(N - m)$-branches. From a physical point of view, the most important thing that happens at the $B = 1$ intersection point is the destabilization of the uniform distribution.

The saddle-node bifurcations of the $m = 1$ and $m = 2$ branches correspond to the minima of the sumfunctions S_1 and S_2 respectively, which in Fig 3.2 can be seen to occur at $F \approx 0.014$ for S_1 and $F \approx 0.202$ for S_2. In general, if a sumfunction $S_m(F)$ has a minimum for a certain B, the associated m branch will have a bifurcation. So the bifurcation condition is that the derivative $dS_m(F)/dF$ equals zero, or equivalently:

$$\frac{\left(\frac{dz_-}{dF}\right)}{\left(\frac{dz_+}{dF}\right)} = -\frac{m}{N-m} \tag{3.8}$$

Not surprisingly, the quantity on the left hand side ($dz_-/dz_+ \equiv \sigma$) will play an important role in the stability analysis of the next section.

3.3 Stability of the branches

The stability of the branches (i.e., of the fixed points) is determined by the eigenvalues of the Jacobi matrix **J** corresponding to Eq. (3.4), with components:

$$J_{jk} = \frac{\partial \dot{n}_j}{\partial n_k} = \sum_l M_{jl} F'(n_l) \frac{\partial n_l}{\partial n_k} = M_{jk} F'(n_k) \tag{3.9}$$

Here F' denotes the derivative of F with respect to n. Note that the Jacobi matrix can also be written as the product of $\mathbf{M}$ and the diagonal matrix $\mathbf{D} = \mathrm{diag}(F'(n_1), \ldots, F'(n_N))$, see also Eq. (3.18) in the Appendix. For a fixed point the only diagonal elements that occur are $F'(n_+)$ (m times) and $F'(n_-)$ ($N - m$ times), in any order. The ratio between these two functions is precisely the quantity we encountered earlier in the bifurcation condition Eq. (3.8), namely σ:

$$\sigma = \frac{F'(n_+)}{F'(n_-)} = \frac{dn_-}{dn_+} \tag{3.10}$$

The Jacobi matrix **J** has N eigenvalues, one of which is always zero. The other $N - 1$ eigenvalues depend on m and the value of σ.

For $m = 0$ (the equipartitioned state) all non-trivial eigenvalues are negative, up to the point $B = 1$. This can be seen either by direct numerical calculation, or analytically (see Appendix). At $B = 1$, the $m = 0$ state becomes the $m = N$ state. Here, the functions F' in the Jacobi matrix (3.9) change sign, and so do all of its eigenvalues. So suddenly the uniform state has $N - 1$ *positive* eigenvalues, which

implies a high degree of instability. Only in the limit $B \to \infty$ does the uniform state regain some of the lost terrain: the magnitude of all positive eigenvalues tends to zero here. Physically speaking, in this limit the vibro-fluidization is too weak to drive the particles out of the boxes anymore.

As for the other values of m, in Fig. 3.4 we have plotted the numerically evaluated eigenvalues (as functions of σ) for the system with $N = 5$ compartments.

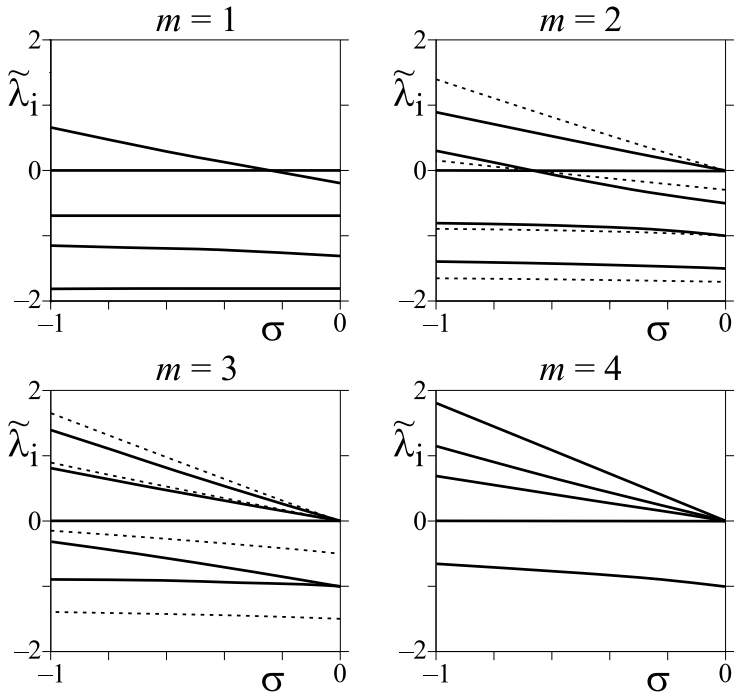

Figure 3.4: Eigenvalues of the Jacobi matrix **J** as a function of σ, for the branches m = 1, 2, 3, and 4. Rather than plotting λ_i, we display $\tilde{\lambda}_i = \lambda_i / F'(n_-)$, because this yields a more clear-cut picture. Negative eigenvalues represent stable directions of the branches, and positive eigenvalues represent unstable ones. A zero crossing (such as for $m = 1$ and $m = 2$) indicates the occurrence of a saddle-node bifurcation. The value $\sigma = 0$ corresponds to the limit $B \to \infty$, and $\sigma = -1$ to the critical point $B = 1$. At this point, the eigenvalues of $m = 1$ and $m = 4$ are equal but opposite in sign: the transition from the one branch to the other is marked by a distinct drop in stability. The same is true for the eigenvalues of $m = 2$ and $m = 3$, and also (not depicted) for those of $m = 0$ and $m = 5$. For m = 2, 3 there are two different cluster-confi gurations, with different eigenvalues. The dashed lines correspond to $\{+ + - - -\}$ for $m = 2$, which goes over into $\{- - + + +\}$ for $m = 3$. The bold lines apply to the slightly more stable confi gurations $\{+ - + - -\}$ and $\{- + - + +\}$.

For $m = 1$, we see that there are three eigenvalues that are always negative. The fourth non-trivial eigenvalue changes sign at $\sigma = -1/4$. This corresponds to the saddle-node bifurcation of the $m = 1$ branch in the bifurcation diagram (Fig. 3.3), and the bifurcation value of σ is in agreement with Eq. (3.8). The region to the right of $\sigma = -1/4$ (where all non-trivial eigenvalues are negative) belongs to the stable outer branch. The left part $\sigma < -1/4$ belongs to the unstable inner branch, up to the point $B = 1$ (at $\sigma = -1$), where the $m = 1$ branch goes over into the $m = 4$ branch. That is, the state $\{+ - - - -\}$ now switches to $\{- + + + +\}$. At the same time all eigenvalues change sign, so suddenly we have 3 positive eigenvalues, which is only one less than for the uniform $m = 5$ state. (Indeed, the only stable manifold of the $m = 4$ fixed point comes from the direction of the completely unstable $m = 5$ state). The positive eigenvalues never cross zero anymore (there are no bifurcations beyond $B = 1$) but, as before, in the limit $B \to \infty$ ($\sigma \to 0$) they go to zero.

For $m = 2$ there are two possible configurations: $\{+ + - - -\}$ and $\{+ - + - -\}$. Due to the cyclic symmetry, all other combinations are equivalent to these two. The eigenvalues of the first configuration are given by the dotted lines, and those of the second by the solid lines. Although they are very similar (and are represented by exactly the same branch in the bifurcation diagram), it is clear that the second configuration is the more stable of the two. Apparently the two well-filled compartments prefer to keep a distance.

The saddle-node bifurcation of the $m = 2$ branch takes place at $\sigma = -2/3$ [cf. Eq. (3.8)], where the third non-trivial eigenvalue goes through zero. The fourth non-trivial eigenvalue always remains positive, indicating that the $m = 2$ branch never becomes completely stable. (As a matter of fact, only the $m = 0$ branch and part of the $m = 1$ branch can be completely stable). Note that for $\sigma \to 0$ (large B) the positive eigenvalue tends to zero, so the degree of instability is quite weak there.

At $B = 1$ the $m = 2$ branch becomes the $m = 3$ branch, with the two configurations $\{- - + + +\}$ and $\{- + - + +\}$, and with all eigenvalues switching sign. As we see, the more dispersed configuration is again the less unstable one. Also the phenomenon of all positive eigenvalues going to zero as σ approaches zero (the weak driving limit $B \to \infty$) is again apparent.

In the present example for $N = 5$, and in fact for all odd values of N, the branches in the bifurcation diagram are all born by means of a saddle-node bifurcation. But for *even* values of N this is different: in that case there is one branch-pair that springs from the uniform distribution, at $B = 1$, by a *pitchfork* bifurcation. This is illustrated in Fig. 3.5 for $N = 6$. Here one sees all the branches that were present already for $N = 5$, only slightly shifted towards the left, plus an additional

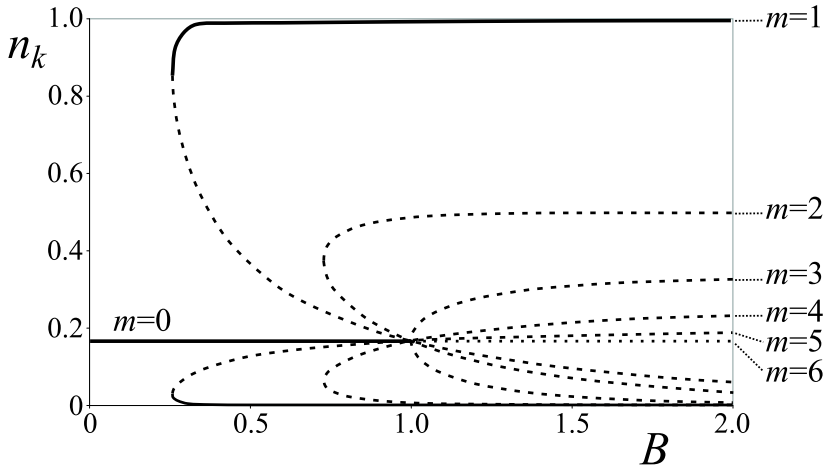

Figure 3.5: Bifurcation diagram for $N = 6$. Note the pitchfork bifurcation at $B = 1$.

pair of branches ($m = 3$) bifurcating in the forward direction from $B = 1$.

The special status of the branch $m = N/2$ is also evident from Eq. (3.8), which tells us that the bifurcation condition for this branch is $\sigma = -1$. This condition is fulfilled only by $n_+ = n_- = 1/\sqrt{B} = 1/N$. So, unlike all other branches, this one originates at $B = 1$ from the (until then stable) uniform state. Related to this, the branch is the only one that is symmetric for interchanging n_+ and n_-.

3.4 Physical aspects

The bifurcation analysis from the previous section can also be understood from a more physical point of view. To this end, let us first have a closer look at a 2-box system. In the equilibrium situation the net flux between the two boxes is zero, with one filled (n_+) and one nearly empty (n_-) box. Suppose the level of the empty box is raised by an amount δn. The level of the filled box then decreases by an equal amount and the net flux $\phi_{-\to+}$ from the empty to the filled box becomes (see also Fig. 3.1):

$$\begin{aligned} \phi_{-\to+} &= F(n_- + \delta n) - F(n_+ - \delta n) \\ &= \left(\frac{dF}{dn_-} + \frac{dF}{dn_+} \right) \delta n = (1+\sigma) \, \frac{dF}{dn_-} \delta n \end{aligned} \tag{3.11}$$

where we have used that $\sigma = dn_-/dn_+$ and neglected the higher order terms in the Taylor expansion. There are two different regimes. If $\sigma > -1$, the net flux

is positive (as $F'(n_-)$ is always positive), so particles are flowing from n_- to n_+, restoring the equilibrium position. This is actually the situation along the entire $m = 1$ branch, for all $1 < B < \infty$. For $\sigma < -1$ (a situation which does not occur for our choice of F), the net flux would be negative, raising the level of the emptier box even further, away from the equilibrium position. In the borderline case, $\sigma = -1$ (at $B = 1$), the system is indifferent to infinitesimal changes.

This argument is readily generalized to the N-compartment system, for an equilibrium with m filled boxes. Now we raise the level of all $N - m$ nearly empty boxes simultaneously by δn. This is done by lowering all levels in the m filled boxes by an equal amount, which by particle conservation must be equal to $\delta n(N-m)/m$. The equivalent of Eq. (3.11) for the flux between any of the empty boxes to a neighbouring filled box then reads:

$$\begin{aligned} \phi_{-\to+} &= F(n_- + \delta n) - F(n_+ - \frac{N-m}{m}\delta n) \\ &= \left(\frac{dF}{dn_-} + \frac{N-m}{m}\frac{dF}{dn_+}\right)\delta n \\ &= \left(\frac{m}{N-m} + \sigma\right)\frac{dF}{dn_-}\delta n \end{aligned} \tag{3.12}$$

From this expression it follows that the transition between a (relatively) stable ($\sigma > -m/(N-m)$) and a (relatively) unstable ($\sigma < -m/(N-m)$) configuration is marked by the bifurcation condition Eq. (3.8). So, by straightforward physical reasoning we have reproduced the exact result obtained earlier from an eigenvalue analysis.

The pitchfork bifurcation discussed at the end of Section 3.3 is especially important for $N = 2$. In this case it is the *only* non-uniform branch. To be specific, it is a stable $m = 1$ branch. This $N = 2$ case [7] is the only one without any saddle-node bifurcations, and consequently it is the only case where the change from the uniform to the clustered situation takes place via a second order phase transition without any hysteresis. For all $N > 2$ the transition is of first order [8], and shows a hysteretic effect that becomes more pronounced for growing N.

In the limit $N \to \infty$ the hysteresis is maximal: the first saddle-node bifurcation takes place immediately after $B = 0$, and this means that there exists a stable $m = 1$ solution over the entire range $B > 0$. So, if one starts out from this solution (at a certain value of B) and then gradually turns down B, one will never witness the transition to the uniform distribution. Vice versa, also the transition from the uniform solution to the $m = 1$ state will not occur in practice, even though the uniform distribution becomes unstable at $B = 1$. If one starts out from the uniform solution (at a certain value of B below 1) and increases B, one will witness the

transition to a clustered state, but in practice this will always be one with a number of peaks. That is, the system gets stuck in a transient state with $m > 1$, even though such a state is not stable (it has one or more positive eigenvalues).

The fact is that its lifetime may be exceedingly large, since the flux in the neighborhood of a peak and its adjacent boxes (which are practically empty) is very small. Furthermore, the communication between the peaks is so poor that usually (even for moderate values of N) the dynamics comes to a standstill in a state with peaks of unequal height.

Another point we would like to address is that practically the transition to a clustered state will take place already before $B = 1$, because the solution is kicked out of its basin of attraction by the statistical fluctuations in the system [8]. An example is shown in Fig. 3.6. Here we see a snapshot for the cyclic system with $N = 80$ compartments, which were originally filled almost uniformly, at $B = 0.90$. The small random fluctuations in the initial condition are sufficient to break away from the (still stable) uniform distribution, and one witnesses the formation of a number of isolated clusters. In the further evolution these clusters deplete the neighbouring compartments and indeed the whole intermediate regions. But the peaks themselves, once they are well-developed, do not easily break down anymore.

3.5 Concluding remarks

In this paper we have constructed the bifurcation diagram for a vibro-fluidized granular gas in N connected compartments. Let us now comment upon the result.

Starting out from $B = 0$, i.e, vigorous shaking, the equi-partitioned state is for some time the only (and stable) fixed point of the system. For increasing B we first come upon the $m = 1$ bifurcation, where the single-cluster state is born. For all $N > 2$ this happens by means of a saddle-node bifurcation, creating one completely stable state and one unstable state (with 1 positive eigenvalue). The one with the largest difference between n_+ and n_- is the stabler one of the two states. Strictly speaking, there are N equivalent single-cluster states, since the cluster can be in any of the N compartments.

For further growing B we come across the $m = 2$ bifurcation, where two unstable 2-peaked states are created. The state with the largest difference between n_+ and n_- has 1 positive eigenvalue, and the other one 2. The two peaks can be distributed in $\binom{N}{2}$ ways over the N compartments, but as we have seen they are not all equivalent. When the peaks are situated next to each other we have a more unstable situation (the positive eigenvalues are larger in magnitude) than when the

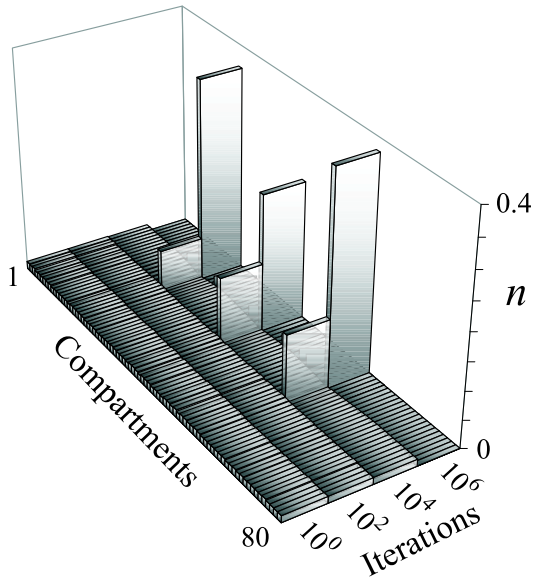

Figure 3.6: Results from a numerical solution of Eq. (3.4) for $N = 80$, at $B = 0.90$. Snapshots are taken after 10^0, 10^2, 10^4 and 10^6 timesteps (iterations). Between 100 and 10,000 iterations a clustering pattern is seen take shape. Although strictly speaking this is a transient state, the system gets stuck in it.

peaks are further apart. This is generally true for m-peaked solutions: of the $\binom{N}{m}$ ways in which m peaks can be distributed, the ones in which the peaks are next to each other are the least favorable of all.

For increasing B we encounter more and more bifurcations, where unstable m-clustered states come into existence (each with 1 more positive eigenvalue than the previous one), and for large N the bifurcation diagram is covered by a dense web of branches. In Fig. 3.7 this is shown for N=80. The last saddle-node bifurcation takes place shortly before $B = 1$ and, for this even value of N, is followed by a final pitchfork bifurcation (creating the $m = N/2$ branch) at $B = 1$.

The uniform solution (or $m = 0$ state) is stable until $B = 1$, with $N - 1$ negative eigenvalues and 1 zero. For $B > 1$ all its negative eigenvalues become positive, making it suddenly the most unstable state of all. Also, it now formally becomes the $m = N$ state. Moving away from this uniform solution one encounters first the $m = N - 1$ branch with $N - 2$ positive eigenvalues, then the $m = N - 2$ branch with $N - 3$ positive eigenvalues, etc. Finally, one arrives at the outermost $m = 1$ branch, which has no positive eigenvalues. This is the only

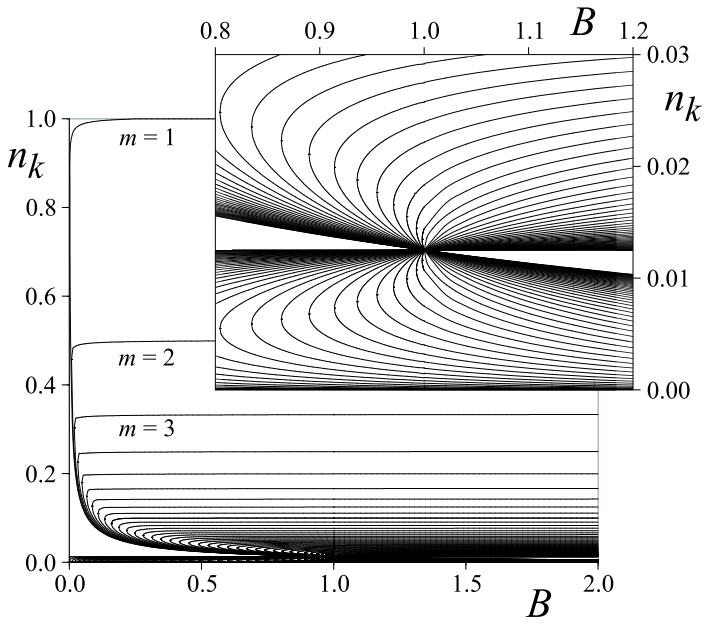

Figure 3.7: Bifurcation diagram for $N = 80$. The hysteresis extends almost all the way down to $B = 0$, and there are numerous transient states (cf. Fig. 3.6). The only strictly stable branches are the $m = 0$ branch (up to $B = 1$) at $n_k = 1/N$, and the outer $m = 1$ branches. Naturally, the upper $m = 1$ branch approaches $n_k = 1$, the upper $m = 2$ branch approaches $n_k = 1/2$, the upper $m = 3$ branch $n_k = 1/3$, etc. The overlay picture shows the neighborhood of the critical point at $B = 1, n_k = 1/N$ in more detail.

solution that is completely stable for $B > 1$. But as we have seen in the previous section, on its way from the uniform distribution to the single peaked state, the system can easily get stuck in one of the transient states (especially for large N) even though these are not strictly stable.

Throughout the paper, we have concentrated on the case where the N compartments are arranged in a cyclic manner. But in doing so, we have in fact also solved the non-cyclic case. Here we close the hole in the wall between the 1st and Nth compartment, and consequently the flux between them is zero. The matrix $\mathbf{M}$ then takes the following form [differing from the cyclic one only in the first and last

row, cf. Eq. (3.4)]:

$$\mathbf{M}^{(nc)} = \begin{pmatrix} -1 & 1 & 0 & 0 & \cdots & 0 & 0 \\ 1 & -2 & 1 & 0 & \cdots & 0 & 0 \\ 0 & 1 & -2 & 1 & \cdots & 0 & 0 \\ \vdots & \vdots & \vdots & \vdots & & \vdots & \vdots \\ 0 & 0 & 0 & 0 & \cdots & -2 & 1 \\ 0 & 0 & 0 & 0 & \cdots & 1 & -1 \end{pmatrix} \tag{3.13}$$

The eigenvalue problem for this matrix is treated in the Appendix. One eigenvalue is identically zero, and the other $N-1$ eigenvalues are negative, just like for the cyclic system. This leads to a bifurcation diagram that is indistinguishable from that of the cyclic case. Even the stability along the branches is the same; only the magnitude (not the sign) of the eigenvalues of the Jacobi-matrix **J** is slightly different for the two cases.

Finally, it should be emphasized that the results of the present paper do not depend on the precise form of the flux function. We have concentrated on the form given by Eq. (3.1), but virtually everything remains true for other choices of this function, as long as it is a non-negative, one-humped function, starting out from zero at $n = 0$ (no flux if there are no particles) and going down to zero again for very many particles (no flux also in this limit, since - due to the inelastic collisions - the particles form an inactive cluster, unable to reach the hole in the wall anymore). Any function with these properties will produce a bifurcation diagram similar to that of Eq. (3.1).

In the likely case that the range of $\sigma = dn_-/dn_+$ is the same, extending from -1 (this value is attained in the maximum) to zero (in the outer regions of the flux function, for $n_-\sqrt{B} \to 0$, $n_+\sqrt{B} \to \infty$), the bifurcation diagram will have the same number of saddle-node bifurcations and the same number of branches. The only things that change are the exact position of the bifurcation points, and the magnitude of the eigenvalues along the branches.

Slight differences in the diagram would occur if the slope of F on the n_+ side was to become steeper than on the n_- side. In that case, the bifurcation condition Eq. (3.8) would also have solutions for $m > N/2$, thus allowing saddle-node bifurcations for branches with $m > N/2$. These branches, however, would certainly be quite unstable.

3.6 Appendix: On the eigenvalues of M and J

In this appendix we present the analytical eigenvalues of the flux matrix **M** [introduced in Eqs. (3.4) and (3.13)] and discuss the eigenvalue problem for the Jacobian matrix **J** [see Eq. (3.9)], thereby determining the stability of the branches in the bi-

furcation diagram.

First, we briefly treat the eigenvalues of $\mathbf{M}$. After that, we turn to $\mathbf{J}$. In Subsection 3.6.2 we discuss its zero-eigenvalues: one eigenvalue is identically zero and, by pinpointing the zero-crossing of a second eigenvalue, we reproduce the bifurcation condition Eq. (3.8). In Subsection 3.6.3 we determine the number of negative eigenvalues of $\mathbf{J}$ in the low-driving limit $\sigma \to 0$. Likewise, in Subsection 3.6.4 we determine the number of positive eigenvalues in the (mathematical) limit $\sigma \to -\infty$. Combining these two results, in Subsection 3.6.5, we finally find the number of positive eigenvalues of $\mathbf{J}$ for general values of σ, and this gives the stability of the branches over the entire bifurcation diagram.

3.6.1 Eigenvalues of matrix $\mathbf{M}$

The matrix $\mathbf{M}$ in Eq. (3.4) is closely related to the $N \times N$ tridiagonal matrix $\mathrm{tridiag}(1, -2, 1)$ associated with the second difference operator known from numerical schemes for solving second order pde's. Its eigenvalue problem can be solved exactly [10], and the same is true for $\mathbf{M}$. The eigenvalues of $\mathbf{M}$ are given by:

$$\lambda_k = -4 \sin^2 \left(\frac{k\pi}{N} \right) \tag{3.14}$$

where k runs from 0 to $N/2$ for N even, and from 0 to $(N-1)/2$ for N odd. The corresponding eigenvectors are:

$$a_i(k) = C_1 \cos \left(\frac{(2i+1)k\pi}{N} \right) + C_2 \sin \left(\frac{(2i+1)k\pi}{N} \right) \tag{3.15}$$

with $i = 1, \ldots, N$ and arbitrary coefficients C_1 and C_2.

As we see, the first eigenvalue ($k = 0$) is zero and the corresponding eigenvector is $\mathbf{1} = (1, 1, \ldots, 1)$. Physically, this eigenvector represents simultaneous filling of all N compartments, and the eigenvalue 0 expresses the fact that this is prohibited (because the number of particles in our system is conserved).

All non-zero eigenvalues are negative and (except the one for $k = N/2$ in the case of even N) doubly degenerate. This means that the corresponding eigenvectors span a two-dimensional subspace, reflected by the two terms C_1 and C_2 in Eq. (3.15). Since $\mathbf{M}$ is symmetric, and therefore normal, linear subspaces corresponding to different eigenvalues are orthogonal. Especially, the eigenvectors of all non-zero eigenvalues span a $N - 1$ dimensional subspace perpendicular to $\mathbf{1} = (1, 1, \ldots, 1)$.

The matrix $\mathbf{M}^{(nc)}$ for the non-cyclic case, given by Eq. (3.13), has a different set of eigenvalues:

$$\lambda_k^{(nc)} = -4\sin^2\left(\frac{k\pi}{2N}\right) \tag{3.16}$$

Here k runs from 0 to $N-1$. The corresponding eigenvectors are:

$$a_i^{(nc)}(k) = \cos\left(\frac{(2i+1)k\pi}{2N}\right) \tag{3.17}$$

Just like in the cyclic case, the first eigenvalue equals zero, and all the others are negative. However, they are non-degenerate and the corresponding eigenspaces are one-dimensional.

3.6.2 Zero-eigenvalues of matrix J

Now we turn to the Jacobian matrices. We consider the cyclic version $\mathbf{J}$, with components as given in Eq. (3.9), but the results are also valid for the non-cyclic version. This matrix can be written as the product of $\mathbf{M}$ and a diagonal matrix $\mathbf{D} = \mathrm{diag}(F'(n_1), F'(n_2), \ldots, F'(n_N))$:

$$\mathbf{J} = \mathbf{M}\cdot\mathbf{D} = \begin{pmatrix} -2F'(n_1) & F'(n_2) & 0 & \cdots & 0 & F'(n_N) \\ F'(n_1) & -2F'(n_2) & F'(n_3) & \cdots & 0 & 0 \\ 0 & F'(n_2) & -2F'(n_3) & \cdots & 0 & 0 \\ \vdots & \vdots & \vdots & & \vdots & \vdots \\ 0 & 0 & 0 & \cdots & -2F'(n_{N-1}) & F'(n_N) \\ F'(n_1) & 0 & 0 & \cdots & F'(n_{N-1}) & -2F'(n_N) \end{pmatrix} \tag{3.18}$$

In the context of the bifurcation diagram, the main thing one wants to know is the number of positive eigenvalues of $\mathbf{J}$ for each branch. This is what we are going to determine now.

First we note that the eigenvalues of $\mathbf{J}$ are real, even though the matrix is not symmetric. This is a consequence of the following similarity relationship between $\mathbf{J}$ and $\mathbf{J}^\dagger$:

$$\mathbf{J}^\dagger = (\mathbf{M}\cdot\mathbf{D})^\dagger = \mathbf{D}\cdot\mathbf{M} = \mathbf{D}\cdot(\mathbf{M}\cdot\mathbf{D})\cdot\mathbf{D}^{-1} = \mathbf{D}\cdot\mathbf{J}\cdot\mathbf{D}^{-1} \tag{3.19}$$

This implies that $\mathbf{J}$ and $\mathbf{J}^\dagger$ have the same eigenvalues, and hence they must be real. Because $\mathbf{M}$ is singular, $\mathbf{J}$ must be too (it has a zero eigenvalue) and so its determinant $\det(\mathbf{J})$ is zero. More explicitly:

$$\det(\mathbf{J}) = \det(\mathbf{M})\cdot\det(\mathbf{D}) = \left(\prod_k F'(n_k)\right)\det(\mathbf{M}) = 0 \tag{3.20}$$

where, for a fixed point with m filled compartments, the product term equals $[F'(n_+)]^m[F'(n_-)]^{(N-m)}$.

For the other eigenvalues we have to look at the characteristic equation $\det(\mathbf{J}-\lambda\mathbf{I})=0$. This is a polynomial expression in λ, of which the constant term is zero since it is equal to $\det(\mathbf{J})$. The coefficient L of the linear term is:

$$L=\sum_k \det(\mathbf{J}^{(k,k)})=\sum_k\left(\prod_{l\neq k}\lambda_l\right) \tag{3.21}$$

where the matrix $\mathbf{J}^{(k,k)}$ is the $(N-1)\times(N-1)$ matrix obtained from $\mathbf{J}$ by deleting its k-th row and its k-th column. In the right-hand side of this equation, the only product that survives is the one that does not contain the trivial (zero) eigenvalue. So:

$$L=\prod_{\text{all non-trivial}\lambda_l}\lambda_l \tag{3.22}$$

Alternatively, the determinant of $\mathbf{J}^{(k,k)}$ in Eq. (3.21) can be written in terms of $\det(\mathbf{M}^{(k,k)})$, by deleting the k-th factor from the product in Eq. (3.20):

$$L=\sum_k\left(\prod_{l\neq k}F'(n_l)\right)\det(\mathbf{M}^{(k,k)}) \tag{3.23}$$

It can be shown that for all k the determinant $\det(\mathbf{M}^{(k,k)})$ is a constant, C, which equals $(N-1)(-1)^{N-1}$ in the cyclic, and $(-1)^{N-1}$ in the non-cyclic case. Thus, Eq. (3.23) reduces to:

$$L=C\sum_k\left(\prod_{l\neq k}F'(n_l)\right) \tag{3.24}$$

For a fixed point with m filled compartments, we can write (using that in the above summation each of the products misses either an $F'(n_+)$ or an $F'(n_-)$):

$$\begin{aligned} L &= C[F'(n_+)]^{(m-1)}[F'(n_-)]^{(N-m-1)}\times \\ &\qquad\Big((N-m)F'(n_+)-mF'(n_-)\Big) \\ &= C[F'(n_+)]^{(m-1)}[F'(n_-)]^{(N-m)}\Big((N-m)\sigma-m\Big) \end{aligned} \tag{3.25}$$

From this equation we conclude that L becomes zero at $\sigma=-m/(N-m)$. This is exactly the bifurcation condition already given in the main text [Eq. (3.8)]. Also, with Eq. (3.22), we see that an eigenvalue crosses zero at this value of σ.

It can be shown, by a similar analysis, that the coefficient of the quadratic term is not equal to zero at $\sigma = -m/(N-m)$, so not more than one of the eigenvalues changes sign at the bifurcation.

3.6.3 Number of negative eigenvalues of J for $\sigma \to 0$

We now come to the next step in determining the number of positive eigenvalues. We again use the definition of σ to write: $\mathbf{J} = F'(n_-)\mathbf{M} \cdot \widetilde{\mathbf{D}}$, where $\widetilde{\mathbf{D}} = \mathrm{diag}(1, \ldots, 1, \sigma, \ldots, \sigma)$. The factors 1 correspond to the $N-m$ nearly empty boxes and the factors σ to the m filled boxes. The precise ordering of the factors is not essential for the following argument, so we may choose the above order for notational convenience.

The factor $F'(n_-)$ is always positive, so we only have to deal with $\mathbf{M} \cdot \widetilde{\mathbf{D}}$. Note that only $\widetilde{\mathbf{D}}$ depends on σ and that in the limit $\sigma \to 0$ this matrix becomes*:

$$\lim_{\sigma \to 0} \widetilde{\mathbf{D}} = \mathrm{diag}(1, \ldots, 1, 0, \ldots, 0) \equiv \mathbf{P} \tag{3.26}$$

$\mathbf{P}$ is a projection matrix which projects $\mathbb{R}^N$ to the subspace spanned by the first $N-m$ unit vectors. It is obviously singular, symmetric, and applying it twice gives the same result as once: $\mathbf{P}^2 = \mathbf{P}$.

Instead of taking the matrix $\mathbf{J}_0 = \mathbf{M} \cdot \mathbf{P}$ as input for solving our eigenvalue problem (in the limit $\sigma \to 0$), we will rather look at the matrix $\mathbf{P} \cdot \mathbf{M} \cdot \mathbf{P}$ which is symmetric and has the same eigenvalues as $\mathbf{J}_0$.

For proof of the last statement, let μ be a (non-zero) eigenvalue of $\mathbf{J}_0$: $\mathbf{J}_0 \cdot \mathbf{x} = \mu\mathbf{x}$. Then: $(\mathbf{P} \cdot \mathbf{M} \cdot \mathbf{P}) \cdot (\mathbf{P} \cdot \mathbf{x}) = \mathbf{P} \cdot (\mathbf{M} \cdot \mathbf{P} \cdot \mathbf{x}) = \mu(\mathbf{P} \cdot \mathbf{x})$. Note that $\mathbf{P} \cdot \mathbf{x} \neq 0$, because otherwise also $\mathbf{J}_0 \cdot \mathbf{x} = \mathbf{M} \cdot \mathbf{P} \cdot \mathbf{x}$ would be zero, contradicting the assumption that μ is non-zero. This completes the proof.

The matrix $\mathbf{M}$ is negative semi-definite. This means that $\mathbf{M}$ has only negative or zero eigenvalues or, equivalently, the inner product $\langle \mathbf{x}, \mathbf{M} \cdot \mathbf{x} \rangle \leq 0$ for all $\mathbf{x}$. This means that also $\mathbf{P} \cdot \mathbf{M} \cdot \mathbf{P}$ is negative semi-definite, because:

$$\langle \mathbf{x}, \mathbf{P} \cdot \mathbf{M} \cdot \mathbf{P} \cdot \mathbf{x} \rangle = \langle \mathbf{P} \cdot \mathbf{x}, \mathbf{M} \cdot (\mathbf{P} \cdot \mathbf{x}) \rangle = \langle \mathbf{y}, \mathbf{M} \cdot \mathbf{y} \rangle \leq 0 \tag{3.27}$$

In conclusion, $\mathbf{J}_0$ has negative and zero eigenvalues only.

The remaining task is to identify the number of negative eigenvalues, or otherwise stated, the rank of the matrix $\mathbf{J}_0$. The statement which we shall prove is that $\mathrm{rank}(\mathbf{J_0}) = \mathrm{rank}(\mathbf{P}) = N - m$.

*Since both the mapping $\sigma \to \mathbf{J}_\sigma$ as $\mathbf{J}_\sigma \to \det(\mathbf{J}_\sigma - \lambda\mathbf{I})$ are C$^\infty$ mappings (from $\mathbb{R} \to \mathbb{R}^{N \times N}$ and $\mathbb{R}^{N \times N} \to$ P(λ) respectively, where P(λ) is the space of polynomials of order N), it is allowed to take the limits $\sigma \to 0$ and $\sigma \to -\infty$, even though the latter does not occur in practice.

Proof: Note that the image $\mathrm{Im}(\mathbf{P})$ of $\mathbf{P}$ is spanned by the first m unit vectors of $\mathbb{R}^N$. Its kernel $\mathrm{Ker}(\mathbf{P})$ is spanned by the remaining $N-m$ unit vectors. Since the kernel of $\mathbf{M}$ is spanned by the vector $\mathbf{1}$, the following identities hold:

$$\mathrm{Ker}(\mathbf{P}) \cap \mathrm{Ker}(\mathbf{M}) = \mathbf{0} \tag{3.28a}$$

$$\mathrm{Im}(\mathbf{P}) \cap \mathrm{Ker}(\mathbf{M}) = \mathbf{0} \tag{3.28b}$$

Now, for all $\mathbf{x} \in \mathrm{Ker}(\mathbf{P})$ it holds that $\mathbf{J}_0 \cdot \mathbf{x} = \mathbf{M} \cdot (\mathbf{P} \cdot \mathbf{x}) = \mathbf{0}$, so $\mathrm{Ker}(\mathbf{P}) \subset \mathrm{Ker}(\mathbf{J}_0)$. On the other hand, for all $\mathbf{y} \notin \mathrm{Ker}(\mathbf{P})$ one has $\mathbf{P} \cdot \mathbf{y} \equiv \mathbf{z} \neq 0$, with $\mathbf{z} \in \mathrm{Im}(\mathbf{P})$, and therefore $\mathbf{J}_0 \cdot \mathbf{y} = \mathbf{M} \cdot \mathbf{z} \neq 0$ because of Eq. (3.28b). This means that $\mathbf{y} \notin \mathrm{Ker}(\mathbf{J}_0)$, and thus $\mathrm{Ker}(\mathbf{P}) \supset \mathrm{Ker}(\mathbf{J}_0)$. Together these two results prove that $\mathrm{Ker}(\mathbf{P}) = \mathrm{Ker}(\mathbf{J}_0)$, so obviously the rank of the two matrices must be equal. Since $\mathrm{rank}(\mathbf{P}) = N - m$, this is also the rank of $\mathbf{J}_0$, which completes the proof.

In short, we have shown that in the limit $\sigma \to 0$, the Jacobi-matrix $\mathbf{J}$ has $N-m$ negative eigenvalues.

3.6.4 Number of positive eigenvalues for $\sigma \to -\infty$

We now turn to the limit $\sigma \to -\infty$. In this limit we rewrite $\mathbf{J}$ as follows: $\mathbf{J} = F'(n_-)\sigma\mathbf{M} \cdot \bar{\mathbf{D}}$. Here $\bar{\mathbf{D}} = \mathrm{diag}(\sigma^{-1}, \ldots, \sigma^{-1}, 1, \ldots, 1)$, which in the limit $\sigma \to -\infty$ becomes:

$$\lim_{\sigma \to -\infty} \bar{\mathbf{D}} = \mathrm{diag}(0, \ldots, 0, 1, \ldots, 1) \equiv \mathbf{Q} \tag{3.29}$$

Again, $\mathbf{Q}$ is a projection matrix, which now projects $\mathbb{R}^N$ to the subspace spanned by the last m unit vectors, so $\mathbf{Q}$ is complementary to $\mathbf{P}$. Following the same line of reasoning, but keeping in mind that now the constant factor in front of $\mathbf{J}_{-\infty}$ is negative, we find that in the limit $\sigma \to -\infty$, the matrix $\mathbf{J}$ has m *positive* eigenvalues.

3.6.5 Number of positive eigenvalues of J for general σ

We are now ready to draw the conclusion. Just below $\sigma = 0$ the matrix $\mathbf{J}$ must, by continuity, have at least $N-m$ negative eigenvalues. If we now move from 0 towards $-\infty$, beyond a certain point there must be at least m positive eigenvalues (or equivalently, at most $N-m-1$ negative eigenvalues). We already know [cf. Eq. (3.25)] that along the way exactly one eigenvalue changes sign, at $\sigma = -m/(N-m)$. Taken together, this means that $\mathbf{J}$ has m positive and $N-m-1$ negative eigenvalues for $\sigma < -m/(N-m)$, and $m-1$ positive and $N-m$ negative eigenvalues for $\sigma > -m/(N-m)$.

This completes the determination of the number of positive eigenvalues for the various branches in the bifurcation diagram.

References

[1] I. Goldhirsch and G. Zanetti, *Clustering instability in dissipative gases*, Phys. Rev. Lett. **70**, 1619 (1993).

[2] S. McNamara and W.R. Young, *Inelastic collapse in 2 dimensions*, Phys. Rev. E **50**, R28 (1994).

[3] Y. Du, H. Li, and L.P. Kadanoff, *Breakdown of hydrodynamics in a one-dimensional system of inelastic particles*, Phys. Rev. Lett. **74**, 1268 (1995).

[4] H.M. Jaeger, S.R. Nagel, and R.P. Behringer, *Granular solids, liquids, and gases*, Rev. Mod. Phys. **68**, 1259 (1996).

[5] A. Kudrolli, M. Wolpert, and J.P. Gollub, *Cluster formation due to collisions in granular material*, Phys. Rev. Lett. **78**, 1383 (1997).

[6] L.P. Kadanoff, *Built upon sand: Theoretical ideas inspired by granular flows*, Rev. Mod. Phys. **71**, 435 (1999).

[7] J. Eggers, *Sand as Maxwell's demon*, Phys. Rev. Lett. **83**, 5322 (1999).

[8] K. van der Weele, D. van der Meer, M. Versluis, and D. Lohse, *Hysteretic clustering in a granular gas*, Europhys. Lett. **53**, 328 (2001).

[9] S. McNamara and S. Luding, *Energy flows in vibrated granular media*, Phys. Rev. E **58**, 813 (1998).

[10] R. Guardiola and J. Ros, *On the numerical integration of the Schrödinger equation: Numerical tests*, J. Comp. Phys. **45**, 374 (1982).

Chapter 4

Sudden Collapse of a Granular Cluster [‡]

Single clusters in a vibro-fluidized granular gas in N connected compartments become unstable at strong shaking. They are experimentally shown to collapse very abruptly. The observed cluster lifetime (as a function of the driving intensity) is analytically calculated within a flux model, making use of the self-similarity of the process. After collapse, the cluster diffuses out into the uniform distribution in a self-similar way, with an anomalous diffusion exponent $1/3$.

4.1 Introduction

One of the key features of a granular gas, making it fundamentally different from ordinary molecular gases, is its tendency to spontaneously separate into dense and dilute regions [1–6]. This clustering originates from the dissipative nature of the particle collisions. It is an unwanted effect in many applications where granular material is brought into motion. Therefore we study (within a simple geometry) how *declustering* occurs. We find that the breakdown of a cluster can be very abrupt, making declustering very different from clustering in reverse time order.

The experimental system (see Fig. 4.1) consists of a row of N equal compartments, separated by walls of height $h = 25.0$ mm and filled with a few hundred steel beads of diameter 3.0 mm. We start out with all the particles in the middle compartment and bring them into a gaseous state by shaking the system vertically.

[‡]Published as: Devaraj van der Meer, Ko van der Weele, and Detlef Lohse, *Sudden Collapse of a Granular Cluster*, Phys. Rev. Lett. **88**, 174302, pp. 1-4 (2002).

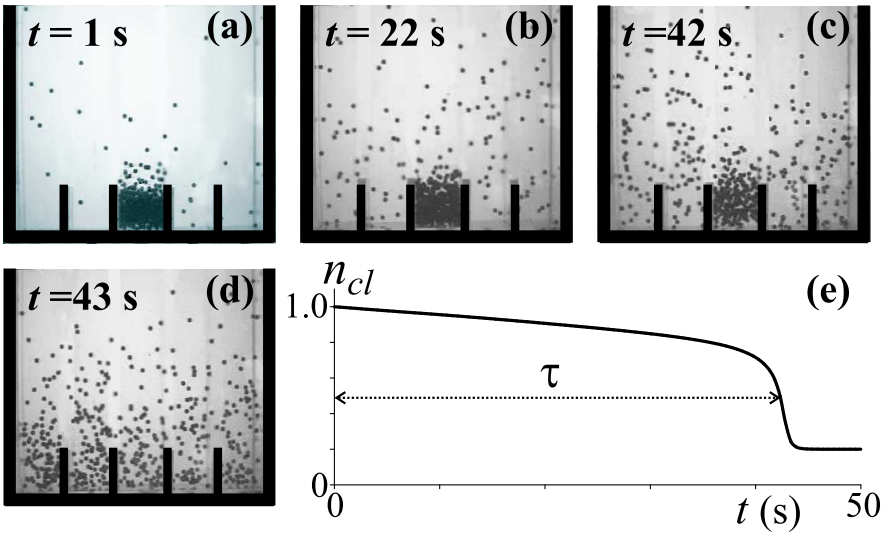

Figure 4.1: Four images from a 5-box experiment, at driving parameter $\widetilde{B} = 8.2$. The cluster is clearly present until $t = 42$ s, then suddenly collapses, leaving no trace one second later. Plot (e) shows the time evolution of the cluster fraction $n_{cl}(t)$, evaluated from the flux model.

For weak shaking the cluster is stable: after some initial spilling, a dynamical equilibrium is established between the outflux of slow particles from the cluster and the influx of fast particles from outside [7–9]. For sufficiently strong shaking, however, the cluster breaks down.

Two different regimes are observed: (i) At very strong shaking the breakdown occurs immediately, and the cluster spreads out over the boxes with its profile widening as $t^{1/3}$ (instead of the standard $t^{1/2}$ diffusion law). (ii) At less violent shaking, the cluster seems to remain stable for a long time, showing only a small leakage to its neighbors. But *suddenly* it collapses and subsequently diffuses over all boxes. The sudden death of the cluster is depicted in Fig. 4.1.

One thing this figure shows is that the breakdown of a cluster is strikingly different from the reverse process of cluster formation, which is known to take place gradually and (for all $N \geq 3$) via transient states showing clusters in several boxes [8, 9]. This lack of time-reversibility is yet another consequence of the dissipation in the system.

The abruptness of the collapse allows us to define a cluster lifetime τ (via $\ddot{n}_{cl}(\tau) = 0$, see Fig. 4.1e). In Fig. 4.2 the measured lifetimes are plotted as a function of the inverse shaking strength $\widetilde{B}$ [Eq. (4.2)] for various values of N. The

data lie on a universal envelope curve, until at some critical value $\widetilde{B}_{c,N}$ (which grows with N) they diverge.

4.2 Collapse of a cluster within the flux model

All the above experimental observations can be accounted for *quantitatively* by means of the flux model of refs. [7–9]. At the heart of this model is a flux function $F(n_k)$, describing the outflow from the kth box to each of its neighbors. It is a non-monotonic function of n_k (the particle fraction in the box): $F(n_k)$ first increases with n_k, but beyond a certain value of n_k it decreases again, as the increasingly frequent *inelastic* collisions slow the particles down, so that they cannot make it over the wall to the neighboring compartments anymore. The precise form of $F(n_k)$ is not very critical, as long as it is a one-humped function. We will use Eggers' flux function [7]

$$F(n_k) = C\sqrt{\widetilde{B}}n_k^2\, e^{-\widetilde{B}n_k^2}, \tag{4.1}$$

with

$$\widetilde{B} \propto \frac{ghr^4(1-e)^2P^2}{S^2(af)^2}. \tag{4.2}$$

The driving parameter $\widetilde{B}$ depends on the total number of particles P and their properties (radius r, restitution coefficient e of the particle collisions), on the geometry of the system (height h of the walls, ground area S of each box), and on the frequency f and amplitude a of the shaking. The factor C only determines the absolute rate of the flux, and can be incorporated in the time scale.

The equation of motion for the fraction in box k is*

$$\frac{dn_k}{dt} = F(n_{k-1}) - 2F(n_k) + F(n_{k+1}), \tag{4.3}$$

where $k = 1, 2, .., N$. Here we assume a nearest neighbor interaction, and a cyclic arrangement of the boxes ($k = N + 1$ equals $k = 1$). We further impose particle conservation, $\sum_k n_k = 1$.

The numerical results shown in Fig. 4.1e and Fig. 4.2 have been obtained using the above flux model, starting out with all particles in one box (labeled cl). They

*Statistical fluctuations, which would add a noise term to Eq. (4.3), are left out of this (mean field) description.

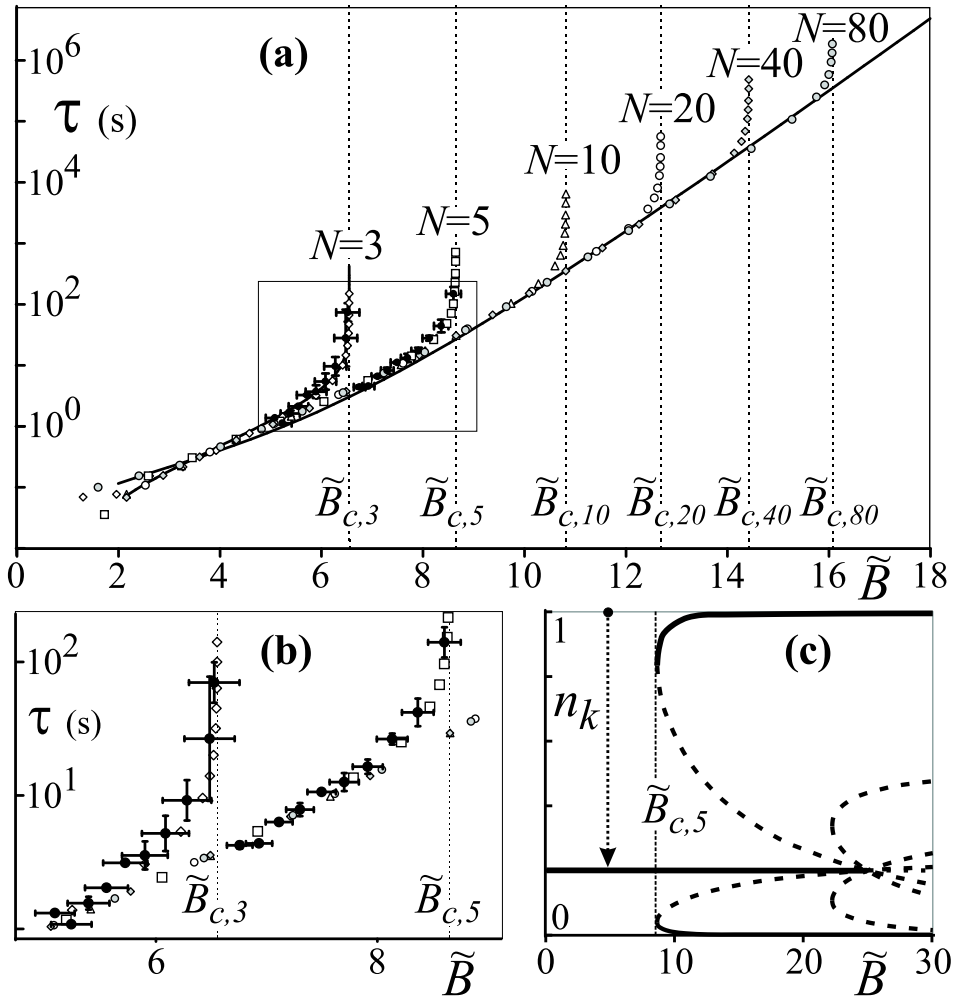

Figure 4.2: (a) Lifetime τ vs driving parameter $\widetilde{B}$, determined from experiments with $N = 3, 5$ boxes (dots with error bars), and from numerical evaluation of the flux model with $N = 3, 5, 10, 20, 40, 80$ boxes (empty symbols). The solid curves are analytical solutions for $N = 3$ and for the envelope curve, which goes roughly as $\exp((3/2)\widetilde{B})$ [cf. Eq. (4.13)]. (b) Enlargement of (a), showing the experimental results for $N = 3$ and $N = 5$ in more detail. Every point is based on 15 repetitions of the experiment; the vertical error bars denote the maximal deviation from the average τ measured, the horizontal ones represent the accuracy in $\widetilde{B}$. (c) Bifurcation diagram for $N = 5$, showing the critical value $\widetilde{B}_{c,5}$. Declustering occurs to the left of this value.

quantitatively agree with the experimental observations. The decaying cluster goes through *three* different stages:

The starting stage is a very short one, in which both n_{cl} and $F(n_{cl})$ display a jump compared to n_i and $F(n_i)$ in the surrounding boxes, $i = 1, 2, ..$ (we have to consider one side only because of the symmetry in the system).

In the second stage, the flux has become continuous but the particle fraction remains discontinuous. However, its low-density counterpart n_0 (defined by $F(n_0) = F(n_{cl})$) *does* continuously connect to n_1. We will use this fact later in the analysis of the envelope curve. The flux gradually grows, and eventually $F(n_{cl})$ reaches its maximum value. This is accompanied by rapid density changes and the sudden death of the cluster at the lifetime τ.

In the third and last stage, both n_{cl} and $F(n_{cl})$ fit continuously to the other boxes (see Fig. 4.3a). The remains of the cluster diffuse over the whole system until the uniform distribution is reached.

In what follows we will analytically solve the flux model. First we focus on the third stage. We rewrite the problem into its continuum version, by setting $n(x,t) \equiv n_k(t)$ ($x = kw$ by definition, where the box width w will be incorporated in the x-scale). Eq. (4.3) then becomes:

$$\begin{aligned} \partial_t n &= \partial_{xx} F\big(n(x,t)\big) \\ &= C\sqrt{\widetilde{B}}\partial_{xx}\left(n(x,t)^2 e^{-\widetilde{B}n(x,t)^2}\right), \end{aligned} \tag{4.4}$$

and the conservation condition takes the form $\int_{-\infty}^{\infty} n(x,t)dx = 1$.

For very strong shaking (regime (i), where τ is vanishingly small) the diffusive stage sets in almost immediately. Here $\widetilde{B} \to 0$, and Eq. (4.4) reduces to

$$\partial_t n = C\sqrt{\widetilde{B}}\partial_{xx}(n^2) = 2C\sqrt{\widetilde{B}}((\partial_x n)^2 + n\partial_{xx} n), \tag{4.5}$$

which is known as the porous media equation [10–12]. The decay of the cluster in this limit is depicted in Fig. 4.3a. It is self-similar: all curves in Fig. 4.3a fall onto a single curve if we properly rescale the axes (Fig. 4.3b). The original partial differential equation (PDE) can thus be brought back to an ordinary differential equation (ODE) in terms of the self-similarity variable $\eta = x/(C\widetilde{B}^{1/2}t)^{1/3}$. With $n(x,t) = H(\eta)/(C\widetilde{B}^{1/2}t)^{1/3}$, Eq. (4.5) now takes the form:

$$\partial_{\eta\eta}(H^2) + \frac{1}{3}\partial_\eta(\eta H) = 0. \tag{4.6}$$

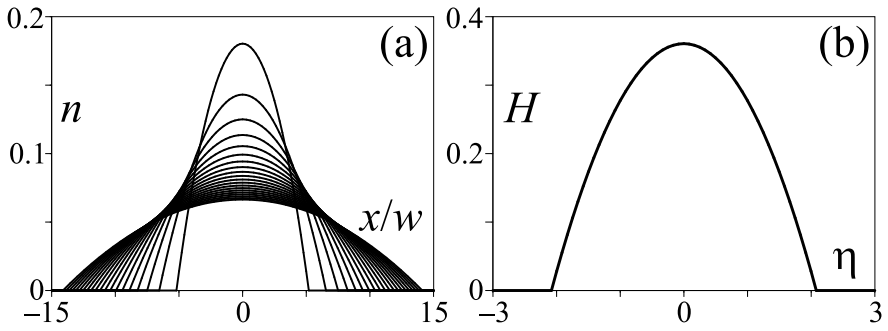

Figure 4.3: (a) The diffusing profile at successive times t (in the limit $\widetilde{B} = 0$). (b) The function $H(\eta)$ onto which all the curves in plot (a) collapse by a proper rescaling of the axes ($H \propto nt^{1/3}$ and $\eta \propto xt^{-1/3}$).

Its symmetric solution is $H(\eta) = H_0 - (1/12)\eta^2$ (with the constant $H_0 = (3^{1/3})/4 \approx 0.361$ determined by $\int_{-\infty}^{\infty} H(\eta)d\eta = 1$). This inverted parabola, depicted in Fig. 4.3b, represents in one curve *all* the stages of Fig. 4.3a. The scaling of the axes shows that the height of the cluster decreases as $t^{-1/3}$, and its width grows as $t^{1/3}$. This anomalous diffusion (with exponent $1/3$) is also found in porous media [10–12]. The slowed down diffusion of the front originates from the quadratic n-dependence in $\partial_{xx}n^2$ [Eq. (4.5)]. In the context of our granular model this reflects that particles only diffuse to neighboring boxes through 2-particle collisions: In the strong shaking limit the absence of particles slows down further diffusion, the presence enhances it.

For non-zero $\widetilde{B}$ (regime (ii), where the diffusive stage has to wait until after the sudden death) we have an additional dimensionless variable $\chi = \widetilde{B}/C(t-\tau)$. Its influence diminishes with time and the solutions converge to the inverted parabola of the case $\widetilde{B} \to 0$.

Next we turn to the second, semi-continuous stage. For moderate shaking, $\widetilde{B} \approx \widetilde{B}_{c,N}$, this stage can take quite a long time. At the critical point $\widetilde{B}_{c,N}$ the lifetime τ even diverges to infinity and the cluster becomes stable. Starting out from the initial ..,0,0,1,0,0,.. distribution, the system first *very slowly* approaches a distribution in which n_{cl} is close to the cluster density at the saddle-node bifurcation (see Fig. 4.2c) and all other boxes contain equal fractions $n_k = (1-n_{cl})/(N-1)$. Only when it has passed this phantom equilibrium (i.e., when n_{cl} is below the level of the saddle-node bifurcation), the system quickens its pace and the sudden collapse occurs.

This means that τ is the time it takes to pass the phantom equilibrium. It can be calculated either numerically or analytically [by integrating the Taylor expansion of Eq. (4.3)][†], with the result $\tau \propto (\widetilde{B}_{c,N} - \widetilde{B})^{-1/2}$. So τ diverges as the inverse square root of the distance to the critical point, which is the common (mean field) power-law behavior near a second order phase transition as we have here for τ [13].

4.3 Analytical approximation of the lifetime of a cluster

Finally, we calculate the lifetime away from the critical point, i.e., for $\widetilde{B}$ considerably smaller than $\widetilde{B}_{c,N}$. This will give us an analytical expression for the envelope curve in Fig. 4.2a. For these $\widetilde{B}$ values, the collapse occurs before the particles leaking out of the cluster have had time to fill the outermost boxes to any significant level. Therefore, the behavior does not depend on the value of N: The system does not feel its finite size during the cluster's lifetime, so the number of boxes can be taken to be infinite.

The time-evolution of the cluster is described by Eq. (4.3), with $F(n_{-1}) = F(n_1)$:

$$\frac{dn_{cl}}{dt} = -2F(n_{cl}) + 2F(n_1) = -2F(n_0) + 2F(n_1). \tag{4.7}$$

This equation contains n_1, which is governed by a similar equation of motion [Eq. (4.3)] containing n_2, etc. So we have to deal with an infinite number of coupled nonlinear ODE's [‡]. This is a problem that cannot be solved directly, so we attack it in five steps.

Step 1: We first rewrite the problem into its continuum version, and replace the cluster density n_{cl} by its low-density counterpart $n(0,t) \equiv n_0(t) \approx n_{cl}\exp(-\widetilde{B}n_{cl}^2/2)$. Thus, without influencing the fluxes (since $F(n_0) = F(n_{cl})$) we make $n(x,t)$ continuous in $x = 0$. The density $n(x,t)$ obeys Eq. (4.4), plus a conservation condition saying that the increase of material into the rest of the

[†]Details of this procedure can be found in the next chapter.

[‡]The case $N = 3$ is contained in a single ODE, which can be solved exactly: $\tau = \int_{n_{thr}}^{1} dn/2\{F((1-n)/2) - F(n)\}$ (solid curve in Fig. 4.2), with n_{thr} determined from $\ddot{n}(\tau) = 0$. An analogous expression holds for general N *close* to the critical point, where all the surrounding boxes are filled to the same level $n_k = (1 - n_{cl})/(N-1)$.

system equals the influx from $x = 0$:

$$\partial_t \int_0^\infty n(x,t)dx = -(\partial_x \big(F\big(n(x,t)\big)\big)_{x=0}. \tag{4.8}$$

Step 2: The cluster-equation Eq. (4.7) now becomes:

$$\begin{aligned} \frac{dn_{cl}}{dt} &= 2\Big(\partial_x F\big(n(x,t)\big)\Big)_{x=0} \\ &= 2F'\big(n(0,t)\big)\big(\partial_x n(x,t)\big)_{x=0}. \end{aligned} \tag{4.9}$$

Since F' can be derived directly from Eq. (4.1), the problem reduces to determining $\partial_x n(x,t)$ at $x = 0$.

Step 3: In order to do so, we observe that changes in $n(0,t)$ happen on a much longer timescale than in the surrounding boxes[§], so the cluster acts as a constant reservoir spilling granular material. This approximation is illustrated in Fig. 4.4a: the profile in the system builds up while n_0 remains constant. In fact, this build-up takes place in a self-similar way (see Fig. 4.4b). So, as before, the problem for $n(x,t)$ can be formulated in terms of one variable $\xi = x/(n_0 C\widetilde{B}^{1/2}t)^{1/2}$. Setting $n(x,t) = n_0 G(\xi)$, Eq. (4.4) becomes an ODE for $G(\xi)$, and also the accompanying conservation condition [Eq. (4.8)] contains ξ only:

$$\begin{aligned} \frac{1}{2}\xi\partial_\xi G &= -\partial_{\xi\xi}(G^2 e^{-\beta G^2}), \\ (\partial_\xi G)_{\xi=0} &= -\frac{e^\beta}{4(1-\beta)}\int_0^\infty G(\xi)d\xi, \end{aligned} \tag{4.10}$$

where $\beta = \widetilde{B}n_0^2$.

Step 4: The slope $(\partial_x n(x,t))_{x=0}$ can now be approximated by the expression $n_0(t)(\partial_\xi G(\xi))_{\xi=0}(\partial_x \xi)_{x=0}$, where we have revived the (slow) time-dependence in

[§]A cluster change Δn_{cl} (flowing into the surrounding boxes) corresponds to a much smaller change Δn_0 in its low-density counterpart: $dn_{cl}/dn_0 = (1-\widetilde{B}n_{cl}^2)^{-1}e^{\widetilde{B}n_{cl}^2/2} \approx (1-\widetilde{B})^{-1}e^{\widetilde{B}/2}$ since $n_{cl} \approx 1$. So for most $\widetilde{B}$-values of interest (excluding the strong-shaking regime $\widetilde{B} \to 0$) $|\Delta n_{cl}| = \sum_{i\neq 0}\Delta n_i \gg \Delta n_0$.

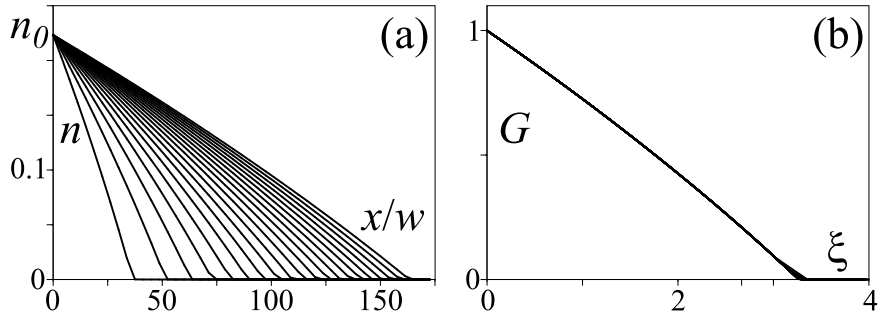

Figure 4.4: (a) The density profi le in the boxes surrounding the cluster, at 20 consecutive (equidistant) moments in time, within the constant n_0 approximation; $n_0 = 0.223$ and $\widetilde{B} = 3.00$. (b) The function $G = n/n_0$ onto which all curves in plot (a) collapse by a proper rescaling of the axes ($\xi \propto xt^{-1/2}$.)

$n_0(t)$. With $\partial_x \xi = (n_0(t) C \widetilde{B}^{1/2} t)^{-1/2}$, Eq. (4.9) becomes:

$$\frac{dn_{cl}}{dt} = 2\frac{\sqrt{n_0(t)}}{\sqrt{C\widetilde{B}^{1/2}t}} F'\big(n_0(t)\big)\big(\partial_\xi G(\xi)\big)_{\xi=0}. \tag{4.11}$$

All quantities on the right hand side are tractable. We re-express $n_0(t)$ in terms of $n_{cl}(t)$, derive F' from Eq. (4.1), and solve Eq. (4.10) to determine $\big(\partial_\xi G(\xi)\big)_{\xi=0}$. This last step still requires some work, because Eq. (4.10) does not allow an analytical solution and moreover contains β (and hence $n_0(t)$) explicitly. Since β is small, however, we may expand $G(\xi)$ and Eq. (4.10) in terms of β, and solve numerically. In leading order we find $\big(\partial_\xi G(\xi)\big)_{\xi=0} \equiv -K = -0.3138$. Inserting all this, Eq. (4.11) becomes:

$$\frac{dn_{cl}}{dt} = -4\frac{K n_{cl}^{3/2} e^{-(3/4)\widetilde{B}n_{cl}^2}}{\sqrt{C\widetilde{B}^{1/2}t}}\Big(1 - \widetilde{B}n_{cl}^2 e^{-\widetilde{B}n_{cl}^2}\Big). \tag{4.12}$$

This is an ODE for n_{cl} in closed form, which replaces the original problem [Eq. (4.7)] consisting of an infinite number of coupled ODE's.

Step 5: Finally, we integrate Eq. (4.12) over the cluster density (dropping the suffix cl) and find an analytical expression for the lifetime τ away from the critical points:

$$\tau = \left[\int_{n_{thr}}^{1} \frac{\sqrt{C\widetilde{B}^{1/2}} n^{-3/2} e^{(3/4)\widetilde{B}n^2} dn}{8K\big(1 - \widetilde{B}n^2 e^{-\widetilde{B}n^2}\big)}\right]^2. \tag{4.13}$$

Here n_{thr} is the value of n at which the sudden death occurs. For the evaluation of the solid curve in Fig. 4.2a we used $n_{thr} = 0.5$, but this value is not too critical (cf. Fig. 4.1e). The only free parameter is the constant C: if this is adjusted properly, the analytical τ curve agrees with the measured data over the whole range of $\widetilde{B}$-values.

The above expression shows that τ roughly increases as $\exp(\widetilde{B}^{3/2})$. Recalling that $\widetilde{B}$ is the inverse shaking strength, this underlines the experimental observation that even a small reduction in the shaking strength causes a tremendous increase of the cluster lifetime.

In conclusion, in the studied compartmentalized system clusters break down very abruptly, in contrast to their slow formation. As clustering itself, the lack of time reversibility originates from the dissipative nature of the particle collisions: The breakdown of the unstable cluster is delayed because most of the energy input is dissipated through collisions in the cluster. The dynamics is *quantitatively* described by a remarkably simple flux model, which can be analytically solved.

References

[1] I. Goldhirsch and G. Zanetti, *Clustering instability in dissipative gases*, Phys. Rev. Lett. **70**, 1619 (1993).

[2] S. McNamara and W.R. Young, *Inelastic collapse in 2 dimensions*, Phys. Rev. E **50**, R28 (1994).

[3] Y. Du, H. Li, and L.P. Kadanoff, *Breakdown of hydrodynamics in a one-dimensional system of inelastic particles*, Phys. Rev. Lett. **74**, 1268 (1995).

[4] H.M. Jaeger, S.R. Nagel, and R.P. Behringer, *Granular solids, liquids, and gases*, Rev. Mod. Phys. **68**, 1259 (1996).

[5] A. Kudrolli, M. Wolpert, and J.P. Gollub, *Cluster formation due to collisions in granular material*, Phys. Rev. Lett. **78**, 1383 (1997).

[6] L.P. Kadanoff, *Built upon sand: Theoretical ideas inspired by granular flows*, Rev. Mod. Phys. **71**, 435 (1999).

[7] J. Eggers, *Sand as Maxwell's demon*, Phys. Rev. Lett. **83**, 5322 (1999).

[8] K. van der Weele, D. van der Meer, M. Versluis, and D. Lohse, *Hysteretic clustering in a granular gas*, Europhys. Lett. **53**, 328 (2001).

[9] D. van der Meer, K. van der Weele, and D. Lohse, *Bifurcation diagrams of compartmentalized granular gases*, Phys. Rev. E **63**, 061304 (2001).

[10] G. Barenblatt, *Scaling, self-similarity, and intermediate asymptotics* (Cambridge Univ. Press, New York, 1996).

[11] G. Barenblatt, M. Bertsch, A. Chertock, and V. Prostokishin, *Self-similar intermediate asymptotics for a degenerate parabolic filtration-absorption equation*, P. Natl. Acad. Sci. USA **97**, 9844 (2000).

[12] T. Witelski and A. Bernoff, *Self-similar asymptotics for linear and nonlinear diffusion equations*, Stud.Appl.Math. **100**, 153 (1998).

[13] L. Landau and E. Lifshitz, *Statistical physics, Part 1* (Pergamon, Oxford, 1980), 3rd ed.

Chapter 5

Critical behavior of a granular cluster [‡]

Single clusters in a compartmentalized granular gas become unstable at sufficiently strong shaking. Under typical experimental conditions, the cluster remains relatively unaffected for a considerable time τ (the so-called lifetime of the cluster) and then abruptly collapses. Very close to the instability threshold, τ diverges with a critical exponent $-1/2$. This is explained in terms of a flux model using a mean field potential formulation.

5.1 Introduction

As discussed in the previous chapter, the collapse of a granular cluster in an experiment within a compartmentalized system occurs quite abruptly, after a long period of time in which there were few signs of the cluster not being stable. This same "sudden death" phenomenon is seen in molecular dynamics simulations of the experiment (see Fig. 5.1, fluctuating lines) and in our analytical flux model (Fig. 5.1, solid lines). After 42 seconds the cluster is still clearly visible, and then abruptly collapses within one second [1].

The suddenness of the collapse makes it possible to define the cluster lifetime τ (see Ch. 4, Fig. 4.2), where we show lifetime data as function of the driving parameter $\widetilde{B}$ [see Ch. 4, Eq. (4.2)], for various numbers of compartments N, spanning no less than eight orders of magnitude. For each value of N there are two

[‡] Adapted from: Devaraj van der Meer and Ko van der Weele, *Breakdown of a Near-Stable Granular Cluster*, Prog. Theor. Phys. Suppl. **150**, pp. 297-312 (2003)

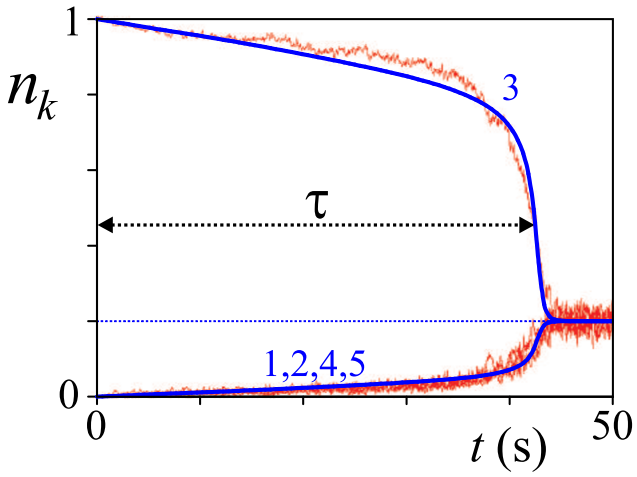

Figure 5.1: Evolution of the fractions n_k, $k = 1, .., 5$, for a five-box system at $\widetilde{B} = 8.2$ as calculated from the flux model (solid line) and from a molecular dynamics simulation (fluctuating lines) with input parameters corresponding to the actual experiment in Fig. 4.1. The cluster collapse occurs at $\tau = 42$ seconds.

distinct regimes to distinguish:

(i) Close to the critical value $\widetilde{B}_{c,N}$ (different for every value of N) the lifetime τ diverges. This stands to reason, because the cluster becomes a stable equilibrium at $\widetilde{B}_{c,N}$, with an infinite lifetime.

(ii) Further away from $\widetilde{B}_{c,N}$ the lifetimes lie on a universal curve, which increases roughly as $\exp[(3/2)\widetilde{B}]$. This reflects the experimental fact that a small reduction of $\widetilde{B}$ (i.e., a small increase of the shaking strength) causes an exponential reduction of the cluster lifetime.

The second regime with its universal curve has been treated in detail in the previous chapter. In the present chapter we explore regime (i), within the context of the flux model. In Section 5.2 we describe the cluster dynamics and the divergency of τ close to the critical point $\widetilde{B}_{c,N}$, which turns out to go as $\tau \propto (\widetilde{B}_{c,N} - \widetilde{B})^{-1/2}$. In Section 5.3 the problem is re-formulated in terms of a potential theory and placed in the wider context of phase transitions. Finally, in Section 5.4 we give a few concluding remarks.

5.2 Cluster dynamics close to the critical point

5.2.1 Phenomenology

We start out with all the particles in the middle compartment, which we label cl (for cluster). Because of the symmetry of the set-up, the particles spill out symmetrically towards both sides into the surrounding compartments.

In regime (ii), for $\widetilde{B}$ values some distance away from the critical point $\widetilde{B}_{c,N}$, all lifetime data lie on one and the same curve, regardless of the number of compartments N in the system. This is because the cluster collapses *before* the particles leaking out of the cluster fill the outermost compartments to any significant level. In this regime the N-compartment system is essentially equivalent to a system with an infinite number of compartments. [1]

In contrast, in regime (i), close to $\widetilde{B}_{c,N}$, the lifetime τ is so long that the particles spilling from the cluster have time to reach even the outermost boxes long before the collapse. All this time, the system seems to be heading for a dynamical equilibrium with one well-filled compartment n_{cl} surrounded by $N-1$ nearly empty compartments. In our analysis we will indeed assume that (just as in the true equilibrium situation to the right of $\widetilde{B}_{c,N}$) all nearly empty compartments have an equal fraction $n_k = (1-n_{cl})/(N-1)$. This means that our description is in fact a mean-field theory, in the same spirit as the Bragg-Williams theory for an Ising ferromagnet, where the actual magnetization of each lattice-site is replaced by its mean value [2, 3].

There is also a close parallel with the calculation of the length of the laminar phases in type-I intermittency [4, 5]. The main difference is that in intermittent systems the trajectory is re-injected again and again into the critical region of slow dynamics (where the so-called "ghost" of the equilibrium is felt), whereas in our case this region is passed only once.

Only when the critical region has been passed, the system shoots toward the uniform distribution. The lifetime τ, from the start of the experiment until this sudden collapse, can be calculated from the flux model:

$$\tau = \int_{n_{cl}=1}^{n_{thr}} dt, \tag{5.1}$$

where dt is understood to be expressed in terms of n_{cl}. A good choice for the threshold n_{thr} is where $n_{cl}(t)$ has an inflection point (Fig. 4.1), but its value is not too critical for the determination of τ. In practice $n_{thr} = 0.5$ gives good results for all $N \geq 3$.

At the critical point $\widetilde{B}_{c,N}$ itself, the center compartment would contain a frac-

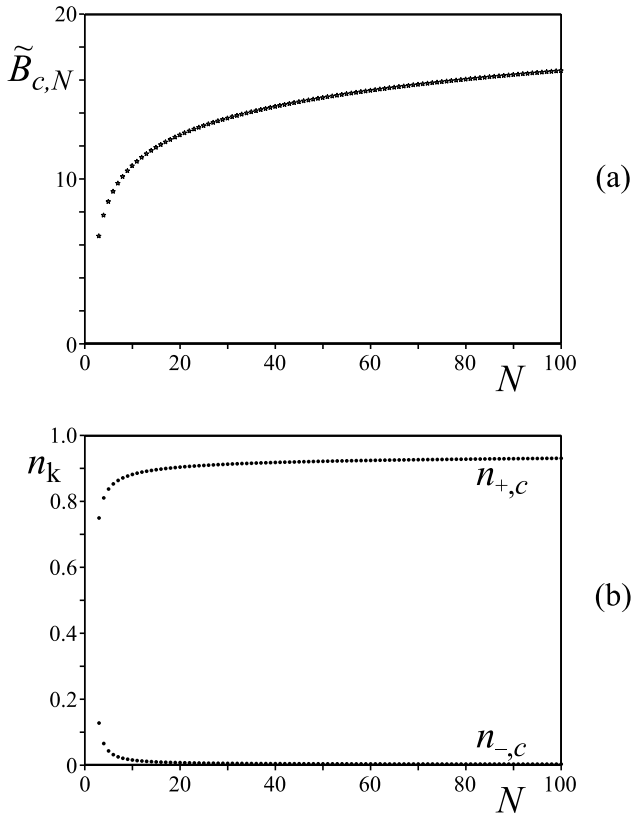

Figure 5.2: (a) The critical value $\widetilde{B}_{c,N}$ (the lowest $\widetilde{B}$-value for which a cluster can persist, cf. Figs. 4.1 and 4.2) as a function of the number of compartments N, for $N = 3, 4, 5, .., 100$. (b) The corresponding values of the cluster fraction $n_{+,c}$ and the fraction $n_{-,c}$ of the surrounding, nearly empty compartments.

tion $n_{cl} = n_{+,c}$, while the surrounding compartments would all have $n_k = n_{-,c}$. Figure 5.2 shows how the three principal quantities $\widetilde{B}_{c,N}$, $n_{+,c}$, and $n_{-,c}$ depend on the value of N. At the critical point the fluxes from the cluster and the dilute compartments balance each other [Ch. 3, Eq. (3.5)]:

$$F(n_{+,c}) = F(n_{-,c}), \tag{5.2}$$

which means that Eq. (4.3) reduces to $dn_{cl}/dt = 0$. So the dynamics come to a standstill and the lifetime of the cluster (which becomes stable at this point) goes to infinity; see Fig. 4.2. At the critical point there also exists an identity for the derivative of F, namely the bifurcation condition [Ch. 3, Eq. (3.8)]

$$\left(\frac{\partial F}{\partial n}\right)_{n_{+,c}} = -\frac{1}{(N-1)}\left(\frac{\partial F}{\partial n}\right)_{n_{-,c}}. \tag{5.3}$$

In Section 5.3, where we give an alternative formulation of the problem in terms of a potential function, we will connect the above two relations (5.2) and (5.3) to the standard conditions for a critical point in the theory of phase transitions.

5.2.2 The equation of motion: Taylor expansion

Close to the critical point, the equation of motion of the cluster can be expanded in the small quantities $\delta n = n_{cl} - n_{+,c}$ and $\delta\widetilde{B} = \widetilde{B}_{c,N} - \widetilde{B}$. Equation (4.3) becomes, with $n_k = n_{cl} = n_{+,c} + \delta n$ and $n_{k-1} = n_{k+1} = n_{-,c} - \delta n/(N-1)$:

$$\begin{aligned}\frac{dn_{cl}}{dt} &= \frac{d(\delta n)}{dt} \\ &= 2F(n_{-,c} - \frac{\delta n}{N-1}, \widetilde{B}_{c,N} - \delta\widetilde{B}) - 2F(n_{+,c} + \delta n, \widetilde{B}_{c,N} - \delta\widetilde{B}).\end{aligned} \tag{5.4}$$

We Taylor expand this up to quadratic order in δn and $\delta\widetilde{B}$:*

$$\begin{aligned}&\frac{d(\delta n)}{dt} = \\ &2\Big\{F_- + \left(\frac{\partial F}{\partial n}\right)_-\left(\frac{-\delta n}{N-1}\right) + \left(\frac{\partial F}{\partial \widetilde{B}}\right)_-(-\delta\widetilde{B}) \\ &\quad + \frac{1}{2}\left(\frac{\partial^2 F}{\partial n^2}\right)_-\left(\frac{-\delta n}{N-1}\right)^2 + \left(\frac{\partial^2 F}{\partial n \partial \widetilde{B}}\right)_-\left(\frac{-\delta n}{N-1}\right)(-\delta\widetilde{B}) \\ &\quad + \frac{1}{2}\left(\frac{\partial^2 F}{\partial \widetilde{B}^2}\right)_-(-\delta\widetilde{B})^2\Big\}\end{aligned}$$

*Here the subscript $-$ denotes that the quantity is evaluated at $n = n_{-,c}$, and $+$ denotes that it is evaluated at $n_{+,c}$. The associated $\widetilde{B}$-value is always $\widetilde{B}_{c,N}$.

$$
\begin{aligned}
&- 2\Big\{F_+ + \left(\frac{\partial F}{\partial n}\right)_+ \delta n + \left(\frac{\partial F}{\partial \widetilde{B}}\right)_+ (-\delta\widetilde{B}) \\
&\quad + \frac{1}{2}\left(\frac{\partial^2 F}{\partial n^2}\right)_+ (\delta n)^2 + \left(\frac{\partial^2 F}{\partial n \partial \widetilde{B}}\right)_+ \delta n(-\delta\widetilde{B}) \\
&\quad + \frac{1}{2}\left(\frac{\partial^2 F}{\partial \widetilde{B}^2}\right)_+ (-\delta\widetilde{B})^2\Big\}.
\end{aligned} \tag{5.5}
$$

The leading term $2(F_- - F_+)$ drops out because of the flux balance Eq. (5.2), and the terms linear in δn cancel each other because of Eq. (5.3), so the above equation can be rewritten as:

$$
\frac{d(\delta n)}{dt} = -L\delta\widetilde{B} - M(\delta n)^2 + X\delta n\delta\widetilde{B} - Z(\delta\widetilde{B})^2, \tag{5.6}
$$

where L, M, X, and Z are four positive coefficients, depending only on the number of boxes N:

$$
\begin{aligned}
L &= 2\Big\{\left(\frac{\partial F}{\partial \widetilde{B}}\right)_- - \left(\frac{\partial F}{\partial \widetilde{B}}\right)_+\Big\} \\
&= 2\sqrt{\widetilde{B}_{c,N}}\left(n_{+,c}^2 - n_{-,c}^2\right) n_{-,c}^2 e^{-\widetilde{B}_{c,N} n_{-,c}^2}, \\
M &= -\Big\{\frac{1}{(N-1)^2}\left(\frac{\partial^2 F}{\partial n^2}\right)_- - \left(\frac{\partial^2 F}{\partial n^2}\right)_+\Big\}, \\
X &= 2\Big\{\frac{1}{N-1}\left(\frac{\partial^2 F}{\partial n \partial \widetilde{B}}\right)_- + \left(\frac{\partial^2 F}{\partial n \partial \widetilde{B}}\right)_+\Big\}, \\
Z &= -\Big\{\left(\frac{\partial^2 F}{\partial \widetilde{B}^2}\right)_- - \left(\frac{\partial^2 F}{\partial \widetilde{B}^2}\right)_+\Big\}.
\end{aligned} \tag{5.7}
$$

As an example, we have worked out L in terms of $\widetilde{B}_{c,N}$, $n_{-,c}$, and $n_{+,c}$. This is done straight from Eq. (4.1), only leaving out the factor C because this has been incorporated in the time scale (which makes all quantities appearing in Eq. (5.7) dimensionless). The other three coefficients can be worked out similarly. Figure 5.3 shows how they vary with N.

Now it is convenient to rewrite Eq. (5.6) in the following way, in order to get rid of the cross-term $X\delta n\delta\widetilde{B}$:

$$
\frac{d(\delta n)}{dt} = -L\delta\widetilde{B} - M\left(\delta n - \frac{X}{2M}\delta\widetilde{B}\right)^2 + \left(\frac{X^2}{4M} - Z\right)(\delta\widetilde{B})^2. \tag{5.8}
$$

With $\delta\hat{n} \equiv \delta n - (X/2M)\delta\widetilde{B}$ and $W \equiv (X^2/4M) - Z$, and noting that $d(\delta\hat{n})/dt = d(\delta n)/dt$, the above equation takes the form:

$$
\frac{d(\delta\hat{n})}{dt} = -L\delta\widetilde{B} - M(\delta\hat{n})^2 + W(\delta\widetilde{B})^2. \tag{5.9}
$$

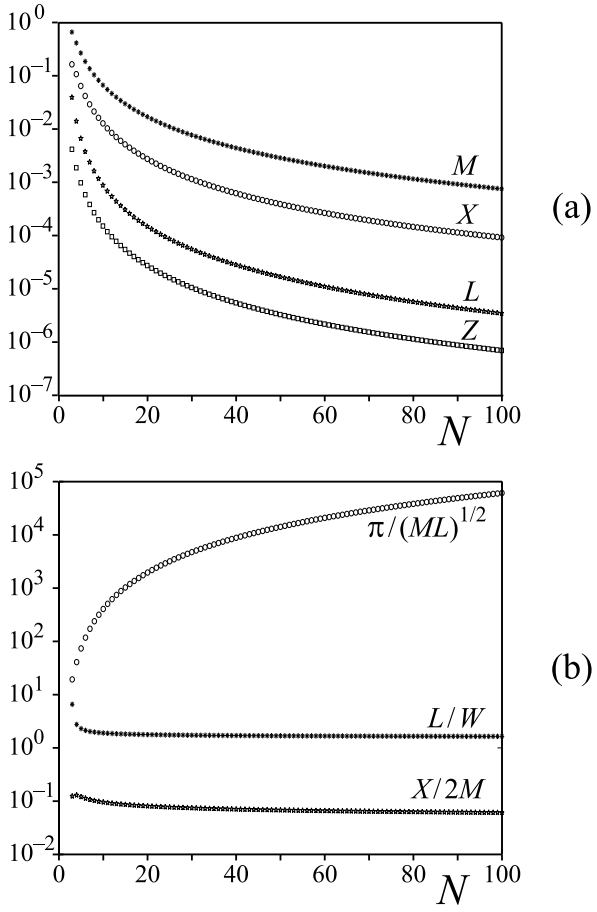

Figure 5.3: (a) The coefficients L, M, X, and Z appearing in the Taylor expansion Eq. (5.6) of the cluster's equation of motion close to the critical point. (b) The composite ratios $X/2M$, $L/W = L/[(X^2/4M) - Z]$, and $\pi/\sqrt{ML}$ that play a role in the further evaluation of the cluster lifetime τ. The smallness of $X/2M$ means that close to the critical point $\delta\hat{n} \approx \delta n$, so a change in $\delta\hat{n}$ [see Eqs. (5.9)-(5.11)] may be identified with practically the same change in δn. The ratio $L/W = L/[(X^2/4M) - Z] \sim 1$ indicates that the coefficients of the linear and quadratic terms in $\delta\widetilde{B}$ are of the same order of magnitude [see Eq. (5.8)] and determines the range of validity of the final simplification made in Eq.(5.12). The third ratio is the prefactor in the end result $\tau \propto (\delta\widetilde{B})^{-1/2}$. It shows a strong growth with increasing N, in agreement with the results from flux model and experiment (see Fig. 4.2a).

Incidentally, since the ratio $X/2M \lesssim 0.1$ for all N (see Fig. 5.3b), the difference between $\delta\hat{n}$ and δn vanishes near the critical point. From Eq. (5.9) we can extract dt:

$$dt = \frac{-d(\delta\hat{n})}{(L - W\delta\widetilde{B})\delta\widetilde{B} + M(\delta\hat{n})^2}, \tag{5.10}$$

which must be integrated to find the lifetime τ.

5.2.3 Evaluation of the cluster lifetime

Strictly speaking, the integration goes from the initial situation ($n_{cl} = 1$) until n_{thr} is reached [Eq. (5.1)], but since the system lingers a long time in the neighborhood of the critical point, the main contribution to τ comes from an interval between $\delta\hat{n} = \epsilon$ (when n_{cl} is just above the critical fraction) and $\delta\hat{n} = -\epsilon$ (when it is just below it). So:

$$\begin{aligned}\tau &\approx \int_{\epsilon}^{-\epsilon} \frac{-d(\delta\hat{n})}{(L - W\delta\widetilde{B})\delta\widetilde{B} + M(\delta\hat{n})^2} \\ &= \frac{2\arctan\left(\epsilon\sqrt{M/(L - W\delta\widetilde{B})\delta\widetilde{B}}\right)}{\sqrt{M(L - W\delta\widetilde{B})\delta\widetilde{B}}} \approx \frac{\pi}{\sqrt{M(L - W\delta\widetilde{B})\delta\widetilde{B}}}.\end{aligned} \tag{5.11}$$

The last approximation uses the fact that sufficiently close to the critical point, the argument $\epsilon\{M/(L - W\delta\widetilde{B})\delta\widetilde{B}\}^{1/2}$ becomes a large number. One final simplification is obtained by realizing that close to the critical point $\delta\widetilde{B} \ll L/W$ (with L/W of order 1, see Fig. 5.3b), or equivalently $(L - W\delta\widetilde{B}) \approx L$, yielding:

$$\tau(N, \delta\widetilde{B}) \approx \frac{\pi}{\sqrt{ML\delta\widetilde{B}}}. \tag{5.12}$$

Thus our mean-field theory predicts that, close to the critical point, τ is proportional to $(\delta\widetilde{B})^{-1/2}$. This is in good agreement with the lifetime data obtained from the flux model, as can be seen in the doubly logarithmic plot of Fig. 5.4: all data points for $\delta\widetilde{B}/\widetilde{B}_{c,N} \lesssim 0.05$ lie on a straight line with slope $-1/2$. These data correspond to the upward strokes of $\tau(\widetilde{B})$ in Fig. 4.2 near each critical value $\widetilde{B}_{c,N}$. For $\delta\widetilde{B}/\widetilde{B}_{c,N} > 0.05$ the lifetimes start to deviate from the straight line (they are considerably smaller) and we enter the regime of the universal envelope curve in Fig. 4.2.

Also the fact that the prefactor $\pi/\sqrt{ML}$ in Eq. (5.12) grows strongly with increasing number of compartments N, see Fig. 5.3b, is in agreement with the lifetime results in Fig. 4.2.

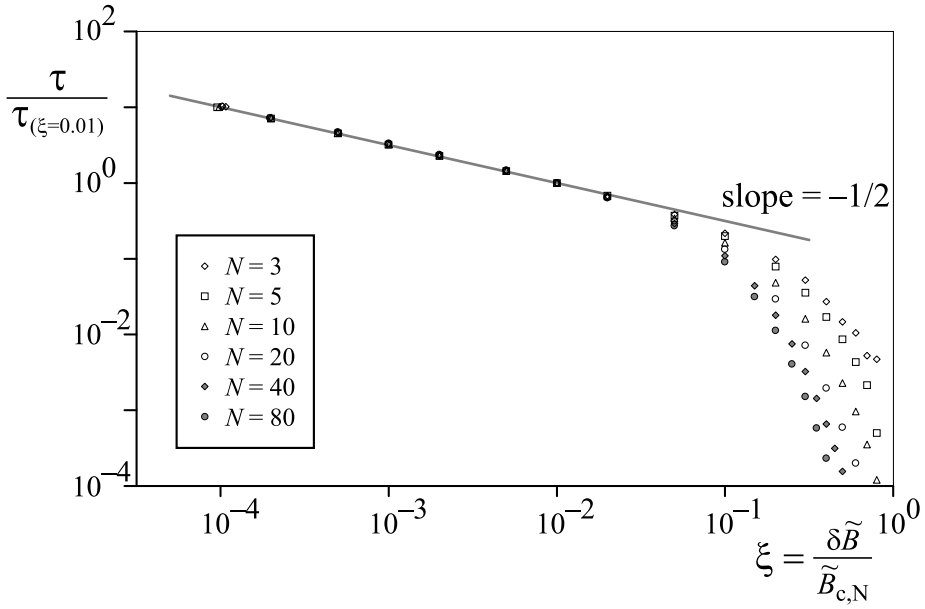

Figure 5.4: Doubly logarithmic plot of the lifetime τ as a function of the distance from the critical $\widetilde{B}$-value ($\delta\widetilde{B} \equiv \widetilde{B}_{c,N} - \widetilde{B}$) for the data series of Fig. 4.2. Both axes have been scaled in order to compare the data for different values of N. It is seen that for $\delta\widetilde{B} \to 0$, all data points converge to a straight line with slope $-1/2$, in agreement with the prediction of Eq. (5.12).

5.3 Potential formulation

The problem of the decaying cluster close to criticality can also be formulated in terms of a potential function. As before, we start out from the equation of motion of the system, Eq. (4.3), with $n_k = n_{cl}$ and $n_i = (1 - n_{cl})/(N - 1)$ for all $i \neq k$:

$$\frac{dn_{cl}}{dt} = 2F\left(\frac{1 - n_{cl}}{N - 1}\right) - 2F(n_{cl}), \tag{5.13}$$

but now we recognize that this can be written as the derivative, with respect to n_{cl}, of a potential $G(n_{cl}, \widetilde{B})$. That is, $dn_{cl}/dt = -\partial G(n_{cl}, \widetilde{B})/\partial n_{cl}$, or dropping the subscript cl and the $\widetilde{B}$-dependence for notational convenience:

$$\frac{dn}{dt} = -\frac{\partial G(n)}{\partial n}. \tag{5.14}$$

The fact that the dynamics of the N-box system close to the critical point can be described with a one-dimensional potential function crucially hinges on the fact

that we take the fraction of *all* the dilute boxes to be equal: i.e., the material that spills out of the slowly decaying cluster is supposed to be divided equally over the rest of the system. This is a typical mean-field assumption [†]. Indeed, as we will see, there is a close analogy with mean-field theories for phase transitions here [2, 3], with $G(n)$ playing the role of the *thermodynamic potential*.

To construct $G(n)$, we first introduce the function $P(n)$ such that:

$$\frac{\partial P}{\partial n} \equiv F(n). \tag{5.15}$$

If we further note that

$$\begin{aligned} \frac{\partial}{\partial n}\left(P\left(\frac{1-n}{N-1}\right)\right) &= \frac{\partial P}{\partial u}\frac{du}{dn}\bigg|_{u=\frac{1-n}{N-1}} = -\frac{1}{N-1}\frac{\partial P}{\partial u}\bigg|_{u=\frac{1-n}{N-1}} \\ &= -\frac{1}{N-1}F\left(\frac{1-n}{N-1}\right), \end{aligned} \tag{5.16}$$

the function $G(n)$, defined by Eq. (5.14), can be written down immediately:

$$G(n) = 2\left\{P(n) + (N-1)P\left(\frac{1-n}{N-1}\right)\right\} + K(\widetilde{B}), \tag{5.17}$$

where $K(\widetilde{B})$ is an arbitrary function of $\widetilde{B}$. The explicit form of the auxiliary function $P(n)$ is found by integration:

$$\begin{aligned} P(n) &= C\sqrt{\widetilde{B}}\int_0^n x^2 e^{-\widetilde{B}x^2}dx \\ &= -\frac{C}{4\widetilde{B}}\left\{2\sqrt{\widetilde{B}}ne^{-\widetilde{B}n^2} + \sqrt{\pi}\mathrm{erf}(\sqrt{\widetilde{B}}n)\right\}. \end{aligned} \tag{5.18}$$

The critical point conditions Eqs. (5.2) and (5.3) take a particularly elegant form in the potential formulation. The flux balance Eq. (5.2) becomes

$$\frac{\partial G}{\partial n} = 0 \tag{5.19}$$

and is equivalent to the thermodynamic *equation of state*. In the present context it provides the relation between n and $\widetilde{B}$ along the branches in the bifurcation diagram. The second equation Eq. (5.3) locates the critical points, or bifurcation

[†] Away from the critical point, the potential $G(n)$ does not accurately describe the dynamics of the system, since in that case there are many more equivalent degrees of freedom. This holds especially around the uniform distribution $n = 1/N$.

points, where these branches switch stability. This is where the derivative of the equation of state (with respect to the order parameter n) becomes zero:

$$\frac{\partial^2 G}{\partial n^2} = 0. \tag{5.20}$$

The two relations Eqs. (5.19) and (5.20) are by no means restricted to the present system. They are frequently encountered at critical points in general, e.g., in the liquid-gas transition, or in the transition from the isotropic to the smectic phase in liquid crystals [2].

The potential $G(n)$ is plotted in Fig. 5.5 for $N = 3$, at three values of $\widetilde{B}$ around the critical value $\widetilde{B}_{c,3} = 6.55$. The dynamics of the system is directed along the downward slopes of $G(n)$ towards the nearest minimum. For $\widetilde{B} = 6.65$, represented by the dotted line, this means that n evolves either towards the global minimum $n = 1/3$ (the uniform distribution) or to the local minimum at $n = 0.82$ (the clustered state). For the case that concerns us here, $\widetilde{B} < \widetilde{B}_{c,3}$ (solid line in Fig. 5.5), there is only one minimum: $n = 1/3$, and the evolution is always directed towards this point.

As we did with dn_{cl}/dt in section 5.2.2, we can expand $G(n)$ as a Taylor series around the critical point $(n_{+,c}, \widetilde{B}_{c,N})$. Up to second order in $\delta\widetilde{B}$ and third order in δn this leads to

$$\begin{aligned} G(\delta n, \delta\widetilde{B}) = &\left(\left(\frac{\partial G}{\partial n} \right)_c - \left(\frac{\partial^2 G}{\partial n \partial \widetilde{B}} \right)_c \delta\widetilde{B} + \frac{1}{2} \left(\frac{\partial^3 G}{\partial n \partial \widetilde{B}^2} \right)_c (\delta\widetilde{B})^2 \right) \delta n \\ &+ \frac{1}{2} \left(\left(\frac{\partial^2 G}{\partial n^2} \right)_c - \left(\frac{\partial^3 G}{\partial n^2 \partial \widetilde{B}} \right)_c \delta\widetilde{B} \right) (\delta n)^2 \\ &+ \frac{1}{3!} \left(\frac{\partial^3 G}{\partial n^3} \right)_c (\delta n)^3 \\ = &\, L\delta\widetilde{B}\delta n + Z(\delta\widetilde{B})^2 \delta n - \frac{1}{2} X \delta\widetilde{B} (\delta n)^2 + \frac{1}{3} M (\delta n)^3. \end{aligned} \tag{5.21}$$

Here we have chosen the arbitrary function $K(\widetilde{B})$ appearing in Eq. (5.17) such that all terms depending exclusively on $\delta\widetilde{B}$ (including the constant term) are cancelled. To arrive at the second equation we used Eqs. (5.19) and (5.20); the quantities L, M, X, and Z are defined in Eq. (5.7).

The form of $G(\delta n)$, see the inset of Fig 5.5, is typical for a first-order phase transition, where δn should be interpreted as the order parameter of the system [2]. By taking its derivative we retrieve the equation of motion (5.6): $d(\delta n)/dt =$

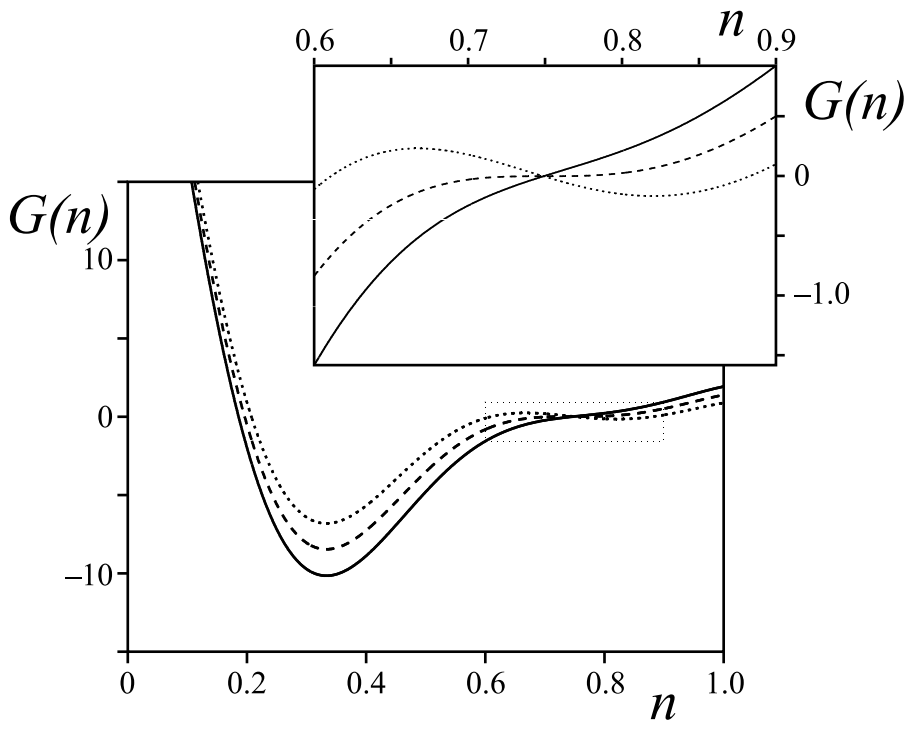

Figure 5.5: The potential function $G(n)$ ("free energy") around the critical value $\widetilde{B}_{c,N}$ for $N = 3$: (a) at $\widetilde{B} = 6.45$ (solid line), (b) at $\widetilde{B} = \widetilde{B}_{c,N} = 6.5527$ (dashed), and (c) at $\widetilde{B} = 6.65$ (dotted). The inset shows the neighborhood of the critical point at $n = n_{+,c} = 0.749$ in more detail. Note that the arbitrary function $K(\widetilde{B})$ in Eq. (5.17) has been chosen such that the three curves intersect at the bifurcation point $(n_{+,c}, G(n_{+,c}, \widetilde{B}_{c,N}))$.

$-\partial G(\delta n)/\partial(\delta n) = -L\delta\widetilde{B} - M(\delta n)^2 + X\delta n\delta\widetilde{B} - Z(\delta\widetilde{B})^2$. Starting out from $n = 1$ (all particles in the central box), the system has to pass the region around $n \approx n_{+,c}$. Here the slope of $G(\delta n)$ is very small [‡], i.e., the dynamics is very slow, and it is exactly this region which is responsible for the larger part of the lifetime τ. In Section 5.2.3 we showed that $\tau \propto (\delta\widetilde{B})^{-1/2}$, that is to say, it diverges with a mean field exponent $-1/2$.

Quantities of importance in this regime are the velocity $\dot{n}$ and acceleration $\ddot{n}$ of the decaying cluster. From Eq. (5.6) we immediately see that, for $\delta n = 0$, $\dot{n}$ is in leading order equal to $-L\delta\widetilde{B}$. For $\ddot{n}$ we find:

$$\ddot{n} = \frac{\partial\dot{n}}{\partial n}\dot{n} = \left(\frac{\partial^2 G}{\partial n^2}\right)\left(\frac{\partial G}{\partial n}\right) = -XL(\delta\widetilde{B})^2 + \mathcal{O}(\delta\widetilde{B})^3, \tag{5.22}$$

because from taking the derivative of Eq. (5.6) with respect to n we find that $\partial^2 G/\partial n^2 = X\delta\widetilde{B} + \mathcal{O}(\delta\widetilde{B}^2)$ for $\delta n = 0$. In the critical point itself ($\delta\widetilde{B} = 0$) both $\dot{n}$ and $\ddot{n}$ are zero, as well as all the other higher order derivatives, which is a general property of stationary points.

From a theoretical point of view it is interesting to note that from the recursive relation

$$\frac{d^k n}{dt^k} = \left(\frac{\partial G}{\partial n}\right)\left(\frac{\partial}{\partial n}\left(\frac{d^{k-1}n}{dt^{k-1}}\right)\right) \tag{5.23}$$

the leading order $\delta\widetilde{B}$-dependencies for arbitrary higher order time-derivatives of n near the critical point are found to be

$$\frac{d^k n}{dt^k} \propto \begin{cases} (\delta\widetilde{B})^{(k+2)/2} & \text{for even } k, \\ (\delta\widetilde{B})^{(k+1)/2} & \text{for odd } k. \end{cases} \tag{5.24}$$

Remarkably, successive pairs of the higher order derivatives have the same scaling behavior: the derivatives $k = 2$ and 3 both scale as $(\delta\widetilde{B})^2$, the derivatives $k = 4$ and 5 as $(\delta\widetilde{B})^3$, etc.

On the other side of $\widetilde{B}_{c,N}$ the cluster is stable. Setting $d(\delta n)/dt = 0$, we find a second order approximation for the equation of state Eq. (5.19) near the critical point:

$$-L\delta\widetilde{B} - M(\delta n)^2 + X\delta n\delta\widetilde{B} - Z(\delta\widetilde{B})^2 = 0, \tag{5.25}$$

[‡]Actually, for the depicted function $G(n)$ at $\widetilde{B} = 6.45$ (i.e., $\delta\widetilde{B}/\widetilde{B}_{c,3} = 0.015$), the slope is only just small enough to qualify for the present mean-field description, cf. Fig. 5.4. For $\widetilde{B}$ closer to the critical value the slope is smaller, but the values $\widetilde{B}$ in Fig. 5.5 have deliberately been chosen rather far apart to show the difference between the three situations as clearly as possible.

and by solving this quadratic equation for δn we find that, for $\widetilde{B}$ slightly above the critical value (i.e. for *negative* values of $\delta\widetilde{B}$), the stable cluster fraction n_{cl} approaches its critical value $n_{+,c}$ with an exponent $1/2$:

$$\delta n = \sqrt{\frac{L}{M}(-\delta\widetilde{B})} - \frac{X}{2M}(-\delta\widetilde{B}) + \mathcal{O}(-\delta\widetilde{B})^{3/2}. \tag{5.26}$$

In retrospect, the above mean field analysis shows that the critical point conditions (5.19) and (5.20) determine the infinitesimal topology of the flow field around the bifurcation. Since the relations $\delta n \propto (-\delta\widetilde{B})^{1/2}$ and $\tau \propto \delta\widetilde{B}^{-1/2}$ both result from this topology, there exists an intimate link between the power-law behavior of the stable cluster just *above* $\widetilde{B}_{c,N}$ and the lifetime of its unstable counterpart just *below* $\widetilde{B}_{c,N}$. Moreover, the complete analysis is largely independent of the precise form of the flux function, provided that it is one-humped. Only if $F(n)$ is such that the inflection point of $G(n)$ is exceptionally flat the exponents are different. For instance, if the leading δn-contribution to G is not of third order anymore but of fifth order [i.e., $(\partial^3 G/\partial n^3)_c = 0$ and $(\partial^4 G/\partial n^4)_c = 0$] we find $\delta n \propto (-\delta\widetilde{B})^{1/4}$ and $\tau \propto \delta\widetilde{B}^{-3/4}$ respectively.

5.4 Conclusion

In conclusion, the delayed, abrupt collapse of a granular cluster in a compartmentalized system is *quantitatively* accounted for by the Eggers flux model. The observed cluster lifetime time has been analytically calculated as a function of the dimensionless driving parameter $\widetilde{B}$. Close to the stability threshold $\widetilde{B}_{c,N}$, which depends on the number of compartments N, the lifetime τ is found to diverge as $(\widetilde{B}_{c,N} - \widetilde{B})^{-1/2}$, with a critical exponent $-1/2$. A related and well-known example from nonlinear dynamics is type-I intermittency, where the average length of the laminar phases between intermittent burst of chaos diverges (close to the critical saddle-node bifurcation) in the same way [4, 5].

The critical breakdown is described by a potential formalism, revealing the close analogy to mean-field theories for a first order phase transition. It is in fact one of the rare examples of such a theory in which all coefficients can be expressed explicitly in the physical model parameters.

References

[1] D. van der Meer, K. van der Weele, and D. Lohse, *Sudden collapse of a granular cluster*, Phys. Rev. Lett. **88**, 174302 (2002).

[2] P.M. Chaikin and T.C. Lubensky, *Principles of condensed matter physics* (Cambridge University Press, Cambridge, 1995).

[3] L. Landau and E. Lifshitz, *Statistical physics, Part 1* (Pergamon, Oxford, 1980), 3rd ed.

[4] Y. Pomeau and P. Manneville, *Intermittent transition to turbulence in dissipative dynamical systems*, Comm. Math. Phys. **74**, 189 (1980).

[5] H.G. Schuster, *Deterministic chaos: An introduction* (VCH Verlag, Weinheim, Germany, 1995), 3rd ed., pp. 84-85.

Chapter 6

Coarsening Dynamics in a Vibrofluidized Compartmentalized Granular Gas [‡]

Coarsening is studied in a vertically driven, initially uniformly distributed granular gas within a container divided into many connected compartments. The clustering is experimentally observed to occur in a two-stage process: First, the particles cluster in a few of the compartments. Subsequently, the clusters collapse one by one, at ever increasing timescales, until eventually only one large cluster remains. We find the same series of events in molecular dynamics simulations. To quantitatively account for the coarsening, we apply a flux model. It reveals the self-similar features of the process and allows to calculate the mean lifetime of the competing clusters. The size of the surviving clusters is found to grow anomalously slow as $[\log(t)]^{1/2}$.

6.1 Introduction

Coarsening is one of the most ubiquitous phenomena encountered in non-equilibrium systems [1]. It is the process by which the typical scale of patterns formed in such systems increases slowly but irreversibly with time. From the wide range of ex-

[‡]Devaraj van der Meer, Ko van der Weele, and Detlef Lohse, *Coarsening Dynamics in a Vibrofluidized Compartmentalized Granular Gas*, JSTAT **1** (in press, 2004).

amples, we mention domain coarsening in Ising ferromagnets and other two-phase systems [2–5], relaxation of deposited atoms into increasingly larger islands on a crystal surface [6], the growth of the average bubble size in aging foams [7, 8], the gradual ordering through pairwise annihilation of defects in time-dependent Ginzburg-Landau models [9–13], and coarsening stripes in driven lattice-gas models [14–17]. In addition, there is a close connection to jamming phenomena in glassy systems [18–21].

In granular gases, coarsening is related to the tendency to spontaneously separate into dense and dilute regions [22–25]. This clustering phenomenon can be traced back to the fact that the collisions between the particles are inelastic, which leads to a substantial energy loss in areas containing many particles. As a result,

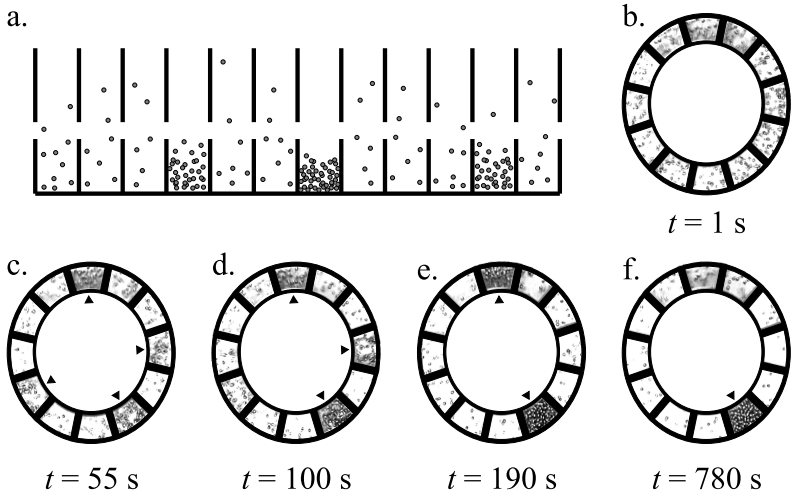

Figure 6.1: (a) Sketch of a vertically driven container partitioned into a cyclical array of 12 compartments connected by slits. Particles leaving the last compartment to the right enter the first from the left.
(b-f) Snapshots (top view) of an experiment in 12 compartments initially filled uniformly with 480 steel beads of radius $r = 1.18$ mm. The driving strength is well within the clustering regime ($f = 40$ Hz, $a = 1$ mm). The compartments lie on a ring with inner diameter 80 mm and outer diameter 104 mm; they are connected by 5.0 mm high slits located 25 mm above the bottom and extending from the inner to the outer ring.
The uniform distribution of particles at $t = 1$ s (b) quickly develops structures, of which the short lived transient with 4 clusters at $t = 55$ s is an example (c). At $t = 90$ s the system settles into a three cluster state (d), which at $t = 180$ s coarsens into a two cluster state (e), and on a much longer timescale (at $t = 770$ s) into the final state with only one cluster (f). The arrows in (b)-(f) mark the clusters.

dense regions become even denser, thereby emptying the spaces in between until these contain only a few (but relatively fast) particles.

6.2 Clustering and coarsening in a vibrofluidized granular gas

The clustering manifests itself in a particularly clear manner in a container that is divided into a series of N identical compartments, connected by slits in the wall between neighboring compartments, see Fig. 6.1a [26–30, 39, 40]. The system is vibrofluidized by shaking the box vertically. When the driving strength is reduced below a critical level, the particles cluster in a small subset of the compartments. Since states with multiple clusters are unstable [27], this pattern will coarsen to a dynamical equilibrium between 1 cluster and $N-1$ diluted compartments. This is seen in Fig. 6.1b-f, where we show a series of snapshots from a typical experiment of $N = 12$ cyclically arranged compartments, initially filled uniformly with 480 particles (Fig. 6.1b).

After we start shaking, there is a rapid emergence of structure in the system: In Fig. 6.1c at $t = 55$ s there are four clusters visible, one of which disappears soon thereafter, leading to the three-cluster state of Fig. 6.1d ($t = 100$ s). This state persists for about 90 s. Then, one of the clusters collapses, and its contents spread swiftly over the neighboring compartments to eventually land in the two remaining clusters (Fig. 6.1e). This state lasts for about 500 s, until again a cluster dies and we end up in the final single-cluster state (Fig. 6.1f).

The above process is well reproduced by a dynamical flux model elaborated in Section 6.3. A typical time-evolution evaluated from this model, for a system with twenty compartments, is shown in Fig. 6.2. Two distinct stages can be recognized in the coarsening process: the first one is the *cluster formation stage*, characterized by the relatively fast development of multiple clusters within the originally uniform system. In Fig. 6.2 this stage is completed at $t \approx 10^2$. It is followed by the actual *coarsening stage*, which takes place on a much larger timescale: the clusters disappear from the system one by one at ever increasing time-intervals.

Similar two-stage coarsening processes are also found in other granular systems, e.g., sand-ripples created by a periodic flow over a sand bed [31–34], shear-bands in a granular medium [35], non-compartmentalized driven granular gases [36, 37], or a freely cooling granular gas in one dimension [38].

The central question in any of these systems is: What are the typical timescales of the coarsening? Commonly it is found that the timescales grow exponentially. In our system however, Fig. 6.2 suggests that the successive time-intervals increase

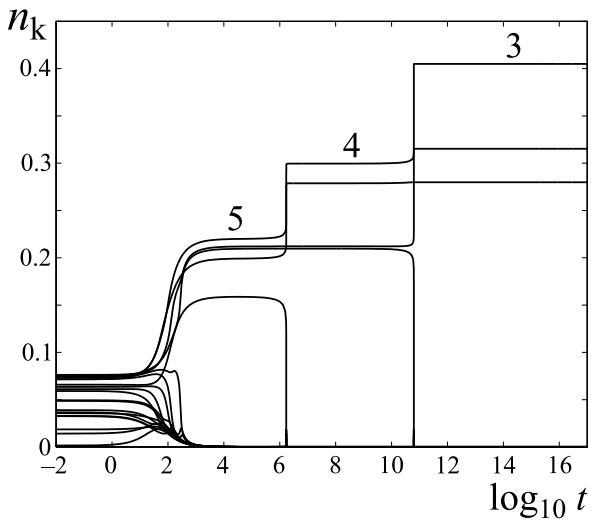

Figure 6.2: Time-evolution of the particle fractions n_k, $k = 1, 2, ..., 20$ (with $\sum n_k = 1$), in a system of 20 connected compartments, evaluated from the flux model introduced in Section 6.3. At $t \approx 10^2$, a five-cluster state emerges, while the other 15 compartments are depleted. The first two steps in the coarsening process (towards the final one-cluster state) occur around $t = 10^6$ and $t = 10^{11}$ respectively. The final two steps take place on an even longer timescale and are not depicted here ($t \gg 10^{18}$). Note the 18 orders of magnitude along the time axis.

even on a logarithmic scale, implying that they grow *super-exponentially*. Thus the coarsening in our system would be exceptionally slow.

It is the analysis and understanding of this coarsening process which will concern us in this chapter. Indeed, we will find that the lifetimes of the successive multi-cluster states grow super-exponentially and correspondingly that the size of the surviving clusters increases anomalously slow as $[\log(t)]^{1/2}$. This feature is directly linked to the asymptotic behavior of the flux from a dense compartment.

The structure of the chapter is as follows: In Section 6.3 we shortly review the flux model and the bifurcation diagrams for compartmentalized granular gases. Section 6.4 gives the coarsening analysis within the context of the flux model, and also an alternative (but equivalent) description of the particle dynamics between the clusters within a random walk view. In Section 6.5 we test several of the predictions of the flux model using molecular dynamics simulations. In Section 6.6 we present an analytical estimate of the typical time-scales, and in Section 6.7 all the previous results are integrated into a complete model for coarsening in a compartmentalized granular gas. Finally, in Section 6.8 we summarize the main findings.

6.3 Flux model and resulting bifurcation diagrams

Compartmentalized granular gases can, in a mean field sense, be adequately described by a flux model [26–28, 39, 40]. The main ingredient of this model is a non-monotonous flux function, which represents the outflow $F(n_k)$ of particles from a compartment into each of its neighbors in terms of the particle fraction n_k in that compartment. Based on the kinetic theory of granular gases, Eggers [39] derived the following approximate expression:

$$F(n_k) = C\sqrt{BN^2}n_k^2 e^{-BN^2 n_k^2}, \tag{6.1}$$

where the (dimensionless) driving parameter B is given by [26]:

$$B = 4\pi\,(1-e^2)^2\,\frac{gh}{a^2 f^2}\,\left(\frac{r^2 P}{\Omega N}\right)^2. \tag{6.2}$$

Here, h is the height at which the slits between the compartments are positioned, a and f are the amplitude and frequency of the driving, and e is the normal coefficient of restitution of the collisions between the particles. The other parameters are the ground area of the compartments (Ω), the particle radius (r), the number of compartments (N), and the total number of particles in the system (P).

The flux function Eq. (6.1) is one-humped: Starting out from zero for an empty compartment ($n_k = 0$), it first increases towards a maximum at $n_k = n_{max} = 1/\sqrt{BN^2}$, and subsequently decreases towards zero for higher particle fractions. It is this property that allows for the clustering effect: a dense and a dilute compartment are capable of generating the same flux and thereby balance each other. It is a consequence of the inelasticity of the collisions between the particles. For elastic particles ($e = 1$), the parameter B equals zero and the flux function F is a monotonously increasing function of the particle fraction. Hence, no clustering is possible.

The time rate of change dn_k/dt of the particle fraction in the k-th compartment is given by the inflow from its two neighbors minus the outflow from the compartment itself,

$$\frac{dn_k}{dt} = F(n_{k-1}) - 2F(n_k) + F(n_{k+1}), \tag{6.3}$$

with $k = 1, 2, .., N$ and cyclical boundary conditions. This balance equation leads to $\sum_{k=1}^{N} n_k = 1$, expressing conservation of the total number of particles.

As discussed in [27], from Eqs (6.1) and (6.3) we obtain the bifurcation diagram for an arbitrary number of compartments N, showing the fractions corresponding to stationary states of the system, $dn_k/dt = 0$, as a function of B. In

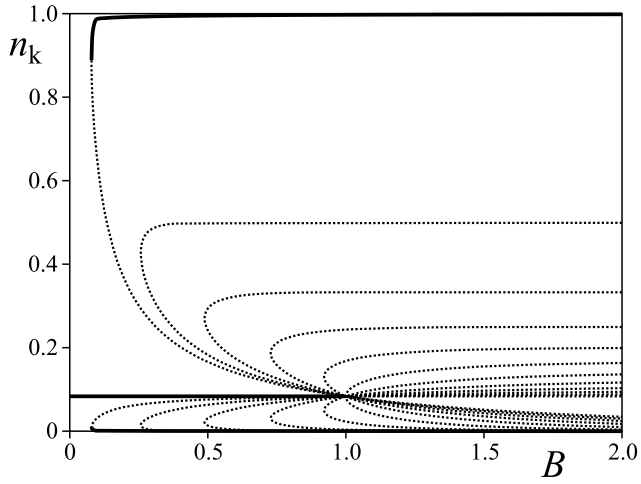

Figure 6.3: Bifurcation diagram for a system with $N = 12$ compartments: the stationary particle fractions n_k ($k = 1, ..., 12$) as a function of the driving parameter B. Only the uniform state for $B < B_C = 1$, and the outermost states with exactly one cluster are stable (solid lines). All the other branches correspond to unstable states (dashed lines). A detailed analysis of the construction and interpretation of this bifurcation diagram can be found in [27].

Fig. 6.3 we plot the bifurcation diagram for $N = 12$. If the driving parameter B is increased beyond the critical value $B_C = 1$, the uniform distribution ($n_k = 1/N$ for all k) becomes unstable. So if we start out from a homogeneous particle distribution, the system will travel through the large amount of dashed curves marking the unstable multi-cluster states (which are all saddle points with an increasing number of stable directions as the number of clusters goes down), slowly evolving to the solid curve which corresponds to a one-cluster state, which is the only stable situation beyond B_C. It is this trajectory that constitutes the coarsening process of a compartmentalized granular gas.

6.4 Clustering and coarsening within the flux model

Within the flux model the coarsening process can be studied by numerically integrating the equations of motion Eq. (6.3). In Fig. 6.4 we show four representative snapshots from the coarsening of a system consisting of $N = 50$ compartments: Initially the system is almost uniformly filled with material (Fig. 6.4a), and the shaking parameter is chosen just above the critical value: $B = 1.05$. Soon af-

ter the shaking is turned on, clusters start to form as illustrated by Fig. 6.4b (at $t = 7.2 \cdot 10^2$, with time measured in units of $C\sqrt{BN^2}$). In this situation most of the well-filled compartments are growing at the expense of the other compartments, but occasionally a cluster still emerges from the turmoil, as can be seen by comparing Figs. 6.4b and 6.4c (at $t = 2.1 \cdot 10^3$).

At this time there is a clear separation between the clusters, which are slowly growing, and an intermediate hilly pattern, from which material spills into the clusters; the cluster formation stage (the first stage in the coarsening process) is completed. At a certain later point in time the intermediate zones are depleted to such an extent that material can be transported from one cluster to another. This is seen to happen in Fig. 6.4d at $t = 1.8 \cdot 10^6$, where the two smallest clusters (cf. Fig. 6.4c) are losing material to their neighbors, until eventually the third cluster from the left disappears from the system (Fig. 6.4e).

In the remainder of this section we will first discuss what happens in the cluster formation stage and then analyze the coarsening stage, i.e., the depletion of the hilly pattern and the cluster-to-cluster transport.

6.4.1 The cluster formation stage

The first stage of the two-stage coarsening process begins with a nearly uniform distribution and ends with a state of a few clusters together with an intermediate hilly pattern, characterized by the simultaneous growth of all clusters and the presence of an appreciable amount of material between the clusters. At the beginning of this stage, it is hard to predict the pattern of clusters that will emerge, since in the neighborhood of the unstable uniform distribution, the system is very sensitive to the precise initial condition. At the end the pattern is fixed: Emergence of new clusters is not possible anymore, since the particle fraction in the intermediate region has dropped below the value for which the flux function has its maximum $n_{max} = 1/\sqrt{BN^2}$. On the other hand, collapse of clusters will not happen until at least one of the intermediate zones is depleted to such an extent that a cluster can start to shrink.

There are two crucial questions one can ask in this cluster formation stage: How many clusters are formed on average? And, what determines their size? To answer these questions, we start out from an ensemble of random initial conditions $n_k^{(0)}$ (drawn from a Gaussian distribution with mean $1/N$ and standard deviation σ) in a system with $N = 100$ compartments, and numerically integrate Eq. (6.3) for different values of B and σ. We repeat each simulation 1000 times and record the following quantities:

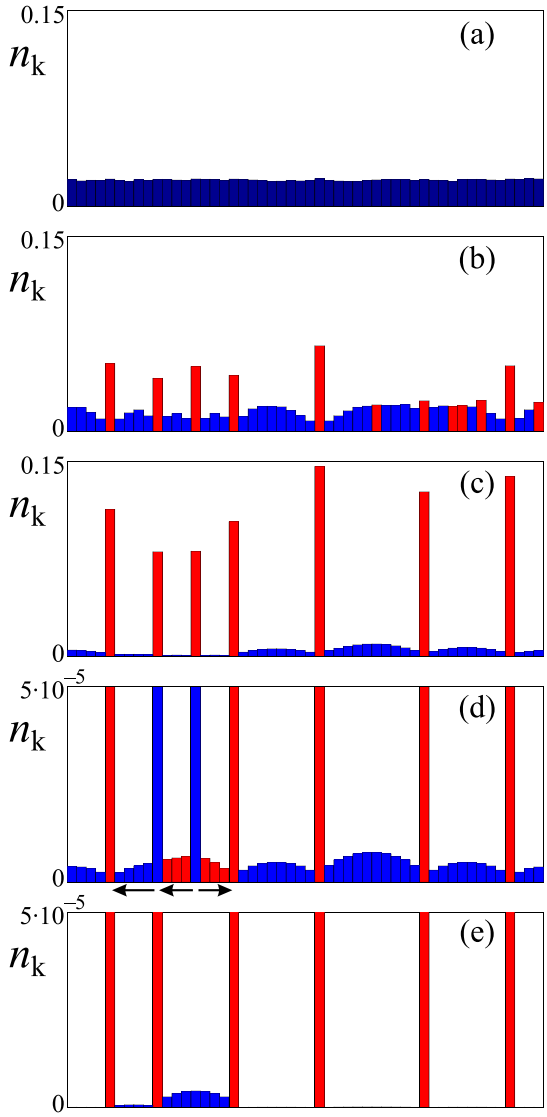

Figure 6.4: Four snapshots from the coarsening process within the flux model, with time measured in units of $C\sqrt{BN^2}$: (a) $t = 0$, initial state; (b) $t = 7.2 \cdot 10^2$, towards the end of the cluster formation stage; (c) $t = 2.1 \cdot 10^3$ depletion of the intermediate hilly pattern; (d) $t = 1.8 \cdot 10^6$, cluster-to-cluster transport, indicated by the arrows; (e) $t = 1.2 \cdot 10^8$, just after collapse of the third cluster from the left. The contents of this cluster have spread to its two direct neighbors, leaving a pronounced intermediate hill. Note the enlarged vertical scale in Figs. 6.4d and 6.4e.

- The distance m between neighboring clusters, defined as the number of compartments between the clusters plus one;
- The mass of each cluster, μ, defined (in the hilly pattern stage) as the fraction in the cluster compartment itself, plus half of the material in the left and right intermediate zones. This is the material that eventually will end up in the cluster (see also the next subsection);
- The support, Σ, of the cluster, which we define as half the distance to the two neighboring clusters. If m and m' are the distances between a certain cluster and its neighbors on the left and right, the support is given by $\Sigma = \frac{1}{2}(m + m') + 1$. Therefore, Σ is a half-integer.

In Fig. 6.5a we depict the distribution of distances between clusters for $B = 1.04$ and $\sigma = 0.02/N$. It is seen that it is extremely unlikely to obtain clusters in neighboring compartments from the given (almost uniform) initial distribution. This remains true for larger B, where the average distance between the clusters becomes smaller (cf. Fig. 6.6). The distribution of distances much larger than the average is consistent with an exponential.

In Fig. 6.5b we plot the cluster mass μ multiplied by the number of compartments in the system as a function of the support Σ of the cluster. For each value of Σ, μ forms a narrow distribution around Σ/N. Since the latter quantity corresponds to the fraction of material within the support of the cluster, this means that on average all the material that was *originally* present in the compartments belonging to the support ends up in the cluster. In other words, given a distribution of cluster distances m_α (resulting from any near-homogeneous initial condition) one can reasonably approximate the associated cluster fractions by $n_\alpha \approx \Sigma_\alpha/N$, where the index α runs over all clusters.

Finally, how does the average number of clusters depend on the driving parameter B? In Fig. 6.6 the fraction ν_{cl} of compartments containing a cluster is plotted as a function of $\delta B \equiv B - B_C$, starting from a Gaussian distribution with mean $1/N$ and standard deviation $\sigma = 0.02/N$. A clear power-law behavior is revealed:

$$\nu_{cl} \propto (\delta B)^\gamma\,, \quad \text{with } \gamma \approx 0.28, \tag{6.4}$$

where the exponent γ has been determined by taking the slope of a best fit through all but the first three data points in Fig. 6.6. The deviations for small values of δB can be attributed to having too large initial deviations from the uniform distribution compared to the positions of the adjacent non-uniform states near the critical point

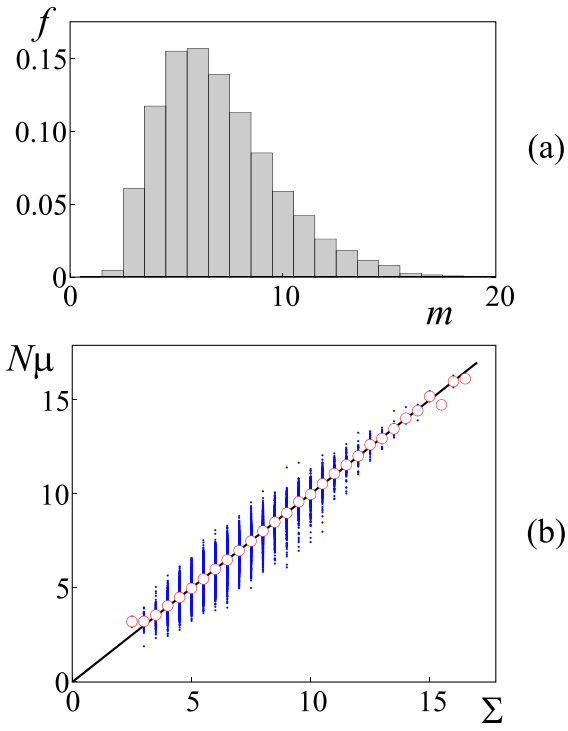

Figure 6.5: (a) Distribution of distances between adjacent clusters for $B = 1.04$ and $\sigma = 0.02/N$. (b) N times the cluster mass μ versus the support Σ of the cluster. The small (blue) dots are the individual data points, the (red) open circles are the averages calculated for each value of Σ. Note that the averages lie on the (black) line $N\mu = \Sigma$, for each value of Σ with suffi cient statistics.

B_C (cf. Fig. 6.3). This is confirmed by the data obtained for a somewhat smaller value of $\sigma = 0.01/N$ (the square symbols in Fig. 6.6). The dependence of ν_{cl} on the standard deviation of the initial distribution is however not strong, as can be seen from the inset of Fig. 6.6: at $\delta B = 0.04$ there is an increase of not more than 15% in ν_{cl} when varying σ from $0.005/N$ to $0.2/N$.

In all the above it was checked that the results remained the same also for a different total number of compartments in the system.

6.4.2 The coarsening stage

After the cluster formation stage we end up in a situation where we have clusters amidst an intermediate hilly pattern (Fig. 6.4c). Here the coarsening stage begins,

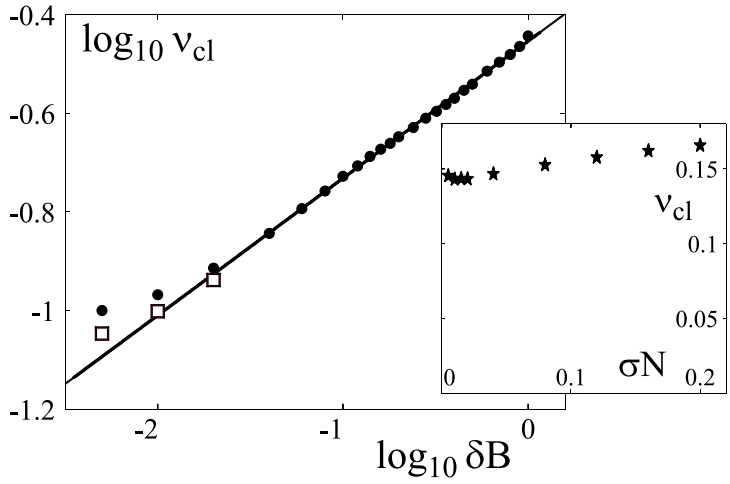

Figure 6.6: Doubly logarithmic plot of the fraction ν_{cl} of compartments containing a cluster at the end of the cluster formation stage as a function of $\delta B \equiv B - B_C$, with $\sigma = 0.02/N$ (circles) and $\sigma = 0.01/N$ (open squares). The slope of the best fit equals 0.28. The inset shows the dependence of ν_{cl} on the standard deviation of the initial conditions for $\delta B = 0.04$.

characterized by a steady depletion of the hilly pattern, followed by slow cluster-to-cluster transport. In Fig. 6.7 the time-evolution of the system depicted in Fig. 6.4 is plotted. After some short-lived initial turmoil, corresponding to the cluster formation stage, the coarsening stage sets in. There are two important features to distinguish:

- For most of the compartments the fraction continuously decreases with a slope of -1 in the doubly logarithmic plot, i.e., $n_k \propto 1/t$. These compartments correspond to the hills between the clusters (see Figs. 6.4c and 6.4d) and will be discussed in the next subsection.

- There are compartments for which the fraction does not change noticeably during substantial amounts of time (from $t \approx 10^6$ to 10^8 in Fig. 6.7). The state of these compartments correspond to the cluster-to-cluster transport of Fig. 6.4d. We will come back to this stage after the next subsection.

The clusters themselves show up as horizontal (nearly) straight lines on top of the plot.

Clearly, hilly patterns and cluster-to-cluster transport coexist in the system. The cluster-to-cluster transport state is always preceded by a hill-depletion zone in

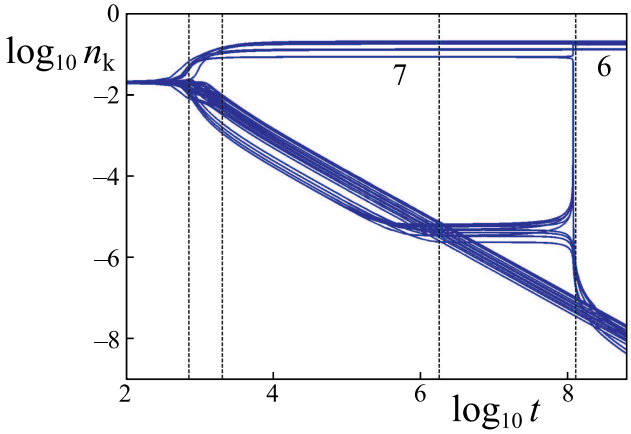

Figure 6.7: Time-evolution of the coarsening $N = 50$ compartments system depicted in Fig 6.4. For all fi fty compartments the logarithm of the fraction ($\log_{10} n_k$) is plotted as a function of the logarithm of time ($\log_{10} t$). The constant slope of the declining lines equals -1 to great precision, indicating the $1/t$ decay of the hilly pattern between the clusters. The vertical dashed lines correspond to the snapshots of Fig. 6.4b,c,d and e respectively. The numbers 7 and 6 in the plot refer to the number of clusters in the system.

the same compartments. And finally, the cluster-to-cluster transport state ends in an abrupt event in which one cluster collapses (at $t \approx 10^8$ in Fig. 6.7) and the two neighboring clusters gain its material; this rapid collapse is similar to the collapse of unstable clusters [28]. All these features will be discussed and analyzed in the next two subsections.

Depletion of the intermediate hilly pattern.

The hilly pattern between two clusters is characterized by depletion, i.e., material is flowing out of the region to the two adjoining clusters. The reverse flow from the clusters to the hilly pattern is negligible; for all practical purposes the clusters are acting as material sinks.

To quantitatively analyze what happens, let us assume that there are two clusters separated by a hilly depletion zone consisting of $m-1$ compartments, and have a look at the continuum limit of Eq. (6.3) by defining $n(x,t) \equiv n_k(t)/w$, where w is the width of a single compartment (cf. Ref. [28]). Mass conservation now reads $\int n(x,t)dx = 1$. We insert $n_{k+1}(t) = wn(x+w,t)$ and $n_{k-1}(t) = wn(x-w,t)$

into Eq. (6.3) and expand up to second order in w, yielding:

$$\partial_t n(x,t) = C'\sqrt{\widetilde{B}'}\,\partial_{xx}\left[n(x,t)^2 \exp\left(-\widetilde{B}' n(x,t)^2\right)\right], \tag{6.5}$$

with $\widetilde{B}' = B(Nw)^2$ and $C' = w^2 C$. Since the clusters on both sides of the depletion zone act as material sinks (absorbing boundaries) we have the following boundary conditions: $n(0,t) = n(L,t) = 0$, where $L = mw$ is the distance between the two clusters. Since the compartments in the depletion zone are very dilute ($n_k \ll 1/\sqrt{BN^2}$), we can approximate Eq. (6.5) by its dilute limit:

$$\begin{aligned} \partial_t n(x,t) &= A\partial_{xx}\left[n(x,t)^2\right], \\ n(0,t) &= n(L,t) = 0, \end{aligned} \tag{6.6}$$

where $A \equiv C'\sqrt{\widetilde{B}'}$. Our numerical results suggest that the hill decays in a self-similar way, and hence we try a self-similarity ansatz $\Gamma(\xi) = n(x,t)At/L^2$, where $\xi = x/L$, the form of which can be justified from dimensional analysis [41]. Inserting this ansatz, the above partial differential equation and boundary conditions transform into the following ordinary differential equation for the function $\Gamma(\xi)$:

$$\begin{aligned} \partial_{\xi\xi}[\Gamma^2] + \Gamma &= 0, \\ \Gamma(0) = \Gamma(1) &= 0. \end{aligned} \tag{6.7}$$

The solution of Eq. (6.7), which can be found numerically, corresponds to the hilly shape of the depletion zone (Fig. 6.8b).

Transforming back to the discrete $n_k(t)$ by using the definitions of A, C', $\widetilde{B}'$, Γ, and ξ, we find that:

$$n_k(t) = \frac{m^2\Gamma(\xi_k)}{C\sqrt{BN^2}}\,\frac{1}{t}, \quad \text{with } \xi_k \equiv \frac{k}{m+1}. \tag{6.8}$$

Note that from the above equation it follows that $n_k(t) \propto 1/t$, in full agreement with the observed decay of the hilly structure (cf. Fig. 6.7).

The expression found in Eq. (6.8) is correct for a system which initially contains an infinite amount of material, with two sinks at $k = 0$ and $k = m$. Within our system such an initial condition is never found, but the solution Eq. (6.8) is valid in the intermediate asymptotics sense [41]. That is, there are large deviations in the beginning (see Fig. 6.7 for $\log_{10} t < 3$), but as time grows the solution Eq. (6.8) is approached.

As an example, in Fig. 6.8a we see 20 consecutive curves, equidistant in time, from the evolution of a system described by Eq. (6.7) starting from an initial condition (not shown) in which $n(x, t = 0) = 1$ for all $0 < x < L$. In Fig. 6.8b the

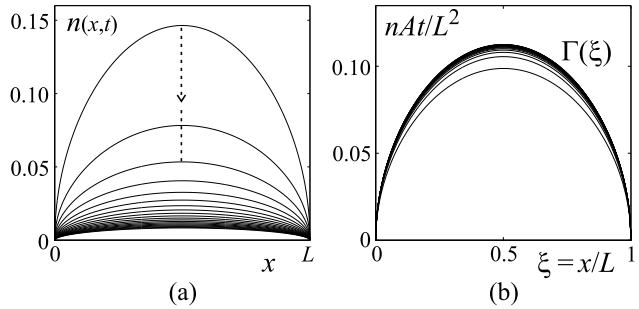

Figure 6.8: (a) Twenty consecutive snapshots $n(x, t_i)$ for the system described by Eq. (6.7). The initial condition (not shown) was $n(x, t = 0) = 1$ for all $0 < x < L$. The time-intervals between the successive t_i are constant. (b) The same curves as in Fig. 6.8a, but now in the rescaled variables $\xi \equiv x/L$ and $n(x, t)At/L^2$. The rescaled curves are seen to approach the self-similarity solution of Eq. (6.7) [$\Gamma(\xi)$, upper curve], confi rming the $1/t$ decay of the intermediate hills in the coarsening process.

same curves are plotted, but now rescaled by dividing x by L, and multiplying each curve $n(x, t)$ with a factor At/L^2. Then, as time increases, these rescaled curves approach the self-similar solution $\Gamma(\xi)$.

Slow cluster-to-cluster transport.

The depletion of the intermediate zones continues as long as the adjoining clusters act as sinks, i.e., as long as the back-flux from the clusters is negligible compared to the flux from the hilly pattern. At a certain moment, however, the flux *from* the hilly structure becomes comparable to the flux from one cluster *towards* the hilly structure. Now a net flux to the other cluster will develop and the hilly shape is transformed into a different pattern. After a comparatively short time, this new pattern hardly changes anymore: in this situation there is a constant net flux $\Phi_k \equiv F(n_k) - F(n_{k+1})$ through the zone (see Fig. 6.9), with material being transported from the smaller to the larger cluster.

The pattern is not completely stationary, but steepens slightly on a very long timescale, as dictated by the slowly changing outflow from the clusters, and thus by the cluster fractions.

To analyze the situation further, let us consider two clusters in compartments $k = 0$ and $k = m$, labelled α and $\alpha + 1$ respectively, connected by a transport zone of $m - 1$ compartments as in Fig. 6.9. Greek symbols are used for indices running over clusters only, to distinguish them from Roman indices labelling all

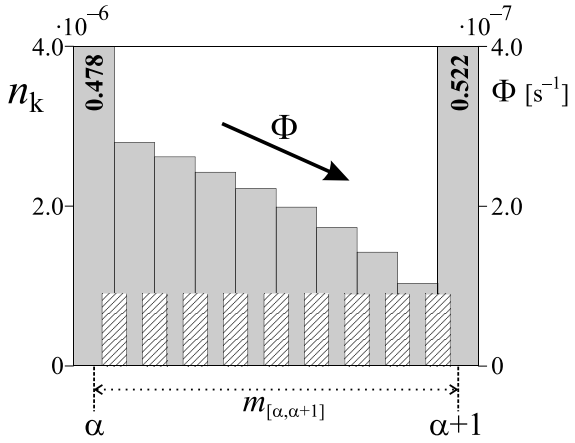

Figure 6.9: Intermediate zone with cluster to cluster transport. The solid bars show the fraction in the intermediate compartments; the particle fraction of the clusters (indicated on the first and tenth compartment) is orders of magnitude larger. The short dashed bars show the magnitude of the net flow $\Phi \equiv F(n_k) - F(n_{k+1})$, which is nearly constant throughout the profile (right axis). The particles flow from the smaller (left) to the larger cluster (right).

compartments. Since $\Phi_k \equiv \Phi$ is constant throughout the profile, we have $F(n_0) - F(n_1) = F(n_1) - F(n_2) = \Phi$, leading to $F(n_0) - F(n_2) = 2\Phi$. By iterating the above we get:

$$F(n_\alpha) - F(n_{\alpha+1}) = m_{[\alpha,\alpha+1]}\Phi_{[\alpha,\alpha+1]} \,, \tag{6.9}$$

where the index α runs over clusters only, and the subscript $_{[\alpha,\alpha+1]}$ is used to denote flux and distance between clusters α and $\alpha+1$. If on the other side of the cluster α there is also a transport zone consisting of $m_{[\alpha-1,\alpha]} - 1$ compartments we find an analogous equation for the net flux on the other side of cluster α and the time rate of change of the fraction in this cluster is then given by:

$$\begin{aligned} \frac{dn_\alpha}{dt} &= \Phi_{[\alpha-1,\alpha]} - \Phi_{[\alpha,\alpha+1]} \\ &= \frac{F(n_{\alpha-1}) - F(n_\alpha)}{m_{[\alpha-1,\alpha]}} + \frac{F(n_{\alpha+1}) - F(n_\alpha)}{m_{[\alpha,\alpha+1]}} \,. \end{aligned} \tag{6.10}$$

This *cluster-to-cluster* equation is a renormalized version of the original compartment-to-compartment equation Eq. (6.3): Instead of solving the balance equation for all compartments, we now only have to do so for those compartments that contain clusters, with the net flux $F(n_{\alpha+1}) - F(n_\alpha)$ being rescaled by the distance

$m_{[\alpha,\alpha+1]}$ between the clusters. Note that the timescale of the cluster-to-cluster dynamics is rescaled by $m_{[\alpha,\alpha+1]}$ and thus much slower.

Very dilute compartment dynamics

In the very dilute limit one may question the validity of the flux model description leading to the cluster-to-cluster equation. Indeed, the significance of time averaged fractions corresponding to particle densities far below one particle per compartment (and hence the validity of the flux model) is not at all obvious. In this section we therefore re-address the very dilute limit using an alternative approach. Surprisingly, we will end up with precisely the same cluster-to-cluster equation derived in the previous section.

Suppose that we have two clusters separated by $m-1$ empty compartments in which only very occasionally a particle resides. To be specific, the probability per unit time that a particle will go from cluster α to the neighboring (empty) compartment is given by $PF(n_\alpha)$, with P the total number of particles in the system. This particle then performs a series of solitary jumps through the intermediate compartments until it is absorbed again by either the cluster of origin, or the neighboring cluster.

We are not interested in the details of its path through the compartments, but only want to know to which of the two clusters it will eventually go. In other words, the question we want to answer is: Given that a particle has left the cluster (α) and entered the empty compartment next to it, what is the probability that it will eventually arrive in the next cluster ($\alpha+1$)? When a particle has entered an (empty) compartment, it is assumed to have an equal probability $p=1/2$ of moving either to the right or to the left neighbor. So, the particle will perform an unbiased random walk, starting from compartment $k=1$ until it is absorbed either by the cluster of origin α in compartment $k=0$ or by the target cluster $\alpha+1$ in compartment $k=m$ (see Fig. 6.10). In probability theory this problem is known as the gambler's ruin problem [42], and the probability p_m for the latter to happen has been shown to be equal to $1/m$. Because the derivation of this result is of relevance for this chapter it is given in Section 6.9, where also the generalization to a history dependent version is discussed.

Given the above, the probability per unit time that a particle travels from cluster α to $\alpha+1$ equals $PF(n_\alpha)p_m = PF(n_\alpha)/m$. Conversely, the probability per unit time that a particle travels from $\alpha+1$ to α is given by $PF(n_{\alpha+1})/m$, which gives a net particle flow towards α of $P[F(n_{\alpha+1})-F(n_\alpha)]/m$.

Thus, for the dilute case we find *exactly the same* cluster-to-cluster equation as

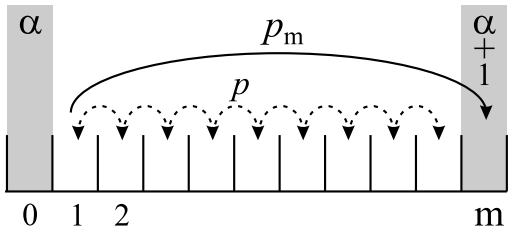

Figure 6.10: The particle performs an unbiased random walk in the (emptied) intermediate region between two clusters (dashed lines), until (with probability $p_m = 1/m$) it either lands in cluster $\alpha + 1$ at position $k = m$ or returns to the cluster α at $k = 0$.

from the flux model [(cf. Eq. (6.10)]:

$$\frac{dn_\alpha}{dt} = \frac{F(n_{\alpha-1}) - F(n_\alpha)}{m_{[\alpha-1,\alpha]}} + \frac{F(n_{\alpha+1}) - F(n_\alpha)}{m_{[\alpha,\alpha+1]}}. \tag{6.11}$$

6.5 Testing the predictions of the flux model

We performed molecular dynamics simulations to test the predictions of the flux model, in particular the predictions for the depletion of the intermediate hilly pattern and the cluster-to-cluster transport stage.

6.5.1 Testing the $1/t$ depletion of the intermediate hills

In order to test the prediction of the $1/t$ law for the depletion of the intermediate hills (cf. Section 6.4.2), a numerical experiment was devised within an N-compartment system, of which all but the outermost two compartments were initially uniformly filled with particles. Moreover, the bottom was removed from the first and the Nth compartment, in order to turn them physically into particle sinks. In this way we avoided having to simulate time consuming dense clusters in the outermost compartments.

In Fig. 6.11 we see the results of the average of four numerical simulations performed under identical conditions, for an intermediate zone of five compartments, containing initially 500 evenly distributed particles. Plotted is the total amount of particles P_t in the profile as a function of time in a doubly logarithmic plot.

After a short period in which predominantly the outer compartments lose material, the profile assumes a more or less hilly shape which decays according to a power-law. From a best fit on the data-points we find an exponent of -0.996, in

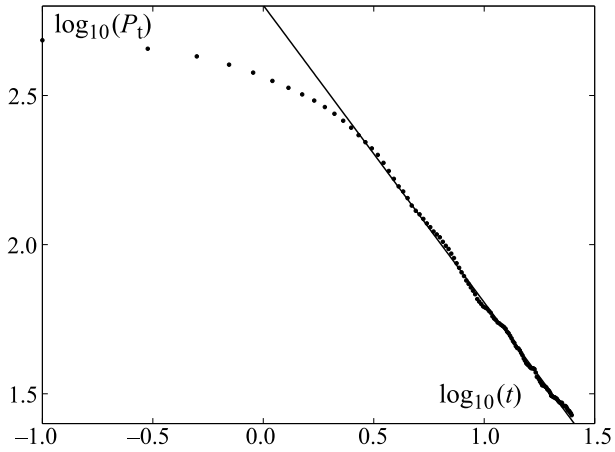

Figure 6.11: Doubly logarithmic plot of the time-evolution of the total amount of particles P_t in a row of 5 compartments with a bottomless compartment on each side. Initially each compartment contains 100 particles, and the system is driven by a sawtooth signal with amplitude 1.00 mm and frequency 100 Hz. The plot shows the averaged data from four simulation runs (dots), and a best fit through the data for $\log_{10}(t) > 0.6$ (line). The slope of the fit is equal to -0.996, in excellent agreement with the analytical prediction (-1) from the flux model.
Other parameter values are: ground area per compartment: 1.5 cm $\times$ 1.5 cm, position of the slits $h = 2.5$ cm, size of the slits: 1.5 cm $\times$ 0.5 cm, particle radius $r = 1.18$ mm, coefficient of restitution $e = 0.9$

excellent agreement with the exponent -1 obtained from the flux model. Note that $n_k(t) \propto 1/t$ implies that also $P_{int}(t) = P \sum n_k(t) \propto 1/t$ when we sum over all compartments in the depletion zone.

6.5.2 Testing the cluster-to-cluster equation

To test the cluster-to-cluster equation, we performed a molecular dynamics simulation within a (non-cyclical) system, with two clusters of initially $P_1 = 250$ and $P_{m+1} = 150$ particles respectively, separated by $m - 1$ empty compartments. The lifetime of the smaller cluster was measured as a function of m.

From the cluster-to-cluster equation Eq. (6.10) or (6.11) we infer that:

$$\frac{dn_{m+1}}{dt} = \frac{F(n_1) - F(n_{m+1})}{m}. \tag{6.12}$$

If we neglect the small amount of material in the intermediate compartments, and thus put $n_1 = 1 - n_{m+1}$, the above equation is readily integrated to give the lifetime

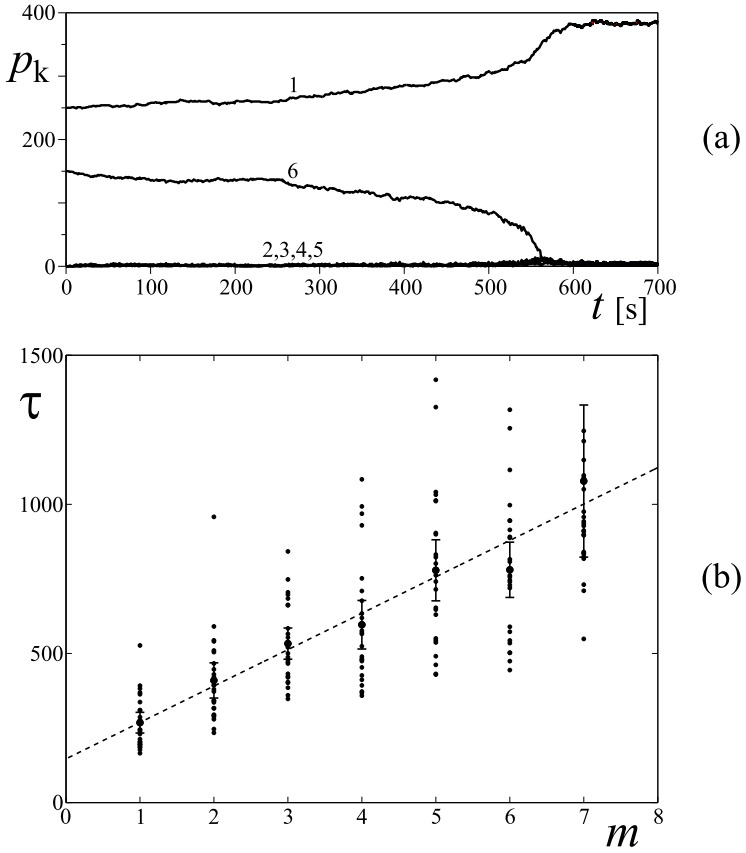

Figure 6.12: (a) Time-evolution of a system of six compartments, with initially particles only in the first ($P_1 = 250$) and the last ($P_6 = 150$) one. The distance between the clusters is $m = 5$. After shaking has started (using sinusoidal driving with $f = 24.0$ Hz and $a = 1.00$ mm), particles start to be transported from the smaller to the larger cluster, until, at $t = 560 \pm 20$ s, the smaller cluster vanishes. Its particles first spread over the intermediate compartments, to end up in the cluster in compartment 1 some 50 seconds later.
(b) Lifetime τ of the smaller cluster as a function of the distance m between the cluster. For each value of m the numerical experiment was repeated 25 times (dots); the larger symbols denote the average value, with the error bars indicating twice the estimated standard deviation. The dashed line is the best linear fit through the data.
Other parameters are as in Fig 6.11.

$\tau(m)$:

$$\tau(m) = m \int_{n_{thr}}^{n_0} \frac{dn}{F(n) - F(1-n)} \equiv m\,\tau(1), \tag{6.13}$$

where we dropped the label $m+1$. The integration goes from n_0 (the initial fraction of the smaller cluster) to n_{thr}, a small threshold fraction at which the smaller cluster is defined to have collapsed. Note that the lifetime $\tau(1)$ for two adjacent clusters is completely determined by the initial condition and threshold fraction in the two-compartment system. Thus, as Eq. (6.13) shows, the cluster-to-cluster equation predicts a linear proportionality between the lifetime $\tau(m)$ of the smaller cluster and the distance m between the clusters.

In Fig. 6.12a we find a typical time-evolution plot from the molecular dynamics simulation. Almost immediately after the start of the experiment, a slow particle transport from the smaller to the larger cluster sets in, which speeds up considerably after a certain point in time (here $t \approx 520$ s). The smaller cluster then collapses abruptly and its contents spread over the compartments, to eventually end up in the other cluster. Because of the abruptness of the collapse, the choice of the threshold value n_{thr} in Eq. (6.13) is not very critical.

To test the proportionality between τ and m, we repeated the simulation 25 times for each $m = 1, ..., 7$. The results are presented in Fig. 6.12b, from which a number of observations can be made. First, as a result of the statistical fluctuations in flux and particle number, there is quite a large spread in the lifetimes for each m. For $m = 7$ there was one observation in which the lifetime happened to be *four* times as large as the average value. Secondly, the lifetime is clearly an increasing function of m, but the relationship appears to be somewahat more intricate than the simple proportionality predicted by Eq. (6.13). From the best fit through the data a linear relationship between m and τ seems all right, but there is a substantial offset. Experiments on the 2-cluster system show the same behavior.

There are several possible causes for this offset. First of all, the cluster-to-cluster equation only holds when the number of particles in the intermediate compartments does not change too rapidly. This condition is of course violated from the moment the cluster starts to collapse ($t \approx 520$ s in Fig. 6.12a), and thus Eq. (6.12) cannot be integrated down to n_{thr}. Large deviations however are not expected because of this. More importantly, during the simulation it was observed that the random walk of the particles in the intermediate compartments was *biased*, in the sense that two consecutive jumps in the same direction were more probable than two jumps in different directions. The original gambler's ruin model can be extended for this kind of (non-Markovian) behavior and then predicts indeed a linear relation with an offset. This is shown in Appendix A.

6.6 Timescales in the coarsening process

In this section we discuss how a given initial distribution of l clusters distributed over N compartments coarsens in time. The argument presented involves an estimate for typical cluster sizes and distances, and focuses on cluster-to-cluster transport, neglecting the intermediate profile depletion stage. A more complete treatment is given in the next section.

When starting out with an N-compartment system in which (after the cluster formation stage) there are l clusters present, the typical cluster size will be $\bar{n}_l = 1/l$, and the typical distance between clusters will be $\bar{m}_l = N/l$. Now let us concentrate on the cluster that will disintegrate first. In the transport stage we can use the cluster-to-cluster equation Eq. (6.10) with $m_{[\alpha,\alpha-1]} = m_{[\alpha+1,\alpha]} = \bar{m}_l$. If additionally we assume that the neighboring clusters are sufficiently larger than the collapsing cluster, such that $F(n_{\alpha-1}) \ll F(n_\alpha)$, $F(n_{\alpha+1}) \ll F(n_\alpha)$, Eq. (6.10) becomes:

$$\frac{dn_\alpha}{dt} = -2\frac{F(n_\alpha)}{\bar{m}_l}, \tag{6.14}$$

which can be integrated to give the typical lifetime of the cluster, i.e., of the l-cluster state:

$$\tau_l = \frac{\bar{m}_l}{2}\int_{n_{thr}}^{\bar{n}_l}\frac{dn}{F(n)} = \frac{\bar{m}_l}{2C\sqrt{BN^2}}\int_{n_{thr}}^{\bar{n}_l}\frac{\exp(BN^2n^2)dn}{n^2}. \tag{6.15}$$

Here we have used the functional form Eq. (6.1) for $F(n)$, and n_{thr} is the threshold value below which the cluster can be considered to have disappeared from the system [cf. Eq. (6.13)]. The above integral can be solved analytically:

$$\tau_l = \frac{1}{2C\sqrt{B}}\left[\sqrt{\pi}x\,\mathrm{erfi}(x) - \exp(x^2)\right]_{x=\sqrt{B}N/l}, \tag{6.16}$$

where the imaginary error function is defined as $\mathrm{erfi}(x) = (2/\sqrt{\pi})\int_0^x \exp(u^2)du$. We have not included the terms containing n_{thr} as they are negligible compared to the above ones for $\bar{n}_l$.*

Plotting the logarithm of the lifetime Eq. (6.16) as a function of the number of clusters in the system, we observe a superexponential increase of the lifetime as the number l decreases (Fig. 6.13a). And if we plot the associated average cluster size $\langle n\rangle$ (or the average cluster distance since they are proportional) as a function of time, we do not retrieve the logarithmic dependence ($\langle n\rangle \propto \log(t)$) found in

*It is instructive to write Eq. (6.16) in a slightly different way by putting $\exp(x^2) = \int_0^x 2u\exp(u^2)du$, with which we find $\tau_l = 1/(C\sqrt{B})[\int_0^x (x-u)\exp(u^2)du]_{x=\sqrt{B}N/l}$. Since $x-u$ is positive for all $u \in (0,x)$, this expression makes visible that τ_l is positive for all l.

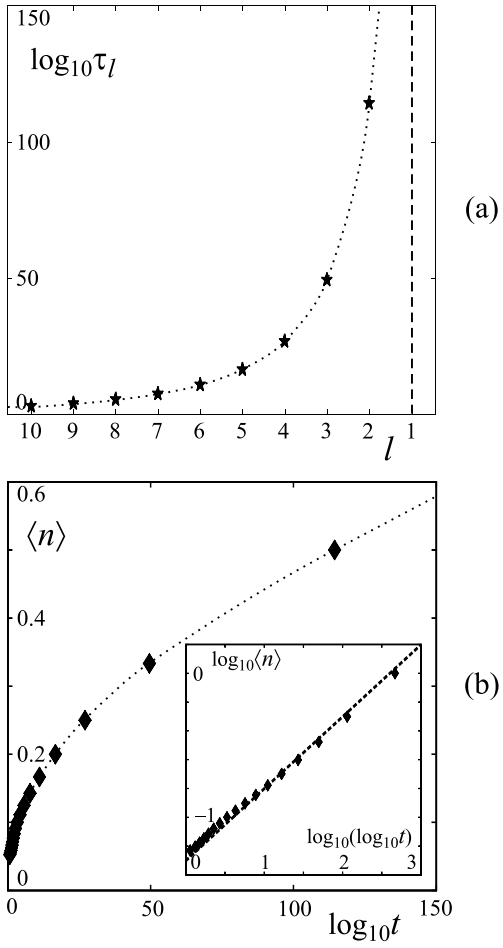

Figure 6.13: (a) Logarithm of the lifetime τ_l of the l-cluster state as a function of the decreasing number of clusters in the system as given by Eq. (6.16) with $N = 30$, $B = 1.2$ and $C = 1$. An exponential increase of the lifetime would be a straight line in this plot, so the increase is clearly superexponential.
(b) Average cluster size $\langle n \rangle$ versus the logarithm of time $\log_{10} t$, as calculated from Eq. (6.16) for the same parameter values. The inset shows the same data in a doubly logarithmic plot. The dashed straight line with slope $1/2$ reveals a good correspondence with the approximate expression Eq. (6.17), exposing an anomalously slow coarsening process with $\langle n \rangle \propto \sqrt{\log t}$. The dotted lines in the other plots are guides to the eye.

many other coarsening systems, but an anomalously slow growth of the cluster size (Fig. 6.13b). This can be understood by realizing that, in the l-cluster state, the average cluster size $\langle n \rangle$ equals $1/l$, and the lifetime of this state can be approximated [according to Eq. (6.16)] by $\tau_l \propto \exp(BN^2/l^2) = \exp(BN^2(\langle n \rangle)^2)$. So if we just set $t = \tau_l$ (since τ_l makes up by far the larger part of the total time t) this yields:

$$\langle n \rangle \approx \sqrt{\frac{\log(t)}{BN^2}}. \tag{6.17}$$

The inset of Fig. 6.13b shows the data in a doubly logarithmic plot together with a reference line with slope $1/2$. There is a good agreement with the $\log(t)^{1/2}$ behavior predicted by Eq. (6.17).

The growth of the average cluster size predicted by Eq. (6.17) is closely connected to the behavior of the flux function $F(n) \propto \exp(-BN^2n^2)$ in the limit of large particle fractions n [cf. Eq. (6.1)]. If the flux function would behave differently for large n, as is the case if one uses e.g. sinusoidally or triangularly shaped driving signals instead of the sawtooth form adopted in the derivation of Eq. (6.1), a different prediction for the time-evolution of the average cluster size will be found. It can be verified via an analysis analogous to the one given above that a purely exponential tail $F \propto \exp(-\widehat{B}n)$, leads to the traditional logarithmic growth law $\langle n \rangle \propto \log(t)$.

6.7 A comprehensive view of the coarsening process: synthesis of all stages

In this section we present a comprehensive view of the coarsening process in which many of the results obtained thus far are combined. The timescales obtained from this synthesis are in good agreement with the approximate result of the previous section.

Directly integrating the balance equations Eq. (6.3) through the complete coarsening process is a considerable task, since time scales become extremely large and the fractions in the intermediate compartments will get very small compared to the fractions in the clusters. This asks for extremely flexible integration schemes and high numerical precision. Checking the results of the previous subsection against numerical solutions of Eq. (6.3) for which one needs a huge number of repetitions of the integration, is therefore hardly feasible. Here we present a concise alternative way to calculate the state of the coarsening compartmentalized granular gas as a function of time, starting from an arbitrary initial distribution of clusters.

Suppose that after the cluster formation stage we have a system of l clusters

with fractions n_α at distances $m_{[\alpha,\alpha+1]}$ for $\alpha = 1, ..., l$. For convenience we take the compartments to be arranged cyclically. Note that: $\sum_{\alpha=1}^{l} m_{[\alpha,\alpha+1]} = N$, and also (if we neglect the small amount of material in the intermediate compartments) $\sum_{\alpha=1}^{l} n_\alpha = 1$. By the way, the fractions n_α and distances $m_{[\alpha,\alpha+1]}$ are not independent but related by the approximate expression:

$$n_\alpha \approx \frac{\Sigma}{N} = \frac{m_{[\alpha-1,\alpha]} + m_{[\alpha,\alpha+1]} + 2}{2N}, \tag{6.18}$$

as was shown in Section 6.4.1 (cf. Fig. 6.5b).

Now let us focus on the smallest cluster, labelled α. First the two hilly depletion zones on both sides of the cluster will be depleted as described by Eq. (6.8), Section 6.4.2, until the intermediate zones generate fluxes that are as small as the flux from the cluster itself, i.e., $F(n_k) \approx F(n_\alpha)$ (where k indicates the compartments in the intermediate zones). Since the fractions in the intermediate zones are very small, we can approximate $F(n_k) \approx C\sqrt{BN^2}n_k^2$, from which we find: $n_k \approx n_\alpha \exp(-BN^2 n_\alpha^2/2)$. Inserting this expression into Eq. (6.8) gives the following depletion time of the intermediate zone at the right hand side of the cluster:

$$\tau_{[\alpha,\alpha+1]}^{(depl.)} = (m_{[\alpha,\alpha+1]})^2 \, \frac{\Gamma(1/2)}{C\sqrt{BN^2}n_\alpha} \, \exp\left(\frac{BN^2 n_\alpha^2}{2}\right), \tag{6.19}$$

where Γ is the solution of Eq. (6.7), with $\Gamma(1/2) \approx 0.113$. A similar expression holds for the left depletion zone.

After the depletion of the intermediate zones, material will be transported from the cluster to its neighbors, which will be described by the cluster-to-cluster transport equation Eq. (6.10), Section 6.4.2. Under the assumption that the neighboring clusters are sufficiently larger (such that their outflow can be neglected) we find [cf. Eq. (6.16)]:

$$\frac{dn_\alpha}{dt} = -\left[\frac{1}{m_{[\alpha-1,\alpha]}} + \frac{1}{m_{[\alpha,\alpha+1]}}\right] F(n_\alpha)\,. \tag{6.20}$$

This equation, like Eq. (6.16), Section 6.6, can be integrated to give the transport time of the material in the cluster:

$$\tau_\alpha^{(trans.)} = \frac{1}{C} \, \frac{m_{[\alpha-1,\alpha]} m_{[\alpha,\alpha+1]}}{m_{[\alpha-1,\alpha]} + m_{[\alpha,\alpha+1]}} \left[\sqrt{\pi}\,\mathrm{erfi}(x) - \frac{\exp(x^2)}{x}\right]_{x=\sqrt{BN^2}n_\alpha}. \tag{6.21}$$

It may be objected that in general the two intermediate zones are not emptied at (about) the same time, which gives rise to a hybrid scenario in which the cluster

will lose material to one of its neighbors while it is still being supplied with material from the intermediate zone at the other side. To circumvent this, we have substituted the actual course of events by one in which the depletion continues on both sides until the *average* depletion time of the left and right zone, followed by synchronous cluster-to-cluster transport towards both sides.

From Eq. (6.19) it follows that $\tau^{(depl.)} \propto [\exp(BN^2 n_\alpha^2)]^{1/2}$ whereas (as argued in Section 6.6) $\tau^{(trans.)} \propto \exp(BN^2 n_\alpha^2)$. So:

$$\tau^{(depl.)} \propto [\tau^{(trans.)}]^{1/2}, \tag{6.22}$$

i.e., the transport time is typically much larger than the intermediate hill depletion.

Summing up, the total time needed for the cluster to collapse is the average Eq. (6.19) for the two intermediate zones plus the transport time Eq. (6.21):

$$\tau_\alpha = \frac{\tau^{(depl.)}_{[\alpha,\alpha+1]} + \tau^{(depl.)}_{[\alpha-1,\alpha]}}{2} + \tau^{(trans.)}_\alpha \ . \tag{6.23}$$

This gives the time until collapse for the smallest cluster in the system. The cluster then disappears from the system, spreading its contents evenly over the two neighboring clusters, which now get new fractions $n'_{\alpha-1} = n_{\alpha-1} + n_\alpha/2$ and $n'_{\alpha+1} = n_{\alpha+1} + n_\alpha/2$ respectively. Moreover, the collapsing cluster leaves behind an intermediate zone of size $m_{[\alpha-1,\alpha+1]} + m_{[\alpha,\alpha+1]}$ which immediately starts to be depleted, soon converging to the self-similar profile of Eq. (6.8).

This leads us to the following recipe for the fast calculation of the coarsening of the system:

1. Start from the initial distribution of l clusters with fractions n_α at distances $m_{[\alpha,\alpha+1]}$ for $\alpha = 1, ..., l$.

2. Calculate for all α the total time τ_α before collapse using Eqs. (6.19) - (6.23).

3. Determine the cluster with the smallest collapse time, spread its contents over the two neighboring compartments, and update the time τ_α for those two neighbors (by updating the two depletion times and transport time for both of them).

4. Repeat the previous step until only one cluster is left in the system.

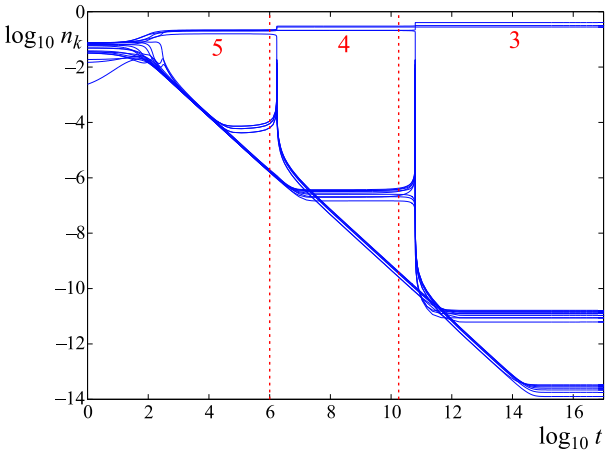

Figure 6.14: Time evolution of a system consisting of $N = 20$ compartments, with $B = 1.5$ and $C = 1/(\sqrt{B}N)$, found by direct numerical integration of Eq. (6.3) (solid lines). The recipe described in the text predicts the right order in which the individual clusters collapse; the quantitative agreement of the predicted collapse times (vertical dashed lines) with the numerical solution of the equations of motion is satisfactory. The numbers in the plot indicate the number of clusters in the system.

In Fig. 6.14 the results from a calculation of lifetimes τ_α using the above recipe are compared to a full numerical integration of the equations of motion Eq. (6.3). The agreement is satisfactory.

The main source of inaccuracy of the recipe is its tendency to underestimate the collapse time of a cluster if its neighbor happens to be of similar size. Suppose that we have two such clusters, with fraction n and $n + \epsilon$ respectively, and want to know under what conditions the outflux of the second cluster is below a certain fraction, say 0.01, of the first. This gives:

$$\begin{aligned} 0.01 &> \frac{F(n+\epsilon)}{F(n)} = \left(\frac{n+\epsilon}{n}\right)^2 \exp(-BN^2\epsilon(2n+\epsilon)) \\ &\approx \exp(-2BN^2 n\epsilon), \end{aligned} \tag{6.24}$$

which can be rewritten as:

$$\frac{\epsilon}{n} \gtrsim \frac{2.3}{B(Nn)^2} \approx \frac{2.3}{B}\left(\frac{l}{N}\right)^2, \tag{6.25}$$

where l is the number of clusters in the system. In the last step we used the approximation $n \approx 1/l$. From Eq. (6.25) we can conclude that the approximations

made in formulating the recipe will become better as the number of clusters in the system decreases, since the margin within which clusters must be considered to be of similar size becomes narrower as l gets smaller. For instance, for a system with $N = 30$ compartments and $l = 6.7$ (the average number of clusters for the system of Fig. 6.13, with $B = 1.20$) we find that $\epsilon/n \gtrsim 0.097$, so clusters which differ by 10% will already slow down cluster-to-cluster transport. If, for the same system we look at the 3-cluster state ($l = 3$), then the critical difference has considerably decreased to $\epsilon/n \gtrsim 0.019$.

This framework can be used to study the timescales τ_l and cluster size evolution also studied in the Section 6.6, but now within a more realistic setting, i.e., beyond the averages used there. By numerically integrating Eq. (6.3) from a nearly uniform initial distribution as described in Section 6.4.1 ($N = 30$, $B = 1.2$, and $C = 1$), we obtained a set of 500 initial conditions in terms of cluster sizes and distances. These were used as input for the recipe, from which lifetimes τ_l for the l-cluster state were obtained, as well as the cluster size as a function of time. In Fig. 6.15 the results are compared with the findings from the Section 6.6 (cf. Fig. 6.13).

The logarithm of the lifetime τ_l as a function of the decreasing number of clusters is plotted in Fig. 6.15a. Note that the lifetimes for the data from the recipe are substantially *larger* than those based on the typical cluster sizes. This points to the fact that the larger-than-average clusters add considerably to the mean lifetime. Because the recipe underestimates the lifetimes of adjacent clusters that are almost equal in size, it is expected that a full numerical solution of the equations of motion would lead to even higher τ_l.

In Fig. 6.15b we show the average cluster size $\langle n \rangle$ versus the logarithm of time $\log_{10} t$. The data from both methods lie on a single curve. Note the gap in the recipe data between $\langle n \rangle \approx 0.33$ and $\langle n \rangle \approx 0.42$. This gap originates from the fact that, starting from a nearly uniform distribution, the distances $m_{[\alpha,\alpha+1]}$ at the end of the cluster formation stage are not uniformly distributed but follow a distribution as in Fig. 6.5a, and that they are related to n_α via Eq. (6.18) [cf. Fig. 6.5b]. Since some cluster distances (and hence sizes) are highly improbable or even impossible, the corresponding cluster distributions in the l-cluster state are hardly ever reached, leading to peaks, valleys and even gaps in the overall cluster size distribution of the system[†].

[†]Of course one could prepare the system in a certain non-uniform state and reach cluster sizes and distances within the gap.

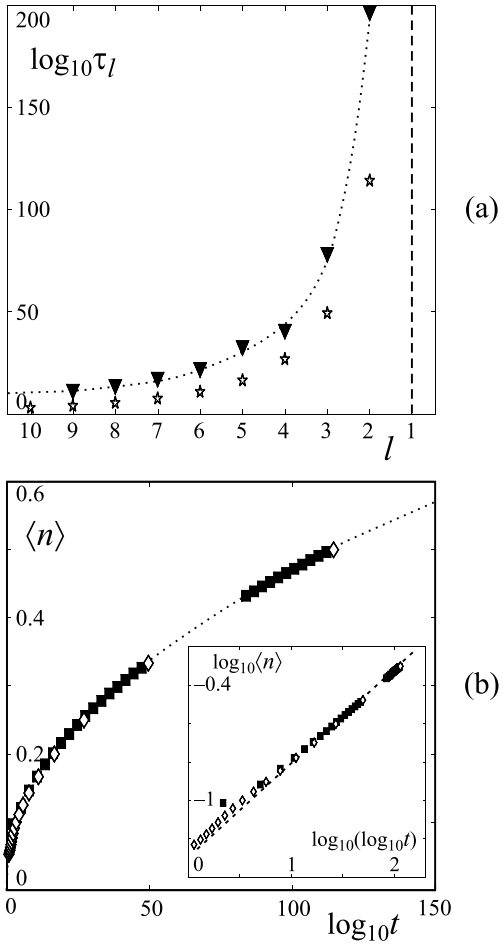

Figure 6.15: Results from a coarsening analysis starting out from random, nearly homogeneous initial conditions (as in Section 6.4.1) to obtain a set of realistic cluster fractions and distances as input for the recipe of Section 6.7. The same parameter values were taken as in Fig. 6.13, i.e., $N = 30$, $B = 1.2$, and $C = 1$.
(a) Logarithm of the average lifetime τ_l of the l-cluster state as a function of the decreasing number of clusters. The data obtained from the recipe in Section 6.7 (solid triangles) are substantially larger than those based on typical cluster sizes and distances [open stars, cf. Eq. (6.16) and Fig. (6.13)a]. The dotted line is to guide the eye.
(b) Average cluster size $\langle n \rangle$ versus the logarithm of time $\log_{10} t$ for the recipe data (solid squares) and the data based on typical cluster size and distance (open diamonds, cf. Fig. 6.13b). Both sets of data lie on the same curve and agree well with the anomalously slow coarsening law of Eq. (6.17) (inset). The gap in the recipe data for $\langle n \rangle \in (0.33, 0.42)$ is explained in the text.

6.8 Summary

In conclusion, we have studied the coarsening of a compartmentalized granular gas by means of experiments, molecular dynamics simulations, and a dynamical flux model. We found that the coarsening is a two-stage process: It starts out with a cluster formation stage, in which the distance between the clusters and hence the number of clusters in the system scales as a power-law $(\delta B)^\gamma$. Here δB is the distance of the driving parameter B to the critical value B_C where the uniform distribution becomes unstable, and $\gamma \approx 0.28$.

The second stage is the actual coarsening stage, in which the clusters collapse one by one. It includes a period of time in which the intermediate, dilute compartments between the clusters are depleted as $1/t$. This is followed by a much longer period of cluster-to-cluster transport, which eventually leads to the collapse of one of the clusters leaving again a depletion zone, and a smaller number of clusters.

Both stages are analyzed and explained within the context of the flux model. Besides, the cluster-to-cluster transport has also been treated using a random walk model for the dynamics in the almost empty intermediate zones. All the findings have been tested through molecular dynamics simulations.

To analyze the long-term behavior of the system (which is hard to attain directly) we have used two approaches: A short one considering typical cluster sizes and distances, and a comprehensive approach, based on all previously obtained knowledge of cluster formation, intermediate zone depletion, and cluster-to-cluster transport. Both approaches show that coarsening in a compartmentalized granular gas is anomalously slow: The lifetime τ_l of the l-cluster state grows superexponentially with decreasing number of clusters l, and the average cluster size $\langle n \rangle$ does not follow the $\log(t)$ dependence encountered in many other coarsening systems, but is shown to grow as $\sqrt{\log(t)}$ only. This feature is closely linked to the precise asymptotic form of the flux function in the limit of large particle fractions.

6.9 Appendix: The modified gambler's ruin problem

Facing a game with a probability p per bet to win a certain sum of money (say 1\$) and a probability $1 - p$ to lose 1\$, the gambler's ruin problem is the following well-known dilemma for any player with limited funds: If he starts out with 1\$, what are the odds that, after an arbitrary number of bets, he will end up with either the target sum of m\$, or with nothing at all because his capital is reduced to zero.

In the context of the cluster-to-cluster transport in the very dilute limit the *original* gambler's ruin model is formulated as follows. A particle which has just left one of the clusters will perform a random walk (biased or unbiased) in the $m-1$ compartments that separate him from the next cluster until the particle either lands in the rightmost cluster ($\alpha+1$) in compartment $k=m$, or returns to the cluster of origin α at $k=0$ (cf. Fig. 6.10.)

Let p denote the probability that the particle takes one step to the right, and let $\mathcal{P}_m$ be the probability that the random walk ends in the rightmost cluster (see Fig. 6.16a, top).

Suppose the first step is taken to the right, i.e., in the first step the particle will move (with probability p) to compartment $k=2$. Then two complementary events can take place (Fig. 6.16a, bottom):

1. The particle moves around in compartments $k=2,...,m-1$ and eventually lands in cluster $\alpha+1$. This happens with probability $\mathcal{P}_{m-1}$.

2. The particle moves around in compartments $k=2,...,m-1$ to return, after an arbitrary number of steps, on position $k=1$. This happens with the complementary probability $(1-\mathcal{P}_{m-1})$.

In the latter case the particle finds itself back on its starting point, with, again, a probability $\mathcal{P}_m$ to get to cluster $\alpha+1$. We thus find a recursive relation between $\mathcal{P}_m$ and $\mathcal{P}_{m-1}$:

$$\mathcal{P}_m = p\left\{\mathcal{P}_{m-1} + (1-\mathcal{P}_{m-1})\mathcal{P}_m\right\}, \tag{6.26}$$

leading to:

$$\mathcal{P}_m = \frac{p\,\mathcal{P}_{m-1}}{(1-p)+\mathcal{P}_{m-1}}, \tag{6.27}$$

or, more conveniently, writing $c=(1-p)/p$:

$$\frac{1}{\mathcal{P}_m} = c\frac{1}{\mathcal{P}_{m-1}} + 1 = \sum_{k=0}^{m-1} c^k . \tag{6.28}$$

The last equation is obtained by iteration, and making use of the fact that $\mathcal{P}_1=1$. By evaluating the sum in Eq. (6.28), we obtain:

$$\mathcal{P}_m = \begin{cases} (1-c)/(1-c^m) & \text{if } p \neq 1/2 \text{ (biased random walk)} \\ 1/m & \text{if } p = 1/2 \text{ (unbiased random walk)} \end{cases} \tag{6.29}$$

The above result can be found in standard textbooks on probability theory [42]. It has also previously been applied in coarsening systems [14].

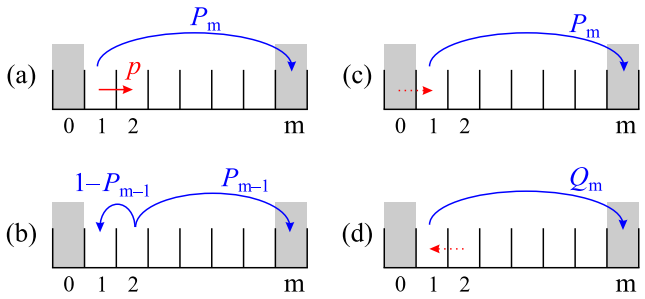

Figure 6.16: (a) Visualization of the probability $\mathcal{P}_m$ that the particle, after an arbitrary number of steps within compartments $k = 1, ..., (m-1)$ lands in the rightmost cluster at position $k = m$. (b) Visualization of part of the recursion relation Eq. (6.26): In the first step the particle moves with a probability p to compartment $k = 2$. From there, it has probability $\mathcal{P}_{m-1}$ of landing in the rightmost cluster and probability $1 - \mathcal{P}_{m-1}$ to return to compartment $k = 1$ (both after an arbitrary number of steps through the compartments $k = 2, ..., (m-1)$). (c)-(d) In the modified gambler's ruin model the probability of ending up in the rightmost cluster after a step to the right ($\mathcal{P}_m$), has to be distinguished from the probability for the same event to happen after a step to the left ($\mathcal{Q}_m$)

Inspired by the observation (see Section 6.5) that in our system two consecutive steps in the *same* direction are more probable than two steps in opposite directions, we now modify the gambler's ruin problem as follows. We denote the conditional probability for a step to the right if the first step was also to the right by $p(R|R) \equiv p$ and assume that the system is symmetric, which means $p(L|L) = p(R|R) = p$. Furthermore $p(R|L) = p(L|R) \equiv q$, with $p + q = 1$, since regardless of the previous step one has to step either to the left or the right.

Let $\mathcal{P}_m$ be again the probability that the random walk starting in the first compartment ends in the rightmost cluster, with the condition that the step into the first compartment was taken to the right (see Fig. 6.16b, top). In the present model this needs to be distinguished from the probability $\mathcal{Q}_m$ that the same event takes place preceded by a step to the left (Fig. 6.16b, bottom).

As before, we are in search for a recursive relation for $\mathcal{P}_m$. Since the particle originates from the cluster and hence the first step (towards compartment $k = 1$) was to the right, the probability of another step to the right, to $k = 2$, is p. Next we perform a random walk in compartments $k = 2, ..., m-1$ and end up either in the cluster at $k = m$ (with probability $\mathcal{P}_m$ since the previous step was to the right), or we return to compartment $k = 1$ with complementary probability $(1 - \mathcal{P}_m)$. This

is similar to the previous case, but now we have come to $k = 1$ by a step to the left, and hence from here on our probability of ending up in the cluster at $k = m$ is not $\mathcal{P}_m$ but $\mathcal{Q}_m$. So:

$$\mathcal{P}_m = p\,\{\mathcal{P}_{m-1} + (1 - \mathcal{P}_{m-1})\mathcal{Q}_m\}. \tag{6.30}$$

If we follow the same line of reasoning for a particle that originally came from $k = 2$ by a step to the left we find:

$$\mathcal{Q}_m = q\,\{\mathcal{P}_{m-1} + (1 - \mathcal{P}_{m-1})\mathcal{Q}_m\}. \tag{6.31}$$

By dividing Eqs. (6.30) and (6.31) we find that $\mathcal{P}_m/\mathcal{Q}_m = p/q$, which is a very plausible result: It reflects that the only difference between $\mathcal{P}_m$ and $\mathcal{Q}_m$ (with the particle following any sequence of steps to the next cluster) lies in the fact that $\mathcal{P}_m$ is preceded by a step to the right and $\mathcal{Q}_m$ by a step to the left. By inserting this result into Eq. (6.30) we find:

$$\mathcal{P}_m = \frac{p\mathcal{P}_{m-1}}{p + q\mathcal{P}_{m-1}}\,, \tag{6.32}$$

or:

$$\frac{1}{\mathcal{P}_m} = \frac{1}{\mathcal{P}_{m-1}} + \frac{q}{p} = (1 - \frac{q}{p}) + m\frac{q}{p}\,, \tag{6.33}$$

where the last step follows by iteration and $\mathcal{P}_1 = 1$. So we find:

$$\mathcal{P}_m = \frac{1}{1 + (m-1)(q/p)}\,. \tag{6.34}$$

If we use the above expression to derive the cluster-to-cluster equation, Eq. (6.12) takes the form

$$\frac{dn_{m+1}}{dt} = \frac{1}{1 + (m-1)q/p}\,\{F(n_1) - F(n_{m+1})\}. \tag{6.35}$$

and this leads to the following adapted form for the lifetime $\tau(m)$:

$$\tau(m) = \left((1 - \frac{q}{p}) + m\frac{q}{p}\right)\,\tau(1)\,. \tag{6.36}$$

We see that the dependence on the number of compartments is still linear [as in Eq. (6.13)] but there is an additional constant term $(1 - q/p)\tau(1)$, which accounts for the offset observed in the molecular dynamics simulations if $p \approx 0.7$ (see Fig. 6.12b).

References

[1] M.C. Cross and P.C. Hohenberg, *Pattern formation outside of equilibrium*, Rev. Mod. Phys. **65**, 851 (1993).

[2] D. A. Huse, *Corrections to late-stage behavior in spinodal decomposition: Lifshitz-Slyozov scaling and Monte Carlo simulations*, Phys. Rev. B **34**, 7845 (1986).

[3] J. Marro, J.L. Lebowitz, and M.H. Kalos, *Computer simulation of the time evolution of a quenched model alloy in the nucleation region*, Phys. Rev. Lett. **43**, 282 (1979).

[4] S. Katano and M. Iizumi, *Crossover phenomenon in dynamical scaling of phase separation in Fe-Cr alloy*, Phys. Rev. Lett. **52**, 835 (1984).

[5] E.D. Siggia, *Late stages of spinodal decomposition in binary mixtures*, Phys. Rev. A **20**, 595 (1979).

[6] C. Bréchignac, P. Cahuzac, F. Carlier, C. Colliex, J. Leroux, A. Masson, B. Yoon, and U. Landman, *Instability driven fragmentation of nanoscale fractal islands*, Phys. Rev. Lett. **88**, 196103 (2002).

[7] M.U. Vera and D.J. Durian, *Enhanced drainage and coarsening in aqueous foams*, Phys. Rev. Lett. **88**, 088304 (2002).

[8] S. Hilgenfeldt, S.A. Koehler, and H.A. Stone, *Dynamics of coarsening foams: Accelerated and self-limiting drainage*, Phys. Rev. Lett. **86**, 4704 (2001).

[9] G.F. Mazenko and R.A. Wickham, *Vortex annihilation in the ordering kinetics of the O(2) model*, Phys. Rev. E **55**, 5113 (1997).

[10] R.A. Wickham and G.F. Mazenko, *Phase ordering of the O(2) model in the post-Gaussian approximation*, Phys. Rev. E **55**, 2300 (1997).

[11] G.F. Mazenko, *Defect statistics in the two-dimensional complex Ginzburg-Landau model*, Phys. Rev. E **64**, 016110 (2001).

[12] H. Qian and G.F Mazenko, *Vortex dynamics in a coarsening two-dimensional XY-model*, Phys. Rev. E **68**, 021109 (2003).

[13] H. Qian and G.F Mazenko, *Defect structures in the growth kinetics of the Swift-Hohenberg model*, Phys. Rev. E **67**, 036102 (2003).

[14] E. Levine, Y. Kafri, and D. Mukamel, *Ordering dynamics of the driven lattice-gas model*, Phys. Rev. E **64**, 026105 (2001).

[15] M.R. Evans, Y. Kafri, E. Levine, and D. Mukamel, *Coarsening of a class of driven striped structures*, Phys. Rev. E **62**, 7619 (2000).

[16] Y. Kafri, D. Biron, M.R. Evans, and D. Mukamel, *Slow coarsening in a class of driven systems*, Eur. Phys. J. B **16**, 669 (2000).

[17] M.R. Evans, Y. Kafri, H.M. Koduvely, and D. Mukamel, *Phase separation and coarsening in one-dimensional driven diffusive systems: Local dynamics leading to long-range hamiltonians*, Phys. Rev. E **58**, 2764 (1998).

[18] A.J. Liu and S.R. Nagel, *Nonlinear dynamics: Jamming is not just cool any more*, Nature **396**, 21 (1998).

[19] C.S. O'Hern, S.A. Langer, A.J. Liu, and S.R. Nagel, *Force distributions near jamming and glass transitions*, Phys. Rev. Lett. **86**, 111 (2001).

[20] I.K. Ono, C.S. O'Hern, D.J. Durian, S.A. Langer, A.J. Liu, and S.R. Nagel, *Effective temperatures of a driven system near jamming*, Phys. Rev. Lett. **89**, 095703 (2002).

[21] C.S. O'Hern, L.E. Silbert, A.J. Liu, and S.R. Nagel, *Jamming at zero temperature and zero applied stress: The epitome of disorder*, Phys. Rev. E **68**, 011306 (2003).

[22] I. Goldhirsch and G. Zanetti, *Clustering instability in dissipative gases*, Phys. Rev. Lett. **70**, 1619 (1993).

[23] H.M. Jaeger, S.R. Nagel, and R.P. Behringer, *Granular solids, liquids, and gases*, Rev. Mod. Phys. **68**, 1259 (1996).

[24] L.P. Kadanoff, *Built upon sand: Theoretical ideas inspired by granular flows*, Rev. Mod. Phys. **71**, 435 (1999).

[25] I. Goldhirsch, *Rapid granular flows*, Annu. Rev. Fluid Mech. **35**, 267 (2003).

[26] K. van der Weele, D. van der Meer, M. Versluis, and D. Lohse, *Hysteretic clustering in a granular gas*, Europhys. Lett. **53**, 328 (2001).

[27] D. van der Meer, K. van der Weele, and D. Lohse, *Bifurcation diagrams of compartmentalized granular gases*, Phys. Rev. E **63**, 061304 (2001).

[28] D. van der Meer, K. van der Weele, and D. Lohse, *Sudden collapse of a granular cluster*, Phys. Rev. Lett. **88**, 174302 (2002).

[29] F. Coppex, M. Droz, and A. Lipowski, *Dynamics of the breakdown of granular clusters*, Phys. Rev. E **66**, 011305 (2002).

[30] U. Marini Bettolo Marconi and M. Conti, *Dynamics of vibrofluidized granular gases in periodic structures*, Phys. Rev. E **69**, 011302 (2004).

[31] J.L. Hansen, M. van Hecke, A. Haaning, C. Ellegaard, K.H. Andersen, T. Bohr, and T. Sams, *Instabilities in sand ripples*, Nature **410**, 324 (2001).

[32] J.L. Hansen, M. van Hecke, C. Ellegaard, K.H. Andersen, T. Bohr, A. Haaning, and T. Sams, *Stability balloon for two-dimensional vortex ripple patterns*, Phys. Rev. Lett. **87**, 204301 (2001).

[33] E.K.O. Hellén and J. Krug, *Coarsening of sand ripples in mass transfer models*, Phys. Rev. E **66**, 011304 (2002).

[34] K.H. Andersen, M. Abel, J. Krug, C. Ellegaard, L.R. Søndergaard, and J. Udesen, *Pattern dynamics of vortex ripples in sand: Nonlinear modeling and experimental validation*, Phys. Rev. Lett. **88**, 234302 (2002).

[35] T.P. Witelski, D.G. Schaeffer, and M. Shearer, *A discrete model for an ill-posed non-linear parabolic PDE*, Physica D **160**, 189 (2001).

[36] E. Livne, B. Meerson, and P.V. Sasorov, *Symmetry breaking and coarsening of clusters in a prototypical driven granular gas*, Phys. Rev. E **66**, 050301(R) (2002).

[37] S.A. Hill and G.F Mazenko, *Granular clustering in a hydrodynamic simulation*, Phys. Rev. E **67**, 061302 (2003).

[38] S. Ostojic, D. Panja, and B. Nienhuis, *Clustering in a one-dimensional inelastic lattice gas*, cond-mat/0310493.

[39] J. Eggers, *Sand as Maxwell's demon*, Phys. Rev. Lett. **83**, 5322 (1999).

[40] R. Mikkelsen, D. van der Meer, K. van der Weele, and D. Lohse, *Competitive clustering in a bidisperse granular gas*, Phys. Rev. Lett. **89**, 214301 (2002).

[41] G. Barenblatt, *Scaling, self-similarity, and intermediate asymptotics* (Cambridge Univ. Press, New York, 1996), 1st ed.

[42] W. Feller, *An introduction to probability theory and applications* (Wiley, New York, USA, 1968), 3rd ed.

Chapter 7

Spontaneous Ratchet Effect in a Granular Gas [‡]

The spontaneous clustering of a vibrofluidized granular gas is employed to generate directed transport in two different compartmentalized systems: a "granular fountain" *in which the transport takes the form of convection rolls, and a* "granular ratchet" *with a spontaneous particle current perpendicular to the direction of energy input. In both instances, transport is not due to any system-intrinsic anisotropy, but arises as a spontaneous collective symmetry breaking effect of many interacting granular particles. The experimental and numerical results are quantitatively accounted for within a flux model.*

7.1 Introduction: on the ratchet effect

The conversion of random fluctuations into directed motion in a periodic system – termed ratchet effect – is of interest in a wide variety of physical, biological, and technological contexts [1]. Overall, two necessary conditions for the emergence of the effect have been identified [2], namely (i) the absence of thermal equilibrium and (ii) the breaking of the inversion symmetry. The most common realization of the latter condition is by means of an intrinsic anisotropy in the system, e.g. a spatially periodic but asymmetric potential, or a so-called dynamical asymmetry due to a time-dependent driving force with zero mean but non-vanishing higher moments [2]. Here, we are concerned with *perfectly symmetric systems* where the symmetry breaking arises spontaneously as a collective effect of many interacting

[‡]Devaraj van der Meer, Peter Reimann, Ko van der Weele, and Detlef Lohse, *Spontaneous Ratchet Effect in a Granular Gas*, Phys. Rev. Lett. **92** (in press, 2004).

particles via an ergodicity breaking non-equilibrium phase transition [3, 4]. While a proof of principle for this so-called spontaneous ratchet effect has been provided theoretically with several different "minimal models" [2–4], we explore here for the first time a *real* system, namely a vibrofluidized granular gas, experimentally, numerically, and analytically.

Transport in granular systems due to a ratchet effect has been previously demonstrated both for asymmetric potentials [5–7] and for dynamical asymmetries [8, 9]. While in both these cases even a single granular particle moves in a preferential direction, the spontaneous ratchet effect we consider here is a genuine *collective phenomenon*. The underlying mechanism is the enhanced energy loss in already dense regions of a granular gas due to the inelastic collisions, resulting in a spontaneous separation into dense and dilute regions [10–12]. This clustering effect can be controlled by confining the particles to a series of compartments that are connected by small apertures (slits) and subjected to gravity [13–19]. When the granular system is fluidized by shaking it vertically, the particles cluster into the compartments which are initially or due to random fluctuations slightly denser, until a dynamical equilibrium is established in which the particle flux out of a compartment is balanced by the influx coming from its neighbors.

Hence, all ingredients for a spontaneous ratchet effect are present: First, random fluctuations in the form of deterministic noise are created intrinsically by the chaotic dynamics. Second, the system is kept away from thermal equilibrium by the vertical vibrations. Third, in a perfectly symmetric, periodic compartmentalization, stable steady states with a spontaneously broken symmetry yet still respecting the periodicity seem possible, but are not at all obvious: their actual existence is the main finding of our present work.

7.2 The granular fountain

We start with a granular gas in a container that is divided into $N = 2$ equal compartments by a wall with a slit at a certain height h. At vigorous shaking, this system has a unique steady state with an equal population of both compartments [13–16]. Upon reducing the driving, this symmetric state loses stability via a continuous phase transition, resulting in a pair of stable solutions with spontaneously broken symmetry: They are clustered states with one diluted and one crowded compartment [13–16]. If we now add a sufficiently small hole at the bottom of the wall separating the compartments, the clustered states are expected to subsist (see Fig. 7.1a), resulting in a particle flow through the hole, balanced by a flow through the slit in the opposite direction. We thus expect a "*granular*

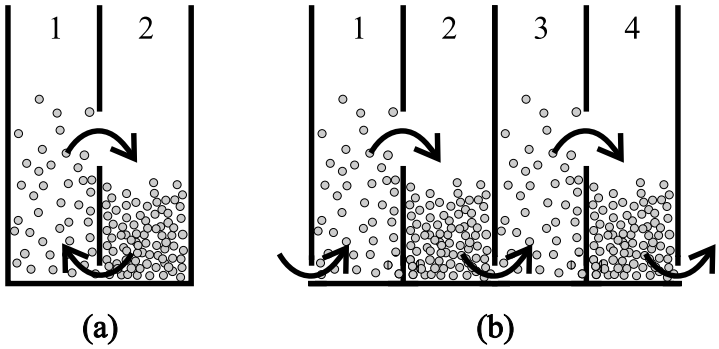

Figure 7.1: (a) Schematic cross section of a granular fountain exhibiting spontaneous symmetry breaking into a "cold" and a "hot" compartment and a concomitant spontaneous circular particle flow. (b) By folding out the geometry of several adjacent fountains, and adding cyclical boundary conditions, a granular ratchet is obtained with almost unchanged populations of the respective compartments and the particle currents between them (here shown for $N = 4$ compartments).

fountain", i.e. a spontaneous convective flow, imposed upon the system by the clustering phenomenon.

To verify these predictions, we conducted both experiments and molecular dynamics simulations. In the *experiments* we used $P = 407$ beads of stainless steel (radius $r = 1.18$ mm, normal restitution coefficient $e \approx 0.9$) in a high perspex container with a ground surface of 41.5×25.0 mm^2. When the particles are at rest, this corresponds to a filling level of 2.0 layers. The box was divided into $N = 2$ equal compartments by a wall, with a horizontal slit of 25.0 mm by 5.0 mm, starting at height $h = 25.0$ mm, and a hole of dimensions 3.0 mm $\times$ 3.0 mm at the bottom. The entire device was subjected to vertical, sinusoidal vibrations with variable frequency f (ranging from 47 Hz to 150 Hz) and fixed amplitude $a = 1.0$ mm. The results are given in Fig. 7.2 in terms of the dimensionless control parameter

$$B = 4\pi \frac{gh}{a^2 f^2}(1 - e^2)^2 \left(\frac{r^2 P}{\Omega N}\right)^2, \tag{7.1}$$

which is motivated [13] from the kinetic theory for dilute granular gases (see also Eq. (7.2) below). Here Ω ($= 19.7 \times 25.0$ mm^2) is the surface area of each compartment, and $g = 9.81$ m/s^2. As anticipated, *vigorous shaking* (small B) leads to a symmetric steady state, giving way to a clustered state with the predicted fountain effect for *intermediate driving*. For very *weak driving* (large B) the system returns to equipartition via the hole at the bottom of the container, since the flux through

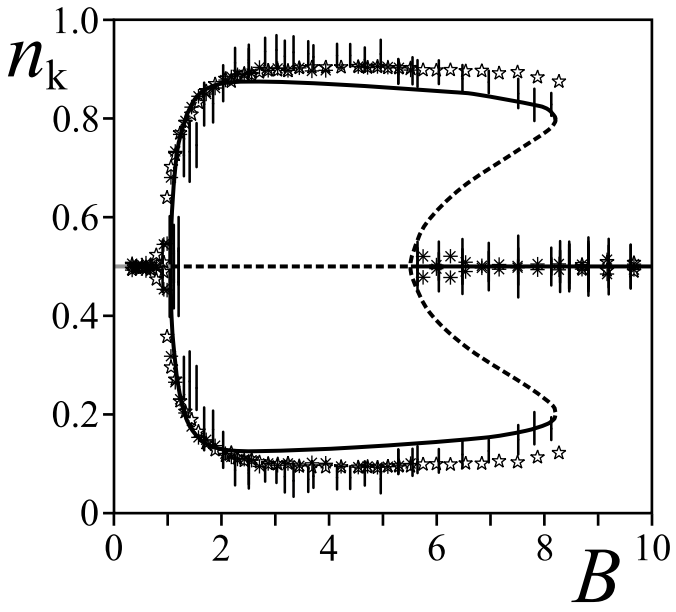

Figure 7.2: Bifurcation diagram for the granular fountain. Depicted are the steady-state fractions of particles n_k, $k \in \{1, 2\}$, in the two compartments from Fig. 7.1a for different values of the driving frequency f in units of $B \propto f^{-2}$ from Eq. (7.1). Experimental results are indicated by the vertical error bars; the other symbols represent molecular dynamics simulations using uniform (asterisks) and clustered (stars) initial conditions. The lines represent the theoretical prediction from the flux model (7.1)-(7.3) for $\lambda = 0.018$: solid lines correspond to stable configurations; dashed lines to unstable ones.

the slit (cf. Fig. 7.1a) becomes negligibly small. Furthermore, a pronounced hysteresis is observed in Fig. 7.2 for B-values between 5.5 and 8.2.

Fig. 7.2 also contains the results of molecular dynamics *simulations* in a setup comparable to the experiment: $K = 2$ rectangular compartments with ground area 19.4×25.0 mm^2 and filled with $P = 400$ particles of radius $r = 1.18$ mm and normal restitution coefficient $e = 0.9$*. While the slit at height h was as in the experiment, the hole at the bottom was chosen slightly larger (4.2×4.2 mm^2) to compensate for the vanishing thickness of the apertures and the neglected dissipation from particle-wall collisions in the simulations. Experiments and simulations are seen to agree well.

*The simulation uses a hard-sphere collision model in which the dissipation is described by 3 parameters: The coefficients of normal restitution, tangential restitution and friction. The latter two were set equal to their ideal (dissipationless) values.

These findings can be explained in the spirit of a previously established *flux model* [13–16] with the help of two flux functions F and G describing the number of particles which escape out of a compartment per time unit through the slit and the hole, respectively:

$$\begin{aligned} F(n_k) &= A\, n_k^2\, e^{-BN^2 n_k^2}, \\ G(n_k) &= A\, \lambda\, n_k^2. \end{aligned} \tag{7.2}$$

Here, B is defined in (7.1), n_k is the fraction of particles in compartment $k \in \{1, ..., N\}$ (hence $n_k \in [0, 1]$, $\Sigma_1^K n_k = 1$), and A essentially accounts for the size of the slit, $[A] = \mathrm{s}^{-1}$. The flux $F(n_k)$ grows from zero for $n_k = 0$ to a maximum at $n_k = (BN^2)^{-1/2}$, and then decreases asymptotically towards zero as a result of the inelastic collisions between the particles. The flux through the hole, $G(n_k)$, is obtained by taking the limit $h \to 0$ of $F(n_k)$. The ratio λ of $G(n_k)$ and $F(n_k)$ in the low density limit is determined by the ratio of the surface areas of the hole and the slit, and also accounts for the anisotropy of the velocity distribution just above the bottom. Obviously, λ should be chosen considerably smaller than unity, otherwise the flux through the hole will completely overpower that through the slit, and hence the clustering effect. For our experimental setup one finds as a rough estimate $\lambda \approx 0.02$ under the assumption that the finite particle radius effectively reduces the dimensions of slit and hole by 1.8 mm and neglecting any velocity anisotropies.

In the fountain geometry ($N = 2$) from Fig. 7.1a the time-evolution of the relative populations $n_1 = n_1(t)$ and $n_2 = 1 - n_1$ follows by adding up all the fluxes through slit and hole:

$$\dot{n}_1 = F(1 - n_1) + G(1 - n_1) - F(n_1) - G(n_1) \tag{7.3}$$

The uniform distribution $n_1 = n_2 = 1/2$ is a stationary solution for all B, but is linearly stable only if the Jacobian $-2F'(1/2) - 2G'(1/2) = -2A[(1 - B)\exp(-B) + \lambda]$ is negative. This is the case when B is either small or large. If $\lambda < e^{-2}$ there exists a B-interval for which the uniform distribution is unstable, and one can show that now the only stable solutions of (7.3) are a symmetric pair of clustered, fountain states. When fitting with $\lambda = 0.018$, the comparison of the predictions of the flux model with the experiment in Fig. 7.2 is fairly good; especially the bifurcation and the hysteresis are well reproduced.

Convection rolls somewhat similar to our present granular fountain but governed by different physical mechanisms are well known for ordinary liquids and gases out of equilibrium and also for granular systems at very high densities. For a dilute granular gas, as we consider it here, convection in a single container has been

reported recently [20–22], but neither a compartmentalized setup nor a theoretical modelling have been addressed before.

7.3 The granular ratchet

We now proceed towards the *"granular ratchet"* setup in Fig. 7.1b: Starting with any number of copies of the granular fountain placed next to each other and closed cyclically, we then move each hole to its adjacent wall. Within the flux model (7.1) - (7.2) this amounts to replacing (7.3) by

$$\begin{aligned} \dot{n}_k &= G(n_{k+1}) + F(n_{k-1}) - F(n_k) - G(n_k), \text{ even } k, \\ \dot{n}_k &= F(n_{k+1}) + G(n_{k-1}) - F(n_k) - G(n_k), \text{ odd } k \end{aligned} \tag{7.4}$$

with an even number of compartments N and periodic boundary conditions $n_{N+k} = n_k$. Due to (7.2) it follows that any periodically continued steady state solution of the original fountain geometry translates into a steady state solution of the extended granular ratchet geometry; the particle currents through the slits remain unchanged, and those through the holes are simply inverted. Less obvious is the stability of these solutions and the possible coexistence of further stable solutions:

In the simplest case of a granular ratchet consisting of just $N = 2$ periodically closed compartments, one obtains, as expected, a bifurcation diagram (not shown) which practically coincides with that in Fig. 7.2, and similarly for the particle currents. Turning to $N = 4$ compartments as depicted in Fig. 7.1b, we have performed molecular dynamics simulations with the same dimensions of compartment, hole, and slit and the same average particle number $P/N = 200$ per compartment as in the $N = 2$ fountain case. The resulting bifurcation diagram in Fig. 7.3 displays as its most prominent new feature *two different types of coexisting stable states* with spontaneously broken symmetry for not too large B-values: (i) *Ratchet states* with alternating dense and dilute compartments and a resulting finite directed particle flux, as quantitatively exemplified in Fig. 7.4: As the system evolves towards its stable steady state, both fluxes in Fig. 7.4 converge to the same constant mean. Its finite value is the most immediate signature of a spontaneous ratchet effect. (ii) *Fluxless clustered states* with alternating pairs of dense and dilute compartments and no resulting net particle flux, see Fig. 7.4. Our experimental data (not shown) on the $N = 4$ ratchet are in agreement with these findings.

The intricate bifurcation diagrams for even larger N will be presented elsewhere. The main (and quite plausible) finding is that current carrying ratchet states with alternating dense and dilute compartments are always stable solutions within

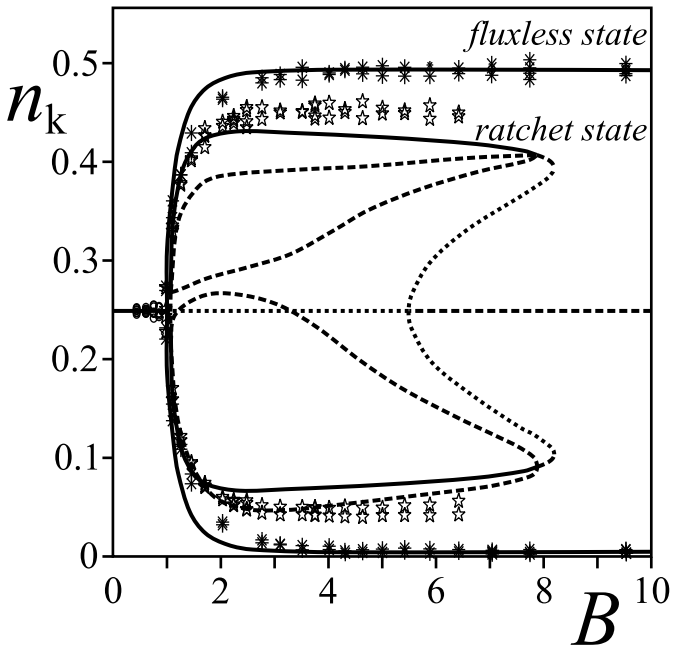

Figure 7.3: Bifurcation diagram of the $N = 4$ granular ratchet. Symbols: results from molecular dynamics simulations. Lines: prediction from the flux model (1), (2), (4) for $\lambda = 0.018$. Solid lines correspond to stable configurations; dashed lines to unstable ones. For further details regarding parameters and methods see main text. For small B the uniform distribution, $n_1 = n_2 = n_3 = n_4 = 1/4$, is the unique steady state. At $B = 1$ a pair of symmetry broken stable states takes over, namely $n_2 = n_3 \neq n_4 = n_1$, indicated by asterisks. They exhibit no net particle flow and are called *fluxless clustered states*. For slightly larger B another pair of stable states emerges, both of the form $n_1 = n_3 \neq n_2 = n_4$ (see Fig. 7.1b), indicated by stars. They do carry a net flow (cf. Fig. 7.4) and are called *ratchet states*. For $B > 6.8$ only the fluxless stable states survive.

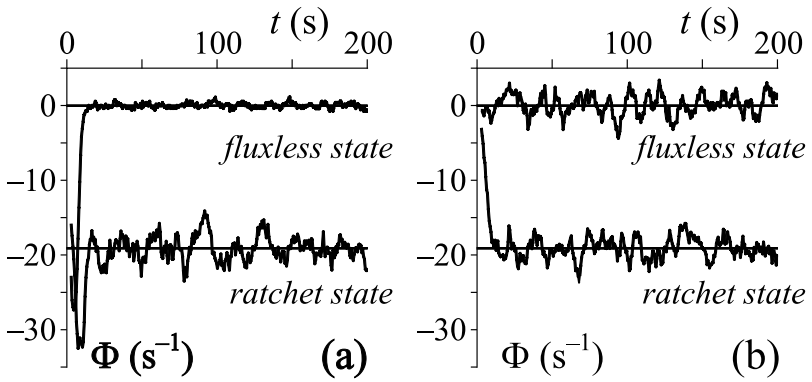

Figure 7.4: Running time average (over 5 seconds) of the net particle flux $\Phi(t)$ for the same molecular dynamics as in Fig. 7.3 with $B = 3.0$, measured through the rightmost slit (a), and through the rightmost hole (b) in Fig. 7.1b. The upper curves in each plot correspond to the clustered state with densely populated leftmost and rightmost compartments in Fig. 7.1b. The lower curves belong to the ratchet state with densely populated compartments 1 and 3 in Fig. 7.1b. For both states the straight line corresponds to the long-time asymptote of the particle current.

an entire interval of B-values. Moreover, one finds an increasing number of coexisting states with spontaneously broken symmetry. These are long-lived hybrid states, containing both ratchet-like regions (with alternating dense and dilute compartments) and fluxless clustered regions.

Which specific steady state solution the system will settle in strongly depends on the initial condition, and at phase boundaries also on random fluctuations. An interesting example of the latter type is a uniform initial distribution. The corresponding probability p_N of ending up in a ratchet state is depicted in Fig. 7.5. For an intuitive explanation we view the system as $N/2$ identical "dimers", each consisting of two compartments with a common slit at height h, and connected with each other by holes. Since the holes which connect neighboring dimers are much smaller than the slits, inside each dimer a quasi-steady distribution is approached much faster than the full equilibration between all dimers. Hence, an initially uniform distribution evolves inside each dimer towards either of two clustered states with probability $q = 1/2$, independently of the other dimers. This implies that a granular ratchet system with N compartments will end in one of the two ratchet states with alternating dense and dilute compartments with probability

$$p_N = 2\, q^{N/2} \,. \tag{7.5}$$

This prediction is in excellent agreement with the linear best fit $p_N = 2.02\,(0.394)^{N/2}$

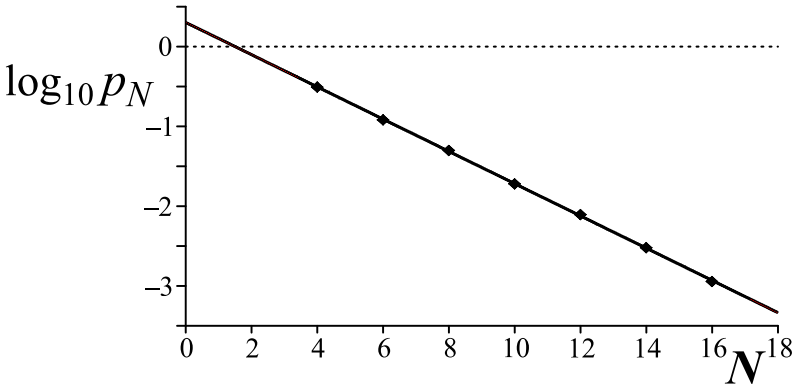

Figure 7.5: Fraction p_N of ratchet solutions versus number $N(\geq 4)$ of compartments in a granular ratchet system with a constant initial particle number P/N per compartment. Symbols represent numerical solutions of the (deterministic) flux model (1), (2), (4) for $B = 3$ and $\lambda = 0.018$, averaged over initial distributions with a superimposed randomization, mimicking fluctuations due to the finite particle number within each compartment. The straight line is a linear best fit.

in Fig. 7.5. The reduced q-value can be attributed to the fact that the dimers are actually not entirely independent due the finite hole size.

In practice, a ratchet state spontaneously arises only with a small probability for large N, as far as uniform initial conditions are concerned. This situation is comparable to other systems with spontaneous symmetry breaking, e.g. a ferromagnet[†]: Just like a piece of iron picked from the shelf normally appears to be "unmagnetized" and an external magnetic field is needed to produce a magnetization on a global scale, a ratchet state only emerges with appreciable probability for large N if there is some initial bias towards this state. Without breaking the symmetry of the setup, this could be realized (in a reproducible direction, if so desired) by applying a periodically modulated initial particle distribution or a small external force in the horizontal direction in Fig. 7.1b, acting during a certain preparatory time span.

In conclusion, we have exploited the clustering effect to create spontaneous directed transport in symmetrically compartmentalized granular gases. In the granular fountain it takes the shape of a convection roll, and in the granular ratchet it appears as a current perpendicular to the vertical driving. In both cases, the directed transport arises as a collective effect of the stochastically colliding particles.

[†]For the analogy, the dimers of the ratchet system should be compared to the single ferromagnetic domains in the piece of ferromagnetic material.

References

[1] H. Linke (guest editor), *Ratchets and Brownian motors: Basics, experiments and applications*, Appl. Phys. A **75**, 167 (2002).

[2] P. Reimann, *Brownian motors: Noisy transport far from equilibrium*, Phys. Rep. **361**, 57 (2002).

[3] F. Jülicher and J. Prost, *Cooperative molecular motors*, Phys. Rev. Lett. **75**, 2618 (1995).

[4] P. Reimann, R. Kawai, C. Van den Broeck, and P. Hänggi, *Coupled Brownian motors: Anomalous hysteresis and zero-bias negative conductance*, Europhys. Lett. **45**, 545 (1999).

[5] A.L.R. Bug and B.J. Berne, *Shaking-induced transition to a nonequilibrium state*, Phys. Rev. Lett. **59**, 948 (1987).

[6] Z. Farkas, P. Tegzes, A. Vukics, and T. Vicsek, *Transitions in the horizontal transport of vertically vibrated granular layers*, Phys. Rev. E **60**, 7022 (1999).

[7] D.C. Rapaport, *Mechanism for granular segregation*, Phys. Rev. E **64**, 061304 (2001).

[8] F.J.C. Rademacher, *On the theoretical and experimental conveying speed of granular bulk solids on vibratory conveyors*, Bulk Solids Handling **15**, 41 (1995).

[9] E.M. Sloot and N.P. Kruyt, *Theoretical and experimental study of the transport of granular materials by inclined vibratory conveyors*, Powder Technology **87**, 203 (1996).

[10] I. Goldhirsch and G. Zanetti, *Clustering instability in dissipative gases*, Phys. Rev. Lett. **70**, 1619 (1993).

[11] H.M. Jaeger, S.R. Nagel, and R.P. Behringer, *Granular solids, liquids, and gases*, Rev. Mod. Phys. **68**, 1259 (1996).

[12] L.P. Kadanoff, *Built upon sand: Theoretical ideas inspired by granular flows*, Rev. Mod. Phys. **71**, 435 (1999).

[13] J. Eggers, *Sand as Maxwell's demon*, Phys. Rev. Lett. **83**, 5322 (1999).

[14] K. van der Weele, D. van der Meer, M. Versluis, and D. Lohse, *Hysteretic clustering in a granular gas*, Europhys. Lett. **53**, 328 (2001).

[15] D. van der Meer, K. van der Weele, and D. Lohse, *Bifurcation diagrams of compartmentalized granular gases*, Phys. Rev. E **63**, 061304 (2001).

[16] D. van der Meer, K. van der Weele, and D. Lohse, *Sudden collapse of a granular cluster*, Phys. Rev. Lett. **88**, 174302 (2002).

[17] J.J. Brey, F. Moreno, R. García-Rojo, and M.J. Ruiz-Montero, *Hydrodynamic Maxwell demon in granular systems*, Phys. Rev. E **65**, 011305 (2002).

[18] A. Lipowski and M. Droz, *Urn model of separation of sand*, Phys. Rev. E **65**, 031307 (2002).

[19] F. Coppex, M. Droz, and A. Lipowski, *Dynamics of the breakdown of granular clusters*, Phys. Rev. E **66**, 011305 (2002).

[20] R. Ramirez, D. Risso, and P. Cordero, *Thermal convection in fluidized granular systems*, Phys. Rev. Lett. **85**, 1230 (2000).

[21] R.D. Wildman, J.M. Huntley, and D.J. Parker, *Convection in highly fluidized three-dimensional granular beds*, Phys. Rev. Lett. **86**, 3304 (2001).

[22] X. He, B. Meerson, and G. Doolen, *Hydrodynamics of thermal granular convection*, Phys. Rev. E **65**, 030301 (2002).

Chapter 8

Temperature Anisotropy in a Driven Granular Gas [‡]

When smooth granular material is fluidized by vertically shaking a container, we find that the temperature in the direction of energy input always exceeds the temperature in the other directions. An analytical model is presented which shows how the anisotropy can be traced back to the inelasticity of the interparticle collisions and the collisions with the wall. The model compares very well with molecular dynamics simulations. It is concluded that any non-isotropic driving of a granular gas in a steady state necessarily causes anisotropy of the granular temperature.

8.1 Introduction

As compared to an ordinary, molecular gas, the hallmark of a granular gas is its permanent dissipation of energy due to inelastic collisions. Whereas an isolated molecular gas will sustain its motion for an infinite amount of time, the only true equilibrium state of granular matter is the one where it is at rest. Hence a steady supply of energy is required to keep a granular gas alive, giving rise to prototypical non-equilibrium systems with many striking phenomena [1, 2]. The one addressed in this chapter is the crucial, but usually ignored temperature anisotropy within a granular gas, fluidized by vertically vibrating a container. It is observed to be a significant effect in both numerical simulations [3] and experiments [4–7], but a theoretical explanation is still lacking.

[‡]Devaraj van der Meer and Peter Reimann, *Temperature Anisotropy in a Driven Granular Gas*, submitted to Phys. Rev. Lett. (2004).

So what causes the anisotropy? We approach this question by a theoretical model in combination with event driven molecular dynamics (MD) simulations, and show that the anisotropy results from the following characteristic feature of such a gas: The *distribution* of energy from the vibrating bottom towards the horizontal directions occurs through the very same mechanism that also constitutes one of the major sources of energy *dissipation*, i.e., the collisions between the particles. This result carries over to any granular gas with a non-isotropic energy source.

The setup we will consider in our present work consists of a granular gas in a container with a square-shaped bottom of side length L in the x-y-plane and infinitely high, vertical side-walls. Gravity acts with $g = 9.81$ m/s^2 and the gas is fluidized by vertical vibrations of the bottom about $z = 0$ with amplitude a and frequency f, typically of triangular (piecewise linear, symmetric) or sinusoidal shape. The gas consists of N identical hard spheres with radius r_p and mass m. We restrict ourselves to the case [3, 8–13] that only normal restitution [1, 2] contributes to the dissipative processes, with restitution coefficients e_p for particle-particle and e_w for particle-wall collisions, while collisions with the vibrating bottom are taken to be perfectly elastic.

After initial transients have died out, we expect (and observe) a stationary probability distribution $\rho(\boldsymbol{r}, \boldsymbol{v})$ of the particle positions $\boldsymbol{r} := (x, y, z)$ and velocities $\boldsymbol{v} := (v_x, v_y, v_z)$. The quantities of central interest are the temperature components

$$T_i(z) := \frac{m}{k} \langle v_i^2 \rangle \tag{8.1}$$

where $i \in \{x, y, z\}$ and k is Boltzmann's constant. This $T_i(z)$ is directly proportional to the average kinetic energy of the particles in a horizontal layer at height z in either of the three spatial directions i.

In evaluating our MD simulations we replace ensemble averages in (8.1) by time averages (justified by ergodicity) and work in units with $m = 1$ and $k = 1$. A representative result is depicted in Fig. 8.1: As expected for symmetry reasons, the horizontal temperature components $T_x(z)$ and $T_y(z)$ are practically indistinguishable. In contrast, the vertical temperature component $T_z(z)$ is significantly larger than $T_x(z)$ and $T_y(z)$. For perfectly elastic particle-wall collisions (Fig. 8.1a) the z-dependence of the temperature components is very weak except for a region directly above the bottom. There, the energy-input by the driving leads to increased upward particle velocities, as shown by the dashed lines in (Fig. 8.1a). For inelastic particle-wall collisions (Fig. 8.1b) the z-dependence of the temperature components is more pronounced. Yet, in both cases the differences between vertical and horizontal temperatures are more important than the z-dependences.

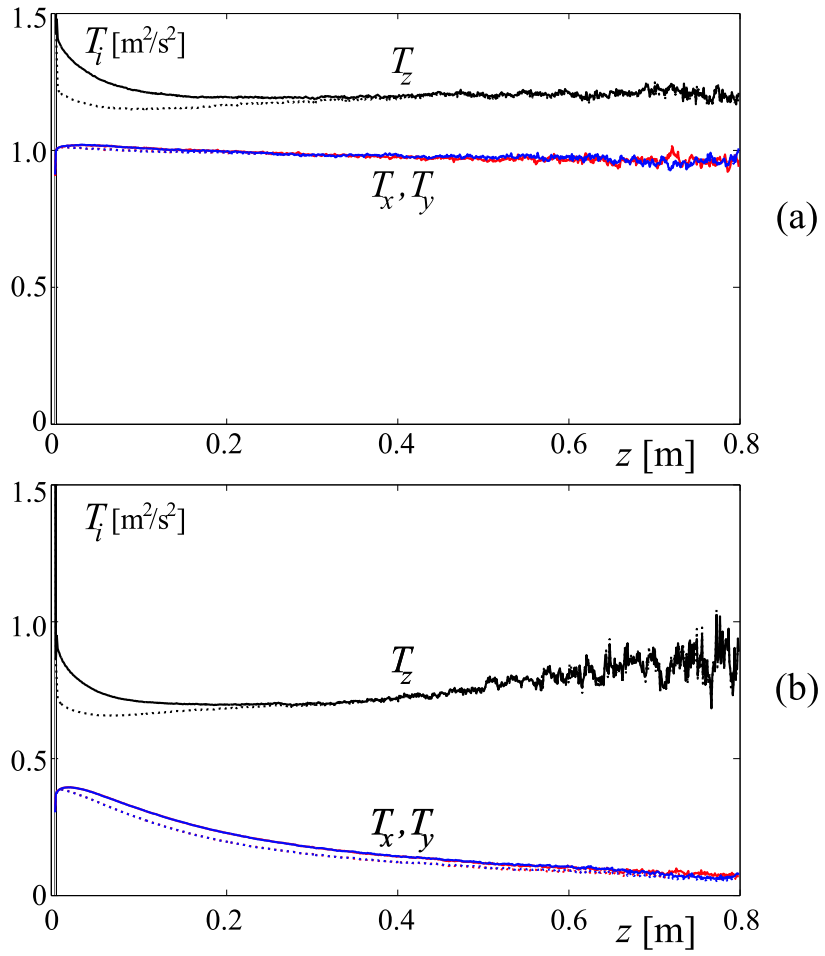

Figure 8.1: Solid lines: Temperature components (8.1) from MD simulations of the driven granular gas model as specified in the main text with sinusoidal driving and parameters $f = 72.648$ Hz, $a = 1.00$ mm, $N = 50$, $r_p = 1.18$ mm, and $L = 2.265$ cm. (a): $e_p = 0.9$ and $e_w = 1$ (reflective sidewalls). (b): $e_p = 0.95$ and $e_w = 95$ (dissipative sidewalls). Dashed lines: Counting only particles that move downward, i.e. restricting the average in (8.1) to negative v_z-values. At large z the statistics deteriorates since particles rarely reach such heights. The curves $T_x(z)$ and $T_y(z)$ practically coincide.

8.2 A theoretical two-temperature model

Our theoretical analysis of the observed temperature differences starts with the well-known conservation laws of energy and momentum for a dilute granular gas, derived from Boltzmann's equation [8–10]. For a stationary system, they read, in terms of the local heat flux $\mathbf{J}(\boldsymbol{r})$ and stress (or pressure) tensor $\mathbf{P}(\boldsymbol{r})$:

$$\nabla \cdot \mathbf{J}(\boldsymbol{r}) = I(\boldsymbol{r}) \ , \ \ \nabla \cdot \mathbf{P}(\boldsymbol{r}) = n(\boldsymbol{r})\mathbf{f}(\boldsymbol{r}) \ . \tag{8.2}$$

Here, $I(\boldsymbol{r})$ is the local energy dissipation rate per unit volume, $n(\boldsymbol{r})$ is the local particle density, and the force $\mathbf{f}(\boldsymbol{r}) = -mg\mathbf{e}_z$. Integrating the first equation (8.2) over the container volume V we obtain with Gauss' theorem that the energy dissipation rate due to particle-particle collisions $Q_{pp} := \int_V I(\boldsymbol{r})\, d\mathbf{r}$ must be equal to the total flux of energy through the boundaries. The latter can be decomposed in the influx $Q_{in} := L^2\, J_z(0)$ of energy through the vibrating bottom of area L^2 and the energy dissipation rate Q_w due to particle-wall collisions. This gives

$$Q_{in} = Q_{pp} + Q_w. \tag{8.3}$$

Crucial to the present model is that the temperature components T_i defined in (8.1) are treated separately. To our knowledge, all existing theories for driven granular gases in a steady state without net flow of material are based upon the assumption of an isotropic temperature, and many of them also on isotropic stress [8–11]*.

The temperature components T_i are related to the diagonal elements of the stress tensor by a generalized ideal gas law $P_{ii} = nkT_i$ [8–10]. Motivated by our MD simulations, we assume that each temperature component T_i is approximately constant within the entire container volume (see also [12, 17]). Because of symmetry the stress tensor is diagonal and $T_x = T_y =: T_{hor}$, with which the second equation (8.2) can now be readily integrated to yield

$$n(\boldsymbol{r}) = \frac{Nmg}{L^2 k T_z} \exp\left\{-\frac{mgz}{kT_z}\right\} \ . \tag{8.4}$$

Furthermore, as exemplified by Fig. 8.2, our MD simulations show that the particle velocity components can be assumed as Gaussian distributed in very good approximation for a wide range of parameter values [18]†. All together, we thus arrive at

*Only in the context of the normal-stress differences observed in steady plane Couette flow of granular material [14], an anisotropic stress tensor [15] or Maxwell-Boltzmann velocity distribution [16] has been used.

†In [19, 20], large deviations from Gaussian velocity distributions, especially near the vibrating bottom, have been reported. Our simulations show that they are rooted in the *discontinuous*, saw-tooth shape of the vibrations considered in [19, 20]. This is the main reason that we focus on *continuous* shapes of the driving in the present work.

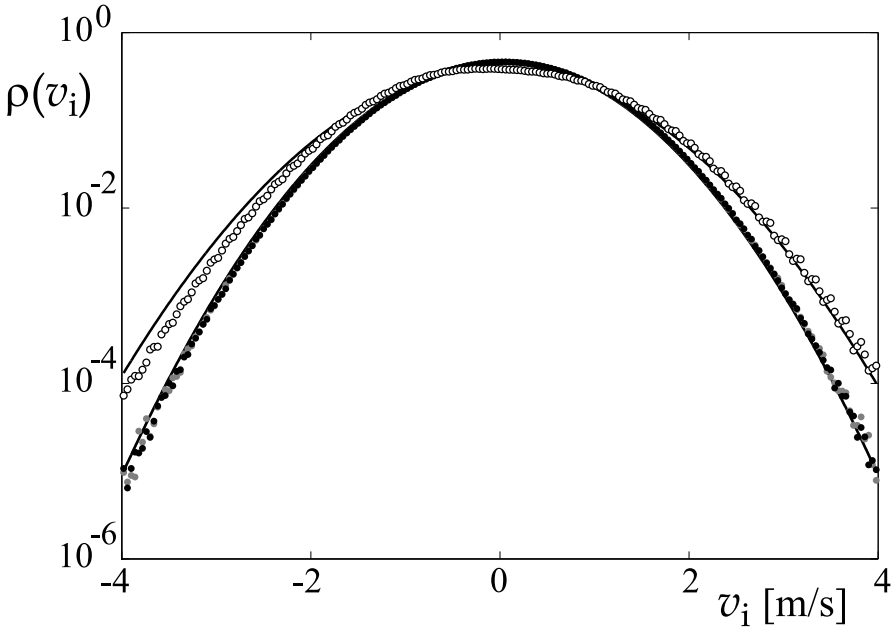

Figure 8.2: Horizontal (solid grey and black dots) and vertical (open dots) velocity distributions of particles in a layer between $z = 0$ and $z = 5$ mm obtained by MD simulations for the same system as in Fig. 8.1a but with $f = 30$ Hz and $L = 4.8$ cm. The solid lines are Gaussian fits.

the following approximative distribution function for particle position and velocity:

$$\rho(\boldsymbol{r}, \boldsymbol{v}) = \frac{n(\boldsymbol{r})\, m^{3/2}}{\sqrt{(2\pi k)^3 T_{hor}^2 T_z}} \exp\left\{ -\frac{m(v_x^2 + x_y^2)}{2kT_{hor}} - \frac{mv_z^2}{2kT_z} \right\} . \tag{8.5}$$

The next main idea is to determine the two unknowns T_z and T_{hor} in (8.5) by means of two energy balance relations. The first of them is (8.3). To obtain the second, we observe that particle-particle collisions not only cause energy dissipation but also a transfer of kinetic energy from the horizontal direction into the vertical direction, and vice versa. In the steady state the net effect must be an average loss of kinetic energy per time unit Q_z in the vertical direction which is exactly balanced by the incoming energy flux Q_{in} through the vibrating bottom:

$$Q_{in} = Q_z . \tag{8.6}$$

The remaining, rather technical task is to explicitly determine all the energy fluxes Q appearing in (8.3) and (8.6) with the help of the approximation (8.5). In

order to evaluate Q_z, we first note that the change of kinetic energy in the vertical direction in a single particle-particle collision is

$$q_z = \sum_{j=1}^{2} \frac{m}{2} \left((\boldsymbol{v}_j \cdot \boldsymbol{e}_z)^2 - (\boldsymbol{v}_j^* \cdot \boldsymbol{e}_z)^2 \right) \ , \tag{8.7}$$

where $\boldsymbol{v}_j$ and $\boldsymbol{v}_j^*$ are the velocities of the two colliding particles ($j = 1, 2$) before and after the collision, respectively. Due to our assumption that only normal restitution contributes to the dissipative processes, we have $\boldsymbol{v}_j^* = \boldsymbol{v}_j + (-1)^j(1 + e_p)[(\boldsymbol{v}_1 - \boldsymbol{v}_2) \cdot \boldsymbol{n}]\boldsymbol{n}/2$, where $\boldsymbol{n}$ is the collision normal vector. To determine Q_z one essentially has to introduce this result for $\boldsymbol{v}_j^*$ into (8.7) and then average according to (8.5). More precisely, first q_z in (8.7) is multiplied by the collisional volume per unit time $(1/2)\pi(2r_p)^2|\boldsymbol{v}_2 - \boldsymbol{v}_1|\delta(|\boldsymbol{r}_1 - \boldsymbol{r}_2| - 2r_p)$, where the factor $1/2$ arises since collisions only can happen if $(\boldsymbol{v}_2 - \boldsymbol{v}_1) \cdot \boldsymbol{n} < 0$. Next we multiply with $(1/2)\rho(\boldsymbol{r}_1, \boldsymbol{v}_1)\rho(\boldsymbol{r}_2, \boldsymbol{v}_2)$ according to (8.5) and integrate over all $\boldsymbol{v}_j$ and $\boldsymbol{r}_j$ (within the container volume). The factor $1/2$ is needed since every collision appears twice in the above considerations. This gives, after a substantial amount of algebra:

$$\begin{aligned} Q_z &= (1 + e_p)\,(Nr_p/L)^2 g\sqrt{\pi m k T_z}\, F(T_{hor}/T_z) \\ F(\vartheta) &:= \int_0^\infty ds \int_0^\infty dt\, \sqrt{s+t}\, \frac{(8 - 4e_p)s - (1 + e_p)t}{6\,\vartheta\sqrt{s}\, \exp\{s + t/\vartheta\}} \ . \end{aligned} \tag{8.8}$$

A similar averaging of the total energy loss in a single particle-particle collision $q_{pp} = (m/2)\sum_{j=1}^{2}(\boldsymbol{v}_j^2 - (\boldsymbol{v}_j^*)^2)$ yields

$$\begin{aligned} Q_{pp} &= (1 - e_p^2)\,(Nr_p/L)^2 g\sqrt{\pi m k T_z}\, G(T_{hor}/T_z) \\ G(\vartheta) &:= \int_0^\infty ds \int_0^\infty dt\, \frac{[s+t]^{3/2}}{\vartheta\sqrt{s}\, \exp\{s + t/\vartheta\}} \ . \end{aligned} \tag{8.9}$$

In the same spirit one can evaluate the total dissipation rate due to particle-wall collisions Q_w with the result

$$Q_w = 4\,(1 - e_w^2)\,N\,(kT_{hor})^{3/2}/(L\sqrt{2\pi m}) \tag{8.10}$$

Finally, a somewhat lengthy but straightforward calculation yields the following expression for the energy input rate at the perfectly elastic, vibrating bottom of the container:

$$Q_{in} = 2\,N\,g\,m^{3/2}\,u^2\psi(\gamma)/\sqrt{\pi k T_z} \tag{8.11}$$

where $\gamma := \sqrt{2kT_z/mu^2}$, $u =: \pi\sqrt{2}\,af$ for sinusoidal driving of the bottom, and $u := 4\,af$ for triangular driving. In both cases, for large γ (which is the typical situation in the dilute systems under study) the function $\psi(\gamma)$ approaches unity [‡].

In the absence of wall dissipation ($e_w = 1$), Eqs. (8.3), (8.6), (8.8)-(8.11) imply

$$F(T_{hor}/T_z) = (1 - e_p)G(T_{hor}/T_z)\ , \quad [e_w = 1]\ . \tag{8.12}$$

Closer inspection shows that for any $0 \leq e_p < 1$ a unique solution $0 \leq T_{hor}/T_z < 1$ of (8.12) exists. In particular, for small $1 - e_p$ one finds the leading order asymptotics

$$T_{hor}/T_z = 1 - (5/2)\,(1 - e_p)\ , \quad [e_w = 1]\ . \tag{8.13}$$

Thus for $e_p < 1$ and perfectly reflecting walls, the model predicts that the horizontal temperature T_{hor} is *always* smaller than the vertical temperature T_z. Moreover, the ratio T_{hor}/T_z solely depends on e_p but not on any details of driving shape and strength, particle density, particle size, or compartment geometry. The comparison with MD simulations in Fig. 8.3 is excellent. The inset of Fig. 8.3 shows that the remaining deviations can largely be attributed to finite size effects.

In the general case one obtains two transcendental, algebraic equations for the two unknowns T_{hor} and T_z by introducing (8.8)-(8.11) into (8.3) and (8.6). While existence and uniqueness of solutions can still be demonstrated analytically, their quantitative determination is only possible numerically. An example is depicted in Fig. 8.4, comparing very well with MD simulations. As expected, dissipative walls tend to reduce the horizontal temperature T_{hor} since they add a source of dissipation for the horizontal kinetic energy. If we increase the particle number, the gas becomes more dense, and the number of particle-particle collisions will increase much faster than the number of particle-wall collisions. Therefore, T_{hor} will first *increase*, in sharp contrast to the overall temperature $[T_z + 2T_{hor}]/3$ which must decrease with increasing particle density. Eventually, particle-particle collisions will dominate the system, and T_{hor}/T_z will asymptotically tend to the value it would have with reflecting walls.

In conclusion, we have numerically observed large differences between the vertical and horizontal temperatures in vertically driven granular gases subjected to gravity. We introduced a theoretical model based on an approximative Maxwell-Boltzmann distribution with anisotropic but homogeneous temperature (8.5), justified by our MD simulations. Both for reflecting and dissipative walls of the container we find that the theoretical model gives good quantitative agreement with the simulations.

[‡]For triangular driving we have derived the exact result $\psi(\gamma) = (1/4)[2 + 3\exp(-1/\gamma^2) - 6\exp(-4/\gamma^2) + 3\exp(-9/\gamma^2)] + (\sqrt{\pi}/8\gamma)[(6 + 3\gamma^2)\,\mathrm{erf}(1/\gamma) - (24 + 2\gamma^2)\,\mathrm{erf}(2/\gamma) + (18 + \gamma^2)\,\mathrm{erf}(3/\gamma)]$. For sinusoidal driving we were only able to show that $\psi(\gamma) \to 1$ for $\gamma \to \infty$.

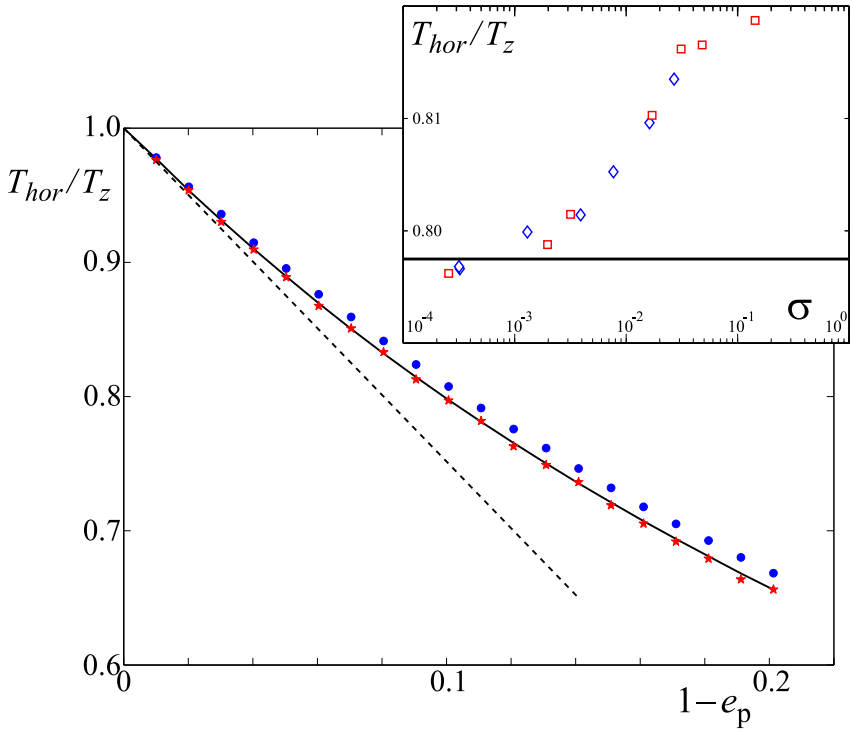

Figure 8.3: Ratio of horizontal and vertical temperatures versus particle-particle restitution coeffi cient. Solid line: Theoretical prediction (8.12). Dashed line: Theoretical asymptotic behavior (8.13). Symbols: MD simulations for the same system as in Fig. 8.1a with $N = 20$ (⋆) and $N = 50$ (•) particles. For $e_p \neq 0.9$, a different choice for the frequency f such that the T_z was (approximately) the same for all e_p. Inset: Same, but for fi xed $e_p = 0.9$ and variable local solid fraction $\sigma := (4/3)\pi r_p^3 \max[n(\mathbf{r})]$, either by varying particle number N (◇, at $r = 1.18$ mm) or radius r_p (□, at $N = 50$).

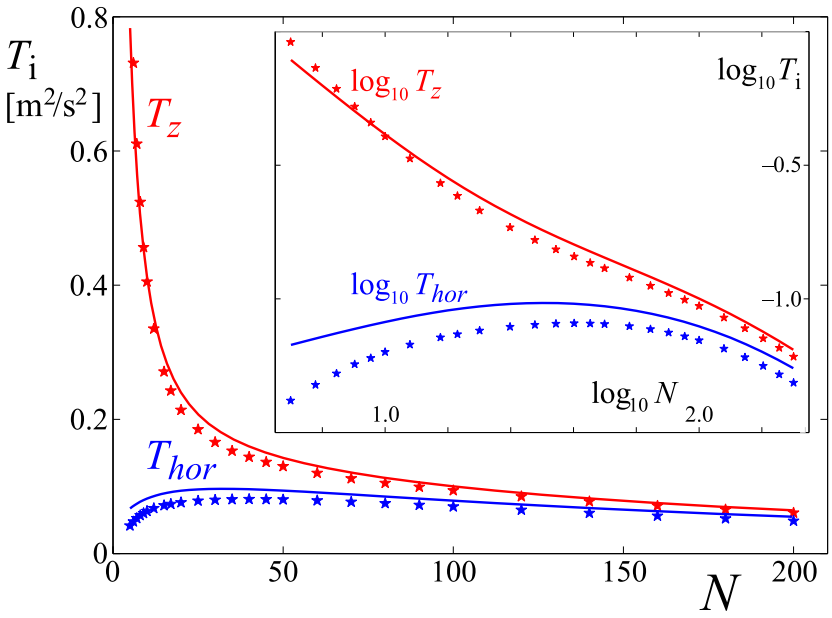

Figure 8.4: Horizontal (T_{hor}) and vertical (T_z) temperatures versus particle number. Lines: Theoretical predictions from (8.3), (8.6), (8.8)-(8.11) for triangular driving and parameters $f = 30$ Hz, $a = 1.00$ mm, $r_p = 1.18$ mm, $L = 4.8$ cm, $e_p = 0.95$ and $e_w = 95$. Symbols: MD simulations. Inset: Same data in a log-log plot.

The difference of the horizontal and vertical temperatures from the isotropic value is a significant correction, at least of the same order as those resulting from taking into account the non-constancy of the temperature and density profiles, or from embedding Chapman-Enskog corrections to the velocity distributions into the theoretical framework [8, 9].

At the root of the temperature anisotropy lies the fact that the *transfer* of kinetic energy between different spatial directions and its *dissipation* arise out of the same mechanism: the collisions between the particles. Thus, the anisotropy of the temperature is a *necessary* consequence of the anisotropy of the driving. The present work indicates that one may obtain an improved hydrodynamic description for dilute granular gases by starting out from an anisotropic velocity distribution (instead of an isotropic one) in deriving hydrodynamics equations from Boltzmann's equation.

The basic concept of the model applies to any situation in which the energy-input in a granular gas is anisotropic, always predicting a higher kinetic energy content in the main direction of energy-input.

References

[1] I. Goldhirsch, *Rapid granular flows*, Annu. Rev. Fluid Mech. **35**, 267 (2003).

[2] K. van der Weele, R. Mikkelsen, D. van der Meer, and D. Lohse, *Cluster formation in compartmentalized granular gases*, in *The Physics of Granular Media*, edited by D. Wolf and H. Hinrichsen, vol. in press (Wiley-VCH, 2004).

[3] S. McNamara and S. Luding, *Energy flows in vibrated granular media*, Phys. Rev. E **58**, 813 (1998).

[4] R.D. Wildman and J.M. Huntley, *Novel method for measurement of granular temperature distributions in two-dimensional vibro-fluidised beds*, Powder Technology **113**, 14 (2000).

[5] X. Yang, C. Huan, D. Candela, R.W. Mair, and R.L. Walsworth, *Measurements of grain motion in a dense, three-dimensional granular fluid*, Phys. Rev. Lett. **88**, 044301 (2002).

[6] D.L. Blair and A. Kudrolli, *Velocity correlations in dense granular gases*, Phys. Rev. E **64**, 050301 (2001).

[7] D.L. Blair and A. Kudrolli, *Collision statistics of driven granular materials*, Phys. Rev. E **67**, 041301 (2003).

[8] N. Sela and I. Goldhirsch, *Hydrodynamic equations for rapid flows of smooth inelastic spheres, to Burnett order*, J. Fluid Mech. **361**, 41 (1998).

[9] J.J. Brey, J.W. Dufty, C.S. Kim, and A. Santos, *Hydrodynamics for granular flow at low density*, Phys. Rev. E **58**, 4638 (1998).

[10] A. Baldassarri, U. Marini Bettolo Marconi, A. Puglisi, and A. Vulpiani, *Driven granular gases with gravity*, Phys. Rev. E **64**, 011301 (2001).

[11] J.J. Brey, J. Ruiz-Montero, and F. Moreno, *Hydrodynamics of an open vibrated granular system*, Phys. Rev. E **63**, 061305 (2001).

[12] J. Eggers, *Sand as Maxwell's demon*, Phys. Rev. Lett. **83**, 5322 (1999).

[13] R. Soto, M. Mareschal, and D. Risso, *Departure from Fourier's law for fluidized granular media*, Phys. Rev. Lett. **83**, 5003 (1999).

[14] C.S. Campbell and A. Gong, *The stress tensor in a two-dimensional granular shear flow*, J. Fluid Mech. **164**, 107 (1986).

[15] I. Goldhirsch and N. Sela, *Origin of normal stress differences in rapid granular flows*, Phys. Rev. E **54**, 4458 (1996).

[16] J.T. Jenkins and M.W. Richman, *Plane simple shear of smooth inelastic circular disks: The anisotropy of the second moment in the dilute and dense limits*, J. Fluid Mech. **192**, 313 (1988).

[17] V. Kumaran, *Temperature of a granular material 'fluidized' by external vibrations*, Phys. Rev. E **57**, 5660 (1998).

[18] J.S. Olafsen and J.S. Urbach, *Velocity distributions and density fluctuations in a granular gas*, Phys. Rev. E **60**, R2468 (1999).

[19] J.J. Brey, J. Ruiz-Montero, and F. Moreno, *Boundary conditions and normal state for a vibrated granular fluid*, Phys. Rev. E **62**, 5339 (2000).

[20] V. Kumaran, *Nonequilibrium stationary states of a particle in a gravitational field driven by a vibrating surface*, Phys. Rev. Lett. **82**, 3248 (1999).

Chapter 9

Conclusions and outlook

We have extensively explored the physics of compartmentalized granular gases and found them to be exemplary in many ways:

- The compartmentalized granular gas is a prime example of a system far from equilibrium in which spontaneous symmetry breaking (clustering) occurs as a collective effect of many interacting particles.
- It is not only a clear-cut paradigm of the clustering effect in a granular gas, but also of a system in which macroscopic quantities, such as temperature and particle density, can differ to an arbitrary extent over the small thickness of the wall between the compartments. This allows for the description in terms of a flux model, and as such is a beautiful experimental realization of the urn-model concept known from statistical mechanics.
- Compartmentalized granular gases display a range of phenomena that play a central role in contemporary non-equilibrium physics: coarsening, jamming, anomalous diffusion and directed transport from a noisy environment, to name a few. Notably, here they are all combined into a single system.
- The system is accessible using all of the three tools available to a physicist: we performed laboratory experiments, compared them to (molecular dynamics) simulations, and theoretically analyzed them (using the flux model).

The findings described in this thesis can be summarized as follows:

The first is the intricate structure of the bifurcation diagrams of compartmentalized granular gases which is unravelled in Chapters 2 and 3. Here it is shown that the clustering transition is of first order for all but the previously studied two-compartment system, where it is of second order. Hence hysteresis is the rule.

We constructed bifurcation diagrams for arbitrary number of compartments and analyzed their stability.

The second main finding is on the lifetime and sudden collapse of a granular cluster (Chapters 4 and 5). It has been shown that even if the energy input rate is large enough to break up a cluster, the cluster will, due to the dissipation, resist its breakup for a long time. As a result, in order to get rid of a granular cluster, supplying surplus energy in a short period of time is more effective than to smearing it out over a long period.*

The third main finding is on the coarsening process within compartmentalized granular gases (Chapter 6), which is fully analyzed within the flux model. The process turns out to be anomalously slow, with the average cluster size growing as $[\log(t)]^{1/2}$.

The fourth main finding is on the granular ratchet effect (Chapter 7), which is (to our knowledge) the first experimental realization of a collective ratchet effect as a result of spontaneous ergodicity breaking in a geometrically completely symmetric setup, as had been predicted theoretically in the late nineties.

The fifth main result is the anisotropy of the temperature in a vertically driven granular gas (Chapter 8), which has been observed before but has never been directly related to the mechanism of the collisions: If energy needs to be distributed from the direction of energy input into the other spatial directions, this can only be done with an efficiency equal to one if no energy is lost in the collisions. As soon as the collisions are dissipative, this is not possible anymore, resulting in a lower granular temperature in the directions perpendicular to the driving.

All phenomena have been studied analytically, the first four by the use of the flux model and the last within the framework of hydrodynamic/kinetic theory, giving very good quantitative agreement with the experiments and molecular dynamics simulations.

Many modifications and generalizations of the compartmentalized systems are conceivable.

Inspired by the paper of Eggers [1], and in addition to the papers which together form this thesis, a fair amount of research on compartmentalized granular gases has been published during the past four years, predominantly on the theoretical and numerical side. They are reviewed by us in ref. [2]. Brey *et al.* [3, 4] constructed a

*It is illustrative, and in accordance with these findings, that an old and proven method to resolve jams (clusters due to the arching effect) in industrial hoppers, consists of hitting the hopper with a sledgehammer, at full power!

"hydrodynamic Maxwell demon" in a two-compartment system without gravity, in which clustering is predicted using a hydrodynamic model. Lipowski, Droz, and Coppex [5, 6] proposed an analysis of the clustering effect in terms of a modified Ehrenfest urn model, and confirmed the hysteresis and sudden collapse phenomena. Bidisperse mixtures of large and small beads have been studied in our group, where Mikkelsen *et al.* [7, 8] found a "competitive clustering effect" (in which, from an asymmetric initial distribution over the two compartments, the clustering could be directed into either one simply by changing the shaking strength), and later also by Barrat and Trizac [9], who considered a bidisperse extension of the hydrodynamic Maxwell demon of Brey and co-workers. Cecconi *et al.* [10] discussed the essential features of the clustering effect in terms of a Kramers-type escape problem, featuring two particles in a double-well potential. Very recently, Marconi *et al.* studied a compartmentalized granular gas driven internally by coupling the dissipative grains to a heat bath [11, 12]. The attention given to compartmentalized granular gases also stimulated a multi-urn extension of the Ehrenfest urn model [13].

The geometry of the system can be changed in many ways. Next to the modifications leading to the granular fountain and ratchet (Chapter 7), we have considered the following extensions: (i) We have constructed a staircase setup, a tilted array of compartments in which we have a competition between clustering and running patterns. In the limit of strong tilting we have observed Burgers-type shock waves, in agreement with the fact that the flux model transforms to a discrete version of the inviscid Burgers equation in that limit. (ii) We have also extended the system to a two-dimensional array of compartments, giving rise to, e.g. many contributing paths for cluster-to-cluster transport in a coarsening system, leading to a path-integral-like formulation of this coarsening stage.

From a mathematical point of view, the flux model is remarkable in its own right. The balance equation looks like one of the known discretizations of partial differential equations as a (nonlinear) diffusion or heat equation, the porous media equation, or the Kardar-Parisi-Zhang equation. The fact however, that one value for the flux $F(n)$ corresponds to two values of the density n means that there are as many possible discontinuities as there are steps ("compartments"), corresponding to even more solutions of a typical problem under consideration. When taking the continuum limit, both the number of possible discontinuities and the number of solutions to a given problem diverge, rendering any problem based on the continuum limit of the flux model, regardless of the boundary conditions, mathematically ill-posed [14].

Within the bifurcation diagrams of the N-compartment system (Chapters 2 and 3) there is a close analogy of the N-state Potts model, i.e., an assembly of P

connected spins with N possible orientations per spin. Also in the Potts model one finds a phase transition of second order if $N = 2$ (the Ising case) and a transition of first order if $N \geq 3$ [6, 15].

Models very similar to the flux model have been used in describing the time-evolution of shear-bands in sheared granular-matter [14], and in the description of sand-ripples formed by a periodic flow [16, 17]. The latter example features a "robber" function, describing the amount of material taken from one ripple and deposited on the next in each half-period of the flow.

The success of the two-temperature model in describing a vertically driven granular gas (Chapter 8) seems to imply that, because of the intrinsic anisotropy of the temperature, a single equation for energy conservation will not be sufficient to describe a dissipative gas. Conservation equations need to be considered for each of the three diagonal components of the stress (pressure) tensor, and possibly even for the three off-diagonal components.

Although the research presented here is predominantly of a fundamental nature, it is potentially important for practical applications: First of all, an understanding of the basic mechanisms of clustering can help in developing strategies and devices to avoid clusters in industry, where they are usually unwanted. Moreover, the compartmentalized setup has a counterpart (on a much larger scale) in connected fluidized beds, which are used, e.g., in the production of fertilizers. In this light it is interesting to study the behavior of compartmentalized systems driven by gas-influx instead of shaking: What are the key differences between gas-fluidized and vibro-fluidized compartmentalized granular gases? A next challenge in this context will be to understand the behavior of granular matter in a compartmentalized system without neglecting interstitial air. To this end the availability of larger simulations, combining molecular dynamics simulations of many particles with computational fluid dynamics code [18–20] is of key importance.

A strong candidate for the practical application of the flux model is traffic flow, in which the dissipative interaction is formed by drivers ceaselessly needing to adjust their speed to the cars in front of them. As is well-known to any frequent freeway driver, having spent significant amounts of time in traffic-jams, also this system tends to cluster. A considerable effort has been devoted to construct macroscopic continuum models on the one hand and microscopic cellular automata models, in which cars are treated individually, on the other [21, 22]. However, the mesoscopic picture, in which highways are divided into cells with a length of about 500 meters (which coincides with the traffic monitoring system) and the flow from one cell into the next is considered, has till now remained underexposed. The flux model has the potential of accurately describing traffic flow without the tremendous overhead of describing each car individually [23]. This again shows the strength

and universality of the presented approach to compartmentalized systems.

References

[1] J. Eggers, *Sand as Maxwell's demon*, Phys. Rev. Lett. **83**, 5322 (1999).

[2] K. van der Weele, R. Mikkelsen, D. van der Meer, and D. Lohse, *Cluster formation in compartmentalized granular gases*, in *The Physics of Granular Media*, edited by D. Wolf and H. Hinrichsen (Wiley-VCH, to appear in 2004).

[3] J.J. Brey, F. Moreno, R. García-Rojo, and M.J. Ruiz-Montero, *Hydrodynamic Maxwell demon in granular systems*, Phys. Rev. E **65**, 011305 (2002).

[4] J.J. Brey, J. Ruiz-Montero, and F. Moreno, *Boundary conditions and normal state for a vibrated granular fluid*, Phys. Rev. E **62**, 5339 (2000).

[5] A. Lipowski and M. Droz, *Urn model of separation of sand*, Phys. Rev. E **65**, 031307 (2002).

[6] F. Coppex, M. Droz, and A. Lipowski, *Dynamics of the breakdown of granular clusters*, Phys. Rev. E **66**, 011305 (2002).

[7] R. Mikkelsen, D. van der Meer, K. van der Weele, and D. Lohse, *Competitive clustering in a bidisperse granular gas*, Phys. Rev. Lett. **89**, 214301 (2002). See also: R. Mikkelsen, D. van der Meer, K. van der Weele, M. Versluis, and D. Lohse, *Competitive clustering in a granular gas*, Phys. Fluids **15**, S8 (2003).

[8] R. Mikkelsen, D. van der Meer, K. van der Weele, and D. Lohse, *Competitive clustering in a bidisperse granular gas: Experiment, molecular dynamics, and flux model*, preprint (2003).

[9] A. Barrat and E. Trizac, *A molecular dynamics 'Maxwell demon' experiment for granular mixtures*, Molecular Physics **101**, 1713 (2003).

[10] F. Cecconi, A. Puglisi, U. Marini Bettolo Marconi, and A. Vulpiani, *Noise activated granular dynamics*, Phys. Rev. Lett. **90**, 064301 (2003).

[11] U. Marini Bettolo Marconi and A. Puglisi, *Statistical mechanics of granular gases in compartmentalized systems*, Phys. Rev. E **68**, 031306 (2003).

[12] U. Marini Bettolo Marconi and M. Conti, *Dynamics of vibrofluidized granular gases in periodic structures*, Phys. Rev. E **69**, 011302 (2004).

[13] Yee-Mou Kao and Pi-Gang Luan, *Poincaré cycle of a multibox Ehrenfest urn model with directed transport*, Phys. Rev. E **67**, 031101 (2003).

[14] T.P. Witelski, D.G. Schaeffer, and M. Shearer, *A discrete model for an ill-posed non-linear parabolic PDE*, Physica D **160**, 189 (2001).

[15] F.Y. Wu, *The Potts model*, Rev. Mod. Phys. **54**, 235 (1982).

[16] J.L. Hansen, M. van Hecke, A. Haaning, C. Ellegaard, K.H. Andersen, T. Bohr, and T. Sams, *Instabilities in sand ripples*, Nature **410**, 324 (2001).

[17] J.L. Hansen, M. van Hecke, C. Ellegaard, K.H. Andersen, T. Bohr, A. Haaning, and T. Sams, *Stability balloon for two-dimensional vortex ripple patterns*, Phys. Rev. Lett. **87**, 204301 (2001).

[18] B.P.B. Hoomans, J.A.M. Kuipers, W.J. Briels, and W.P.M. van Swaaij, *Discrete particle simulation of bubble and slug formation in a two-dimensional gas-fluidised bed: A hard-sphere approach*, Chem. Eng. Sci. **51**, 99 (1996).

[19] B.P.B. Hoomans, J.A.M. Kuipers, and W.P.M. van Swaaij, *Granular dynamics simulation of segregation phenomena in bubbling gas-fluidised beds*, Powder Technology **109**, 41 (2000).

[20] M. Goldschmidt, *Hydrodynamic Modelling of Fluidised Bed Spray Granulation*, Ph.D. thesis, University of Twente (2001).

[21] D. Helbing, *Traffic and related self-driven many-particle systems*, Rev. Mod. Phys. **73**, 1067 (2001).

[22] D. Chowdhury, L. Santen, and A. Schadschneider, *Statistical physics of vehicular traffic and some related systems*, Phys. Rep. **329**, 199 (2000).

[23] K. van der Weele, W. Spit, T. Mekkes, and D. van der Meer, *From granular flux models to traffic flow description*, in *Traffic and Granular Flow*, edited by S. Luding and D. Wolf (to appear in 2004).

Summary

Small beads are put in a transparent container divided into two parts by a wall. When the container is shaken vigorously, the beads move fiercely, now and then colliding with the wall and the other particles. They form a granular gas, and distribute themselves evenly over the two compartments, much like an ordinary molecular gas would do.

When the driving strength is reduced below a critical level, we are witness to a peculiar phenomenon: The particles go preferentially into *one* of the compartments. They are seen to perform increasingly high jumps in the compartment that is emptied, whereas in the other the particles remain closer to the bottom of the container. If an energetic particle lands in the latter, it loses most of its energy. With time, the effect becomes more and more pronounced, and a cluster of slow particles is formed, leaving only a few but very lively particles in the first compartment. The explanation for this remarkable phenomenon, which can be traced back to the inelasticity of the collisions, is given in the introduction (Chapter 1), and a theoretical model based on the particle flux from a compartment is presented. Here, roughly the derivation presented by Jens Eggers in 1999 is followed.

For the two-compartment system the transition from the uniform distribution towards the clustered state takes place at the same value of the driving strength as the reverse transition when the driving is increased again. When the number of compartments is extended to three, this changes radically: The system becomes *hysteretic*, which means that the transition from clustered to uniform takes place at considerably stronger driving than the reverse transition. In Chapter 2 the occurrence of the hysteresis is explained in terms of the flux model.

The system can be extended to an arbitrary number of compartments. In Chapter 3 it is shown that, upon adding more compartments, the hysteresis becomes more pronounced. This means that, once the system has clustered, more and more driving power is needed to dissolve the clusters and return to the uniform state. A stability analysis proves that the only stable situations are those with not more than one cluster present. However, it is shown that on its path towards the single clus-

ter the system easily gets stuck in a state with multiple clusters. This is because particles do not have enough kinetic energy to make it over the walls anymore: Although the system still strives towards a single cluster, for all practical purposes the dynamics comes to a standstill.

In applications clusters are highly unwanted, clogging up production lines, preventing optimal contact between catalysts and reacting chemicals, or impeding the crucial mixing of granular ingredients in the pharmaceutical industry. Therefore, in Chapter 4 the focus is on 'declustering': Given a highly clustered system, under what conditions will it disperse? As the shaking strength increases, the system passes through some critical value, beyond which the cluster ceases to be truly stable. Even there however the cluster resists its breakup, and a considerable time span of continuous energy input, the 'lifetime' of the cluster, is necessary to provoke its abrupt collapse. Far away from the critical value, the cluster lifetime varies exponentially with the driving. This exponential relationship explains the experimental observation that even a small increase in the shaking strength can lead to a large decrease in the cluster lifetime.

Close to the critical point, the cluster lifetime diverges to infinity. It does so as a power-law, with an exponent that is characteristic of a second-order phase transition. This behavior is analyzed in Chapter 5, using a thermodynamic potential based on the flux model.

In Chapter 6 we return to the clustering. As time proceeds, the number of clusters decreases gradually, whereas the size of the clusters grows and grows, a process called *coarsening*. The course of events and the timescales are studied in detail, and it is found that the coarsening process in the granular gas is considerably slower than most other coarsening processes.

In Chapter 7 the clustering phenomenon is employed to create a "granular ratchet" with a spontaneous particle current perpendicular to the direction of energy input. To our knowledge, this is the first practical realization of the theoretically predicted concept of a stochastic ratchet as a collective effect in a completely symmetric geometry.

Finally, Chapter 8 deals with a crucial but usually ignored phenomenon: whenever granular matter is fluidized by vertically shaking a container, the temperature in the direction of energy input always exceeds the temperature in the other directions. It is shown that the anisotropy of the temperature is a *necessary* consequence of the anisotropy of the driving.

Samenvatting

In een doorzichtige container, die door een laag tussenschot in tweeën is gedeeld, bevinden zich kleine kogeltjes. Wanneer de container met voldoende energie in vertikale trilling wordt gebracht, dan vliegen de kogeltjes heftig in het rond en vormt zich een granulair gas dat, net als een gewoon gas, gelijkmatig over de twee bakjes is verdeeld.

Als de schudsterkte tot onder een zekere kritische waarde wordt verlaagd, gebeurt er iets opmerkelijks: de kogeltjes hopen zich op in een van de twee bakjes. In het legere bakje krijgen de kogeltjes steeds meer bewegingsenergie terwijl ze in het andere alsmaar dichter bij de bodem blijven. Komt een kogeltje in dit vollere bakje terecht, dan verliest het een groot gedeelte van zijn energie. Het effect wordt mettertijd steeds uitgesprokener en er ontstaat een cluster van langzame kogeltjes, terwijl in het andere bakje slechts een paar zeer beweeglijke kogeltjes overblijven. De verklaring voor dit opvallende fenomeen, dat berust op de inelasticiteit van de botsingen, is te vinden in hoofdstuk 1. Hier wordt ook een theoretisch model gepresenteerd, dat gebaseerd is op de deeltjesflux uit een bakje, waarbij min of meer de afleiding van Jens Eggers (uit 1999) wordt gevolgd.

Voor het twee-bakjes systeem vindt de overgang van de uniforme naar de geclusterde toestand bij dezelfde schudsterkte plaats als de omgekeerde overgang. Dit verandert ingrijpend als het systeem uitgebreid wordt naar drie compartimenten. Het vertoont nu *hysterese*: de overgang van een cluster naar de uniforme verdeling geschiedt nu bij een veel grotere schudsterkte dan de overgang van de uniforme naar de geclusterde situatie. In hoofdstuk 2 wordt het optreden van de hysterese verklaard met behulp van het fluxmodel.

Het systeem kan worden uitgebreid tot een willekeurig groot aantal bakjes. In hoofdstuk 3 wordt aangetoond dat naarmate er meer compartimenten worden toegevoegd, de hysterese steeds uitgesprokener wordt. Als gevolg hiervan is er in een geclusterd systeem steeds meer schudvermogen nodig om de clusters te doen verdwijnen en terug te keren naar de uniforme verdeling. Stabiliteitsanalyse toont aan dat alleen toestanden met ten hoogste één cluster werkelijk stabiel kunnen zijn.

Het systeem kan echter in een toestand met meerdere clusters blijven steken. Dit komt dan doordat de kogeltjes in de deelclusters niet genoeg energie hebben om over de scheidingswanden heen te springen: de dynamica komt tot stilstand, ook al streeft het systeem nog steeds naar een stabiele toestand met slechts één cluster.

In toepassingen zijn clusters zeer ongewenst. Ze blokkeren pijpleidingen, ze maken goed contact tussen katalysatoren en de reagerende chemicaliën onmogelijk en belemmeren de noodzakelijke vermenging van granulaire grondstoffen in de farmaceutische industrie. Daarom is hoofdstuk 4 gewijd aan het 'ontclusteren': onder welke condities zal een sterk geclusterd systeem zich over alle bakjes verspreiden? Bij het opvoeren van de schudsterkte passeert het systeem de kritieke grens waarboven het cluster niet meer stabiel is, maar desalniettemin houdt het cluster nog lang stand. Er is een behoorlijk lange periode van energietoevoer nodig (de 'levensduur' van het cluster) voordat het uiteindelijk uiteenvalt. Ver van de kritieke waarde hangt de levensduur van het cluster exponentiëel van de schudsterkte af. Dit exponentiële verband verklaart de experimentele waarneming dat een minieme toename van de schudsterkte al kan leiden tot een enorme vermindering van de levensduur van het cluster.

Vlak bij het kritieke punt divergeert de levensduur van het cluster en wordt oneindig groot. Dit gebeurt via een zogenaamde 'power-law', en wel met een exponent die karakteristiek is voor een tweede orde fase-overgang. Dit gedrag wordt geanalyseerd in hoofdstuk 5, waar gebruik gemaakt wordt van een thermodynamische potentiaal op basis van het flux model.

In hoofdstuk 6 keren we terug naar het clusteren. Naarmate de tijd verstrijkt, wordt het aantal clusters geleidelijk minder, terwijl de grootte van de clusters juist voortdurend toeneemt. Dit proces staat bekend als 'coarsening'. Een gedetailleerde studie van de tijdschalen in dit proces toont aan dat de coarsening in het granulaire gas beduidend trager verloopt dan in de meeste andere systemen.

In hoofdstuk 7 wordt het clusteren gebruik om een "granulaire ratchet" te creëren, met een spontaan optredende deeltjesstroming, loodrecht op de richting waarin de energie aan het systeem wordt toegevoerd. Voor zover bekend is dit de eerste experimentele verwezenlijking van het theoretisch voorspelde concept van een stochastische ratchet als gevolg van een collectief effect binnen een volledig symmetrische geometrie.

Hoofdstuk 8 tenslotte behandelt een belangrijk maar gewoonlijk veronachtzaamd fenomeen: als granulaire materie door vertikaal schudden gefluidiseerd wordt, blijkt de temperatuur in de vertikale richting altijd groter te zijn dan de temperatuur in de andere richtingen. Aangetoond wordt dat deze anisotropie in de temperatuur een *noodzakelijk* gevolg is van anisotropie in de energietoevoer.

Acknowledgements

First I would like to express my deepest gratitude towards Detlef Lohse, my promotor. He had the courage to move into a new field with new people, and gave me the opportunity and the support to carry out the research leading to this thesis. From him I learned what it means to do physics research within a team.

The second person I want to thank is Ko van der Weele, for all the work we did together, for the many lively discussions we had in Dutch, English, and Greek, and for the countless hours spent in polishing our manuscripts and presentations to near-perfection. He showed me how to invest in presenting intricate and complicated physics in a clear and lively manner.

I want to give thanks to the Directors of Education of our Physics Department, Cor Blom and Clemens Pouw, first for hiring me as a university teacher and second for approving of my move towards research. They have always been extremely supportive and allowed me to combine teaching and research.

I want to thank Peter Reimann for sharing his enormous commitment and the depth of his physical reasoning. I very much cherish our collaboration and especially our mutual visits, in Augsburg, Bielefeld, and Enschede.

Thanks also go to all my scientific colleagues from the Physics of Fluids group: the prosperous and powerful team consisting of professors Leen van Wijngaarden, Andrea Prosperetti, and Nico de Jong, fellow staff-members Gerrit de Bruin, Michel Versluis, and Sascha Hilgenfeldt, post-docs Claus Dieter Ohl, Stefan Luther, Phillipe Marmottant, Adrian Staicu, and Nicolas Bremond. I value our collaboration and retain good memories of the conversations we have had so far.

A special word of gratitude goes to our technicians Gert-Wim Bruggert and Henni Scholten. They were untiring in the implementation and construction of the many ideas that called for experimental realization during the past few years. The same holds for our system manager, Bas Benschop, who instantaneously helped me through several instances of computer hardware failure. Many thanks also go to Joanita Leferink for her help with the intricate procedures involved in a promotion.

My special appreciation goes to the PhD students of the granular team: René Mikkelsen, Raymond Bergmann, and Peter Eshuis, the latter two of whom are my current room companions. They are great and enthusiastic people and I enjoy working with them a lot. The same holds for the (graduated) granular Master students Marcel Kloosterman, Arthur van Bilsen, Marijn Sandtke, and Remco Rauhé plus the many students who, within the context of various projects, have contributed to our granular research.

I also want to thank the PhD students Manish Arora, Ramon van den Berg, Francisco Fontenele Araujo, Jos de Jong, Sander van der Meer, Mark Stijnman, and Christian Veldhuis for being truly fine colleagues. The same is true for the former members of the group: Rüdiger Tögel, Anna von der Heydt, Irene Mazzitelli, Judith Rensen, Kengo Ichiki, Florine Meijer, Marie-Caroline Jullien, especially the ones that put up with me as a room mate.

I want to thank Christiaan Zeilstra, Martin van der Hoef, Matthijs Goldschmidt, and Bob Hoomans, all in the Fundamentals of Chemical Reaction Engineering group headed by professor Hans Kuipers. Their work on granular particle simulations is invaluable for the numerical part of the research in this thesis, and constitutes the foundation for our MD simulation, of which the first version was built by Xander van Doornum and Arthur van Bilsen.

Many thanks go also to my colleagues of the Institute of Physics Education: Brigitte Tel, Imme de Bruijn, Maarten van Woerkom, Ben Oude Alink, Henk van Dijk, Ruud Heijstek, Roel Jansen, Paul Rupert, Lambert Wolterbeek, Cristy Brandriet, and the many teaching assistants with whom I have worked together very pleasantly during the last years.

Finally I am deeply indebted to Stichting FOM, which not only funded the projects of which this thesis is part, but also showed the flexibility which made the realization of this thesis possible in the first place.

Last but not least my warmest feelings go to Nileen, Steven, and Mara, who had to put up with the large amount of family time invested into this thesis. They have always given me invaluable support at times when I needed it.

Devaraj van der Meer
Enschede, March 2004

About the Author

Devaraj van der Meer was born on August 1, 1963, in Amsterdam, the Netherlands. He studied Physics at the University of Leiden and Modern Greek at the University of Amsterdam. In 1990 he obtained a cum laude Master's degree in theoretical physics with dr. P.J.M. Bongaarts and prof. dr. R.H. Terwiel on formal quantum field theory.

From 1990 to 1992 he worked at the international advertizing agency Ogilvy & Mather, and in 1993 started studying at the institute of post-graduate studies of the University of Twente. Here he obtained his high school teaching qualification ("eerstegraads") with dr. ir. I. de Bruijn in 1995, and simultaneously worked as a high school teacher at the Erasmus College (1993-1994) and the Canisius (1994-1997), both located in Almelo.

In 1997 he accepted a teaching position at the University of Twente, where he became also involved in the adaptation and implementation of the physics curriculum within a turbulently evolving educational environment.

In 2000 he returned to physics research when he started to work on granular matter together with dr. J.P. van der Weele and prof. dr. D. Lohse. In 2002 he joined the Physics of Fluids group headed by prof. Lohse as a research scientist, where he also started working on his PhD thesis.